FILE COPY
NO. 2-W

N 62 65712

ARR No. L6E22

NATIONAL ADVISORY COMMITTEE FOR AERONAUTICS

WARTIME REPORT

ORIGINALLY ISSUED
August 1946 as
Advance Restricted Report L6E22

WIND-TUNNEL TESTS AND ANALYSIS OF THREE 10-FOOT-DIAMETER THREE-BLADE TRACTOR PROPELLERS DIFFERING IN PITCH DISTRIBUTION

By Jean Gilman, Jr.

Langley Memorial Aeronautical Laboratory
Langley Field, Va.

FILE COPY
To be returned to
the files of the National
Advisory Committee
for Aeronautics
Washington, D. C.

NACA

WASHINGTON

NACA WARTIME REPORTS are reprints of papers originally issued to provide rapid distribution of advance research results to an authorized group requiring them for the war effort. They were previously held under a security status but are now unclassified. Some of these reports were not technically edited. All have been reproduced without change in order to expedite general distribution.

NACA ARR No. L6E22

NATIONAL ADVISORY COMMITTEE FOR AERONAUTICS

ADVANCE RESTRICTED REPORT

WIND-TUNNEL TESTS AND ANALYSIS OF THREE 10-FOOT-DIAMETER THREE-BLADE TRACTOR PROPELLERS DIFFERING IN PITCH DISTRIBUTION

By Jean Gilman, Jr.

SUMMARY

An investigation was conducted at low Mach numbers to determine the effect of variations in pitch distribution on propeller efficiency. Three 10-foot-diameter three-blade tractor propellers mounted on a streamline body were tested for a blade-angle range from 15° to 65°.

In addition to the usual procedure of determining propeller thrust and power coefficients by force-balance measurements, surveys were made of the total pressure in the propeller wake to determine the thrust loadings. The over-all propeller characteristics as well as the thrust and torque loadings were also determined by an analytical method.

The section thrust and torque coefficients are presented for seven standard radii in a form that enables rapid determination of the thrust and torque loadings of the three propellers at operating conditions within the limits of the data obtained. Charts are presented that show the variation of power coefficient with blade-angle setting and advance-diameter ratio and that include lines of constant efficiency. Other charts show the variation of thrust coefficient with advance-diameter ratio at both constant blade-angle setting and constant power coefficient. A comparison of the variation of thrust coefficient with advance-diameter ratio at several constant values of power coefficient is made to show the relative efficiency of the three propellers for a large range of operating conditions. The efficiencies are compared at several simulated flight conditions ranging from take-off to high speed.

For the simulated flight conditions, the induced axial and rotational components of the efficiency loss, and the component due to profile drag are evaluated and presented in tabular form. Representative distributions of these induced and profile-drag losses are shown.

Good agreement was obtained between the calculated and measured propeller characteristics. The results indicated that high efficiencies at large advance-diameter ratios (in excess of 3.0) could be maintained if the pitch distribution were near optimum. The induced axial-energy loss was shown to be independent of pitch distribution when the propeller was operating near peak efficiency. The induced rotational-energy loss might become excessively high at large advance-diameter ratios. The loss of efficiency due to profile drag would be critically dependent on the advance-diameter ratio and the relationship between C_L and $\tan \gamma$ at a given section.

INTRODUCTION

The ideal pitch distribution of a propeller is the pitch distribution that, for a given operating condition, will yield minimum energy losses. The induced energy loss is a minimum when the blade loading is optimum. The profile-drag energy loss is a minimum when the product of the blade chord and profile-drag coefficient at each section is the least possible for the required blade loading. These requirements for minimum energy losses may be achieved for a given operating condition by following design procedures such as those set forth in references 1 to 3, which are based on the work of Betz and Goldstein.

Because of the fixed pitch distribution of a given propeller, the proper load distribution can not be maintained over a range of operating conditions. The variation from optimum loading may become appreciable for large ranges of operating conditions such as those now being encountered by high-speed airplanes. The work of reference 2 shows that improperly loading the propeller leads to appreciable increases in induced energy losses at high advance-diameter ratios, although the effect is small at advance-diameter ratios less than approximately 2.5. In particular, the induced rotational-energy loss is shown to become excessive if the shank sections at high advance-diameter ratios are overloaded.

The present investigation was made in the Langley propeller-research tunnel to determine the effects of pitch distribution on propeller characteristics for a range of blade-angle settings from 15° to 65°. The program included tests at low Mach numbers of three 10-foot-diameter propellers having NACA 16-series sections and varying only in pitch distribution. In this program the usual force-balance test methods were supplemented with wake surveys to determine the thrust loadings. The thrust and torque loadings and propeller characteristics were also determined by an analytical method with two-dimensional-airfoil data.

In the present paper the calculated and measured propeller characteristics are compared and curves are presented that show the comparative efficiencies of the three propellers for a large range of operating conditions. The calculated section thrust and torque coefficients were employed to evaluate the induced axial-energy and rotational-energy losses and the loss due to profile drag for several operating conditions.

The section thrust and torque coefficients are presented in a form that enables quick determination of the thrust and torque loadings of the three propellers at operating conditions within the limits of the data obtained.

A chart is presented that permits a fairly rapid qualitative determination of the blade loading for any propeller. This chart was found to be quite useful as an aid in the analysis of the results of this investigation.

SYMBOLS AND COEFFICIENTS

a	axial inflow factor (fig. 1)
a'	rotational inflow factor (fig. 1)
B	number of propeller blades
b	blade section chord, feet
C_D	section profile-drag coefficient $\left(\frac{dD}{\frac{\rho}{2}W^2 b}\right)$
C_L	section lift coefficient $\left(\frac{dL}{\frac{\rho}{2}W^2 b}\right)$

C_{L_D} section design lift coefficient

C_P power coefficient $(P/\rho n^3 D^5)$

C_Q torque coefficient $(Q/\rho n^2 D^5)$

C_T thrust coefficient $(T_p/\rho n^2 D^4)$

D propeller diameter, feet

ΔD change in body drag due to propeller slipstream, pounds

dD section profile drag, pounds $\left(\frac{C_D \rho W^2 b\ dr}{2}\right)$ (fig. 1)

dC_Q/dx section torque coefficient $\left(\frac{dQ/dx}{\rho n^2 D^5}\right)$

dC_T/dx section thrust coefficient $\left(\frac{dT/dx}{\rho n^2 D^4}\right)$

dL section lift, pounds $\left(\frac{C_L \rho W^2 b\ dr}{2}\right)$ (fig. 1)

dQ/r section torque force, pounds (fig. 1)

dT section thrust force, pounds (fig. 1)

E_a energy lost to axial momentum in propeller wake, foot-pounds per second

E_D energy lost through profile drag, foot-pounds per second

E_r energy lost to rotational momentum in propeller wake, foot-pounds per second

F Goldstein correction factor for finite number of blades

ΔH total-pressure rise in propeller wake, pounds per square foot

h maximum thickness of blade section, feet

J	advance-diameter ratio (V/nD)
n	propeller rotational speed, revolutions per second
P	power absorbed by propeller, foot-pounds per second $(2\pi nQ)$
Q	torque of propeller, foot-pounds
q	free-stream dynamic pressure, pounds per square foot $(\rho V^2/2)$
R	radius to propeller tip, feet
r	radius to propeller element, feet
T	shaft tension, pounds
T_p	propulsive thrust, pounds $(T - \Delta D)$
V	free-stream velocity, feet per second
V_l	local axial velocity, propeller removed, feet per second
W	true resultant velocity, feet per second (fig. 1)
W_o	geometric resultant velocity, feet per second (fig. 1)
w_1	total interference velocity at airfoil, feet per second (fig. 1)
x	radius ratio (r/R)
x_0	radius ratio at spinner juncture
α	section angle of attack, degrees (fig. 1)
β	blade-section angle, degrees (fig. 1)
$\gamma = \tan^{-1} \frac{C_D}{C_L}$	
ϵ	angle of inflow, degrees (fig. 1) $\left(\tan^{-1} \frac{\sigma C_L}{4F \sin \phi}\right)$

η propulsive efficiency $\left(T_p V/P \quad \text{or} \quad C_T J/C_P\right)$

η'_o blade-section profile-drag efficiency

ρ mass density of air, slug per cubic foot

ρ_0 standard sea-level mass density, slug per cubic foot

σ section solidity $(Bb/2\pi r)$

ϕ aerodynamic helix angle, degrees (fig. 1)

ϕ_o geometric helix angle, degrees $\left(\tan^{-1}\frac{J}{\pi x}\right)$ (fig. 1)

ψ angle of twist in propeller slipstream, degrees

EQUATIONS AND METHODS OF ANALYSIS

For the determination of section thrust coefficient dC_T/dx from the wake pressure measurements, a convenient equation is given in reference 4 that transposes to

$$\frac{dC_T}{dx} = \frac{\Delta H}{q}\frac{\pi}{4}J^2 x \qquad (1)$$

Section thrust and torque coefficients were calculated by the method given in reference 5. The airfoil characteristics shown in figure 2 for NACA 16-series propeller sections were used in the calculations. These airfoil data were interpolated from reference 6. The free-stream velocity distribution was assumed to be uniform and the calculations were based on the propeller design dimensions.

Equations for evaluating the induced fractional energy losses were taken from reference 2. The fractional energy lost to axial momentum is

$$\frac{E_a}{P} = \frac{J}{C_P}\int_{x_0}^{1.0} a\frac{dC_T}{dx}\,dx \qquad (2)$$

and to rotational momentum

$$\frac{E_r}{P} = \frac{1}{C_Q} \int_{x_0}^{1.0} a' \frac{dC_Q}{dx} dx \tag{3}$$

where

$$a = \frac{-1 + \sqrt{1 + \frac{4 \frac{dC_T}{dx}}{\pi J^2 x F}}}{2} \tag{4}$$

$$a' = \frac{dC_Q}{dx} \frac{2}{\pi^2 J x^3 (1 + a) F} \tag{5}$$

The value of x_0 for this investigation is 0.236 for all three propellers.

The fractional energy loss due to profile drag is

$$\frac{E_D}{P} = \frac{1}{C_Q} \int_{x_0}^{1.0} \left(1 - \eta'_o\right) \frac{dC_Q}{dx} dx \tag{6}$$

The value of η'_o can be shown to be

$$\eta'_o = \frac{\tan \phi}{\tan (\phi + \gamma)}$$

where

$$\tan \phi = \frac{1 + a}{1 - a'} \tan \phi_o$$

The angle γ can be determined from figure 2(b) if the operating C_L is known. An expression giving the operating C_L can be derived from the following:

$$\frac{dC_T}{dx} = \frac{BbJ^2}{8R} \frac{(1 + a)^2}{\sin^2 \phi} \left(C_L \cos \phi - C_D \sin \phi\right)$$

$$\frac{dC_Q}{dx} = \frac{BbJ^2x}{16R} \frac{(1 + a)^2}{\sin^2\phi} \left(C_L \sin \phi + C_D \cos \phi\right)$$

Eliminating C_D from the expressions for the section thrust and torque and solving for C_L gives the following equation

$$C_L = \frac{4D}{xBbJ^2} \left(x \frac{dC_T}{dx} + 2 \tan \phi \frac{dC_Q}{dx}\right) \frac{\cos \phi \sin^2\phi}{(1 + a)^2}$$

APPARATUS

Test Equipment

The tests were conducted in the Langley propeller-research tunnel. A photograph of the test setup is given as figure 3 and the dimensional details are shown in figure 4. A close-up of the propeller-spinner arrangement is given as figure 5. The gap between the propeller blade and the celluloid coverplate was one thirty-second of an inch all around.

The propellers were driven by two variable-speed 25-horsepower electric induction motors that incorporated spring-selsyn dynamometer equipment for measuring torque. Propeller rotational speed was determined by means of electric tachometers and propeller thrust, by the tunnel thrust-balance equipment.

The total-pressure rise in the propeller wake was determined by a horizontal rake of total-pressure tubes along the right-hand radius. The radial stations at which the individual total-pressure tubes were located were at 30, 34, 37, 42, 45, 51, 55, 60.5, 65, 75, 80, 85, 90, 95, 99, 103, and 110 percent of the propeller radius. The distance from the propeller center line back to the total-pressure tubes was $7\frac{1}{2}$ inches (0.0625D), and the minimum clearance between the blade trailing edge and the total-pressure tube at 0.30R was 0.0135D, or 1.62 inches. Pressures were recorded photographically from an NACA recording multiple tube manometer, which was inclined 60° from the vertical in order to double the magnitude of the readings.

PROPELLERS

The three propellers selected for the investigation were the NACA 10-308-03-55, 10-308-03-45, and 10-308-03-30 and will hereinafter be referred to as propellers 55S, 45S, and 30S, respectively. The first group of numerals in the designation denotes the propeller diameter in feet; the first digit of the second group is ten times the design lift coefficient at 0.70R; and the last two digits of the second group express the thickness-chord ratio at 0.70R. The third group of figures gives the solidity per blade at 0.70R and the last group designates the approximate blade-angle setting at 0.70R for the design condition. The blade design incorporates NACA 16-series sections. The activity factor for each blade is 90 or for the three-blade tractor propellers, 270. The blade-form characteristics are shown in figure 6, which also includes a curve showing the design lift coefficient C_{L_D} of the airfoil section at each station. The angular twist $(\beta - \beta_{0.75R})$ of the blades is compared in figure 7(a) and curves of p/D are shown in figure 7(b).

The blades of propeller 45S were constructed of dural and conformed very closely to the design dimensions. The blades of propellers 55S and 30S were constructed of mahogany and varied somewhat from the design dimensions. The blade-section angles of propeller 55S were generally within $\pm 0.25^\circ$ of the specified angles, but two of the blades of propeller 30S were found to be as much as 2° too high in the tip region and to vary by $\pm 1^\circ$ in the shank sections.

TESTS

The range of the force measurements was from zero thrust to well beyond the stall for the blade angles of the following table:

Propeller	Blade angle at 0.75R (deg)									
55S	15	25	30	35	40	45	50	55	60	--
45S	15	25	30	35	40	45	50	55	--	65
30S	15	25	30	35	--	45	--	55	--	65

The engine speed varied from a maximum of 550 rpm for low blade angles to 175 rpm for peak efficiency at $\beta_{0.75R} = 65^\circ$. The tunnel airspeed varied from 90 miles per hour for the large blade angles to 37.5 miles per hour for peak efficiency at $\beta_{0.75R} = 15^\circ$. The Reynolds number based on the chord at 0.75R was of the order of 1×10^6. The resultant velocities were too low to lead to any compressibility effects for the tip Mach number was always less than 0.3.

At each blade angle, measurements of the total pressure were made for a range of advance-diameter ratio to include only the region of peak efficiency. No attempt was made to obtain measurements under conditions of stalled operation because previous investigations (for example, reference 4) have shown that such measurements are unreliable. The pressure measurements were not extended to include zero thrust because of the limited time available for testing. A velocity survey (propeller removed) was made $7\frac{1}{2}$ inches behind the propeller disk and the results are shown in figure 8.

Blade-deflection tests of the thin wooden blades, in which a reflected-light-beam method similar to that of reference 7 was used, showed that the blade deflections were not unduly large. At a blade angle of 30° the deflection varied from about 0.1° at an advance-diameter of 0.3 to no measurable amount at peak efficiency. At a blade angle of 55°, the deflection varied from 0.6° at a low value of J to 0.1° at peak efficiency.

RESULTS AND DISCUSSION

In presenting the results of this investigation of pitch distribution, the blade section characteristics

and propeller characteristics are discussed separately. The efficiencies of the three propellers are compared for a range of operating conditions to show the effect of changes in the load distribution. A discussion of energy losses completes the presentation.

Blade Section Characteristics

Calculated blade-section characteristics.- The calculated blade section characteristics for seven standard radii are shown in figures 9 to 14. The variation of dC_T/dx with J at both constant blade-angle setting and constant power coefficient for propellers 55S, 45S, and 30S, are shown in figures 9 to 11. The corresponding values of dC_Q/dx are shown in figures 12 to 14.

Measured blade-section characteristics.- Curves of dC_T/dx against J, as determined from the wake pressure measurements, are presented in figures 9 to 11 for several blade-angle settings. Close agreement between the measured and calculated results was not realized. Some of the factors that may have affected the results are: the flow angularity and velocity variation in the tunnel jet, the increase in stream velocity at the spinner (fig. 8), the use of interpolated airfoil-section data, and the previously noted variation of the wooden blades from design dimensions. Some error was also probably derived from the use of a single survey rake for a recent investigation (reference 8) concludes that more accurate data result from wake surveys across the propeller diameter rather than along a single radius.

The measured $\frac{dC_T}{dx}$-curves, however, are generally parallel to the calculated curves. Inasmuch as the assumption of the independence of blade sections holds to a fair degree of accuracy, the measured and calculated curves of dC_T/dx could possibly be brought into substantial agreement by considering only the blade discrepancies and the actual $\frac{V_l}{V}$-distribution. This procedure was not attempted, however, because of the uncertainty introduced by the use of a single survey rake.

Because of the unsatisfactory nature of the measured section thrust coefficients, the discussion is confined mainly to the calculated section characteristics.

Application of results.- The data presented in figures 9 to 14 may be used to determine the thrust and torque loadings of the propellers tested at a given advance-diameter ratio for either the blade angles or power coefficients shown in the figures. An estimate of the loadings may also be obtained for other propellers of not-too-dissimilar design. Knowledge of the thrust and torque loading is useful for applications such as the determination of the pressure rise obtainable from a propeller and the stream angle in the propeller wake. The pressure rise at any radial station may be estimated by transposing the terms of equation (1) to find $\Delta E/q$. The equation for determining the stream angle immediately behind the propeller disk is given in reference 4 as

$$\tan \psi = \frac{4 \frac{dC_Q}{dx}}{\pi J^2 x^2 (1 + a)^2}$$

The variation of dC_T/dx with J at constant C_P at the 0.30R station is of interest in regard to the pressure rise obtainable for duct entrances located behind this station. Inasmuch as the value of dC_T/dx for propeller 55S is small or negative at low values of J (less than 2.0, see fig. 9(a)), this propeller would either not materially aid air induction or would interfere with it to some extent. The range of J from 1.0 to 2.0 corresponds roughly to climbing conditions for some airplanes, and thus propeller 55S might be deficient in propeller "ram." For the same range of operation, propellers 45S and 30S (figs. 10(a) and 11(a), respectively) would produce a pressure rise. The amount of pressure rise available from a given propeller varies with the type of installation: some installations tend to retard rather than to accelerate the free-stream velocity (propeller removed) and in such installations the section angles of attack of the shanks would be higher for the same advance-diameter ratio. Changing the free-stream velocity distribution for a given propeller has much the same effect on the pressure rise available as changing the pitch distribution for a given installation.

Propeller Characteristics

The over-all characteristics of propellers 55S, 45S, and 30S, as determined from force tests, are shown in figures 15 to 17, respectively. These figures show the variation of C_P with J at constant blade-angle settings and include contour lines of constant efficiency. The operating chart for propeller 55S (fig. 15) is of special interest because it shows that high efficiency can be obtained if the pitch distribution is near the optimum at large advance-diameter ratios. The region of peak efficiency occurs at lower advance-diameter ratios for propellers 45S and 30S (figs. 16 and 17) than for propeller 55S. The advance-diameter ratio for peak efficiency varies with the design pitch distribution and, of further interest, the region of high efficiencies becomes more limited as the design pitch distribution is reduced. The contour curve of propeller 55S for 91-percent efficiency, for example, extends over a range of J from 1.8 to about 4.0 whereas the corresponding range for propeller 45S is from approximately 1.8 to 3.0 and that for propeller 30S, from approximately 1.1 to 2.1.

The variation of the thrust coefficients with advance-diameter ratio at constant blade-angle settings and also at constant power coefficients is shown in figures 18 to 20 for propellers 55S, 45S, and 30S, respectively. The variation of C_T with J at constant C_P, shown for all three propellers in figure 21, provides a comparison of their relative merits for a large range of operating conditions.

Comparison of experimental and calculated propeller characteristics.- The calculated thrust and power coefficients are shown as short-dash lines in figures 15 to 20 for comparison with the measured values. The curves at equal blade-angle settings show a varying lack of agreement, principally as a result of the previously noted blade-discrepancies and the nonuniform velocity field. The calculated results for the metal propeller (45S) are seen to be in better agreement with the measured results than are the calculated results for the wooden propellers, which indicates that the blade-design discrepancies are the more important cause of disagreement in the results of the two methods. When the calculated thrust coefficients are compared with the experimental values at the same power coefficient

(figs. 18 to 20), good agreement is obtained between the two sets of data through most of the operating range.

The good agreement between the experimental and calculated values of thrust coefficient at a given power coefficient indicates that reasonably accurate blade thrust-loading and torque-loading curves may be constructed from the calculated section thrust and torque coefficients shown in figures 9 to 14. A comparison of measured and calculated thrust-loading curves at constant power coefficient is given in figure 22. Because of the uncertainty of the wake-survey data, this comparison is approximate, but the comparison is believed to tend to bear out the assumption that the calculated loadings will be similar to the actual loading for a given operating condition.

The increase of flow velocity due to the spinner (propeller removed) raises the question of the effect of this nonuniform velocity distribution on the propeller characteristics. In order to determine this effect, the characteristics were recalculated for propeller 45S at $\beta_{0.75R} = 25^\circ$ and 55° and a comparison of these values with the previously calculated values based on a uniform velocity field is shown in the following table:

Propeller 45S								
$\frac{V_l}{V}$	Blade angle at 0.75R							
	25°				55°			
	J	C_T	C_P	η_{max}	J	C_T	C_P	η_{max}
1.0	1.0	0.0432	0.0480	0.900	3.3	0.0625	0.2240	0.920
From fig. 8	1.0	.0390	.0445	.875	3.1	.0858	.2910	.914

Comparison of propeller efficiencies at various simulated flight conditions.- Several values of J and C_P were chosen as a basis for comparison of the propeller characteristics and for analysis of the efficiency losses. For constant-speed propellers,

C_p increases with increasing altitude and J increases with increasing forward speed. Values of C_p and J were therefore selected to simulate low speed at sea level, medium and high speeds at a medium altitude, and high speeds at two high altitudes. These values of C_p and J and other pertiment data are presented in the following table:

Flight condition	Take-off at sea level	Climb at 33,800 ft	High speed at 33,800 ft	High speed at 44,200 ft	High speed at 39,400 ft
ρ/ρ_0	1.000	0.325	0.325	0.200	0.250
J	.80	2.00	3.15	3.00	3.80
C_p	.080	.246	.246	.400	.320

It is emphasized that compressibility effects are not considered in this investigation. In practice the simulated operating conditions considered, except possibly take-off, would probably lead to compressibility losses that would exceed the other losses discussed herein.

The values from the preceding table of $J = 3.15$ and $C_p = 0.246$ correspond to the highest efficiency of propeller 55S on the efficiency contour curve. (See fig. 15.) If these values are assumed to represent high speed at altitude, maximum rate of climb at the same altitude would require the same value of C_p but would require an advance-diameter ratio of the order of 1.2 to 2.0, depending on the airplane characteristics. In this comparison, climb is represented by $J = 2.00$ and $C_p = 0.246$. Take-off is usually accomplished at an advance-diameter ratio of 0.5 or less, but in this case a value of $J = 0.80$ and a value of C_p of 0.080 are assumed. Because of the current lack of data on NACA 16-series airfoils at the larger lift coefficients, it is not possible to calculate the values of C_p just mentioned for advance-diameter ratios lower than those used herein for climb and take-off.

The variation of η at the selected values of C_p is shown in figure 23 for a range of J to include the values of J chosen for comparison. Propeller 55S is seen to have a higher efficiency than propellers 45S and 30S in the range of advance-diameter ratio from 2.60 to 3.30. In most of the range of J simulating climb at altitude (1.2 to 2.0) propeller 45S is most efficient; whereas propeller 30S is most efficient in take-off. The difference in efficiency in climb and take-off, however, is small. The values of η at the simulated flight conditions are summarized in table I.

Effect on Load Distribution of Changes in Operating Conditions

The thrust-loading and torque-loading curves shown in figures 24 to 28 are presented for the simulated flight conditions of the preceding section. These figures indicate that the differences in the loadings due to the pitch-distribution differences of the three propellers are greater at high than at low advance-diameter ratios for equal power absorption.

For a given propeller the resultant force at any blade section, which determines the thrust and torque at the section, depends on the square of the resultant velocity W_o and the geometric angle of attack $\beta - \phi_o$. At constant advance-diameter ratio, the resultant velocities increase with increasing radius. With increasing advance-diameter ratio, the resultant velocities of the inboard sections become a larger percentage of the resultant velocities at the tip sections. If $\beta - \phi_o$ remains constant along the blade, for example, increasing the value of J increases the resultant force of the shank sections as compared to that of the tip sections. The geometric angle of attack, however, is not necessarily constant along the blade but depends on β and ϕ_o at each section. The radial variation of ϕ_o at any J can be determined from the relation

$$\tan \phi_o = \frac{J}{\pi x} \frac{V_l}{V}$$

The radial variation of ϕ_o was calculated for a large range of advance-diameter ratio, with V_l/V taken to be equal to 1.0 all along the blade. The variation of ϕ_o, expressed as $\phi_o - \phi_{o_{0.75R}}$, with J at eight standard radii is shown in figure 29. These curves give the angular twist of the resultant geometric air stream for any value of J.

The angular twist of the propeller blades has previously been expressed as $\beta - \beta_{0.75R}$. (See fig. 7(a).) If for some value of J under consideration the quantity $\phi_o - \phi_{o_{0.75R}}$ is subtracted from the quantity $\beta - \beta_{0.75R}$, the difference gives a measure of the variation of the geometric angles of attack along the blade. The curves of

$$\left(\beta - \beta_{0.75R}\right) - \left(\phi_o - \phi_{o_{0.75R}}\right)$$

for propeller 30S at J = 3.80 and for propeller 45S at J = 0.80 are shown in figures 30(a) and 30(b). The curve for propeller 30S shows that for any given geometric angle of attack at 0.75R the shank and tip angles of attack will be greater, and these larger shank and tip angles readily account for the shape of the thrust- and torque-loading curves of propeller 30S at J = 3.80. (See fig. 28.) The curve of

$$\left(\beta - \beta_{0.75R}\right) - \left(\phi_o - \phi_{o_{0.75R}}\right)$$

for propeller 45S at J = 0.80 (fig. 30(a)) shows that the shank angles of attack are much larger than are the tip angles of attack. Most of the thrust and torque load of propeller 45S is shown in figure 24 to be located at the outboard stations in spite of the large shank angles, the reason being that at J = 0.80 the resultant velocities over the shank sections are very low as compared with the resultant velocities over the tip sections. The variation of the square of the ratio of the shank resultant velocity to the tip resultant velocity with advance-diameter ratio is illustrated by the following table:

J	0.5	1.0	1.5	2.0	2.5	3.0	4.0	5.0
$\left(\frac{W_{o_{0.30R}}}{W_{o_{0.95R}}}\right)^2$	0.125	0.191	0.280	0.376	0.469	0.546	0.675	0.765

The resultant force at a section (when profile drag is neglected) is $\frac{bC_L\rho W^2\,dr}{2}$. Inasmuch as the magnitude of the vector W is very nearly the same as that of vector W_o, the table just given indicates directly the increasing importance of a shank section as compared with a tip section as J is increased.

If values of $\beta - \beta_{0.75R}$ for any propeller are plotted directly in figure 29 to the same scale as the values of $\phi_o - \phi_{o_{0.75R}}$, values of

$$\left(\beta - \beta_{0.75R}\right) - \left(\phi_o - \phi_{o_{0.75R}}\right)$$

may be readily seen. The plot therefore gives a qualitative representation of the angle-of-attack variation, which, with due consideration to the radial location of the sections, the section chords, and the value of J, gives a rough idea of the loading to be expected. For propellers incorporating sections with large values of angle of zero lift, it may be desirable to base the angle β on the zero-lift line rather than on the chord line of the section.

The blade twist $\beta - \beta_{0.75R}$ of a structurally practical propeller should be approximately the same as the twist of the resultant air stream to realize the best efficiency at a given J. For example, the angular blade twist of propellers 5S, 4S, and 3S is indicated in figure 29 at $J = 3.15$, 2.60, and 1.40, respectively; for each propeller the value of J corresponds approximately to peak efficiency. In each case the blade twist approximates the air-stream twist at the value of J for peak efficiency. Deviations from the optimum blade twist lead to more important losses at high than at low values of J, as illustrated by the η-values in table I. At $J = 0.80$, for example,

the difference in η for propellers 45S and 30S is 0.035; at $J = 3.80$, the difference in η for propellers 30S and 55S is 0.083.

The most interesting fact brought out in figure 29 is that in order to conform to the resultant twist, the design blade twist should be increased as the design J is increased to a value of about 2.0 and should then be decreased as J is further increased. If the propeller design J is about 2.0, the blade twist fails to conform to the twist of the resultant air stream at values of J either higher or lower than 2.0. If the value of the design J is 3.0 or greater, on the other hand, the blade twist is similar to that of a propeller designed to operate at $J = 1.0$.

Breakdown of Energy Losses

The induced energy losses, E_a/P and E_r/P, and the loss due to profile drag E_D/P were evaluated for the five simulated flight conditions, and the results are shown in table I. The sum of these losses $\frac{E_a + E_r + E_D}{P}$ is presented for comparison with the measured total fractional energy loss $1 - \eta$, in which the value of η is the observed value. Inasmuch as, for incompressible flow, the value $\frac{E_a + E_r + E_D}{P}$ represents the total fractional energy loss, the values of $\frac{E_a + E_r + E_D}{P}$ and $1 - \eta$ in table I should be very nearly equal. The calculated fractional energy losses closely check the measured losses in several instances, but inequalities occur because of the discrepancies between the actual and calculated loadings, as indicated in figure 22, and also because the agreement between calculated and measured thrust coefficients at equal power coefficients is not exact in all cases. The lack of agreement at equal power coefficients is illustrated by a comparison in table I of the integrated C_p-values from figures 24 to 28 with the C_p-values chosen for the simulated flight conditions and by a comparison of the observed and calculated thrust coefficients. The integrated value of C_p for propeller 30S, for example,

is 3 percent less than the C_P-value chosen for simulated flight at $J = 3.15$, and the integrated C_T-value is 4 percent higher than the observed C_T at $J = 2.00$.

Axial-energy loss.- The $\frac{E_a}{P}$-values for the three propellers in table I are of the same magnitude at any one operating condition. The axial-energy loss is a large percentage of the total energy loss at $J = 0.80$, but this percentage decreases as J increases.

Representative distributions of the axial-momentum-loss factor $a\frac{dC_T}{dx}$ are shown in figures 31(a) and 32(a) for climb and for one of the high-speed conditions. The distributions for the other high-speed conditions are similar to figure 32(a) and for take-off, compare with those for climb (fig. 31(a)).

The calculated axial-energy losses for each simulated flight condition, are compared in table II with the optimum axial-energy losses as determined from reference 2 for the same flight condition. The optimum and calculated losses practically coincide for each flight condition, which shows that little, if any, improvement in the axial-energy loss could be achieved by further varying the load distribution of these three propellers.

Rotational-energy loss.- The distributions of the rotational-energy-loss factor $a'\frac{dC_Q}{dx}$ are shown in figures 31(b) and 32(b) for climb and high speed. The distribution for take-off is similar to climb and all high-speed distributions are comparable to that of figure 32(b). The integrated results in table II show that the roational-energy loss generally tends to increase with increasing J. Because of the heavier shank loadings of propellers 45S and 30S, the rotational losses of these propellers are greater than those of propeller 55S.

A comparison of the calculated and optimum values of E_r/P in table II indicates that the rotational-energy loss of propeller 55S is about optimum throughout the operating range under consideration but that gains in efficiency could be realized in the case of propellers 45S and 30S at large values of J.

Profile-drag energy loss.- Except for the high-speed operating condition represented by $J = 3.80$ the calculated values of E_D/P in table I indicate that the loss of efficiency due to profile drag varies but slightly. The low profile-drag losses are mainly the result of the small profile drag of the thin shank sections of these propellers.

The distributions of the profile-drag energy loss $\left(1 - \gamma'_0\right)\frac{dC_Q}{dx}$ are shown in figures 33 to 37 for each of the operating conditions presented in table I.

Application to design.- The foregoing comparisons of the axial-, rotational-, and profile-drag energy losses indicate that, of these three factors, for light loadings (near peak efficiency), the induced axial-energy loss is not susceptible to design treatment insofar as pitch distribution is concerned. Changes in the pitch distribution, however, affect both the induced rotational and the profile-drag energy but affect each in a different manner.

When the angle ϕ is small, the value of the induced-inflow factor a' is seen in figure 1 to be inconsequential compared with that of the inflow factor a but these values reverse when ϕ is large. The angle ϕ becomes larger, of course, as J increases. The condition for minimum induced-energy loss requires that

$$x \tan \phi = \text{constant}$$

as discussed in reference 3. For a given operating condition, this uniform helical wake is attained by a certain distribution of the blade loading bC_L. Charts in references 1 and 3 that give the necessary distribution of bC_L to attain minimum induced energy losses at a given operating condition show that bC_L must be decreased in the shank region as J is increased. The factor $a'\frac{dC_Q}{dx}$ is thus kept as small as practicable in the region where large values of ϕ are unavoidable.

Figure 29, however, shows that a propeller designed to operate at an advance-diameter ratio of roughly 1.0 to 2.0 (for example, propellers 30S and 45S) may be overloaded along the inner radii if it is operated at values of J in excess of about 2.5. At J = 3.15 the inboard values of $a'\frac{dC_a}{dx}$ for propellers 45S and 30S are shown in figure 32(b) to be much larger than those for propeller 55S. Because of a similar overloading of the shank sections at J = 3.80, the results in table I give values of E_r/P for propellers 45S and 30S that are nearly double the loss in rotational energy for propeller 55S.

Propeller weight and diameter limitations generally require heavier loadings than those encountered with the propellers tested. Charts in reference 2 show that for a given number of blades the optimum value of E_r/P becomes larger if the loading is increased at a constant J. Hence, for more heavily loaded propellers, nonoptimum load distributions of the type experienced by propellers 30S and 45S lead to rotational-energy losses more serious than the results of table I indicate.

The profile-drag energy loss varies with C_D/C_L as indicated by the equation

$$\eta'_o = \frac{\tan \phi}{\tan (\phi + \gamma)}$$

For a small constant value of C_D/C_L, the value of η'_o does not change appreciably in the approximate range of ϕ from 20° to 70°. The value of η'_o decreases rapidly as the value of ϕ decreases below about 20° or increases above about 70°.

The value of C_D/C_L, or $\tan \gamma$, varies with C_L as shown in figure 2(b). Very low operating C_L-values and C_L-values beyond the stall produce an abrupt increase in $\tan \gamma$ with a corresponding increase in the profile-drag loss.

The profile-drag losses for the five simulated flight conditions discussed herein are of particular interest.

In take-off, for example, the measured efficiency of propeller 45S is 81.5 percent as compared with 85.0 percent for propeller 30S and 84.1 percent for propeller 55S. Operating C_L-values were determined for take-off and are presented in figure 38. The C_L-values of propeller 45S, nearly 0.7, in the region of 0.50R, are on the border of the region for an abrupt rise of tan γ. (See fig. 2(b)). Because the airfoil section characteristics are interpolated, however, the values of C_L and tan γ shown must be regarded as estimates rather than the actual values at the blade. Hence, although the calculated value of E_D/P for propeller 45S for take-off only slightly exceeds the value for either of the other two propellers, in actuality the profile-drag loss could be larger than shown - or large enough to account for the discrepancy between the value 0.161 for $\frac{E_a + E_r + E_D}{P}$, and 0.185 for $1 - \eta$, in table I. If this supposition is tenable, the take-off qualities of propeller 45S could be improved either by reducing the pitch in the region of 0.5R or by incorporating shank sections with a higher critical lift coefficient.

The good efficiency of propeller 55S in take-off, 84.1 percent as compared with 85 percent for propeller 30S, illustrates a previously mentioned point - the similarity of the pitch distribution of a propeller of high pitch ($J = 3.0$ or greater) to that of a propeller of low pitch. (See fig. 29.)

The distribution of fractional energy loss due to profile drag of propeller 30S in climb (fig. 34) shows that this loss is large in the tip region. By comparing in figure 29 the blade twist at the tip (beyond 0.75R) with the resultant air-stream twist, propeller 30S is readily seen to be insufficiently twisted in this region for $J = 2.00$. As a result, values of C_L are high in the tip region. The estimated C_L-values of all three propellers are shown in figure 39.

The distributions of fractional energy-loss due to profile drag (figs. 35 to 37) are similar for all three of the simulated high-speed flight conditions. The estimated C_L-values of the three propellers at

$J = 3.15$ and $C_P = 0.246$ are shown in figure 40. It will be noted that the C_L-values at the inner radii of propeller 55S are very low and hence lead to large values of $\tan \gamma$. The resulting low profile-drag efficiency at the inner radii does not seriously affect the propeller efficiency, however, because of the small contribution of these sections to the total power absorption.

A comparison of the rotational- and profile-drag energy losses at $J = 3.80$ shows that of the two losses the profile-drag loss is the more important for each propeller. The C_L-variations for this flight condition, presented in figure 41, indicate that the C_L-values of all three propellers are in a favorable C_D/C_L range for most of the propeller radius. The relationship between C_L and $\tan \gamma$ of the shank sections (from $x = 0.3$ to $x = 0.5$) is more favorable for propellers 45S and 30S than for propeller 55S. The drag losses are shown in figure 37 to be higher for the shank sections in the case of propeller 45S and 30S than for propeller 55S.

At $x = 0.3$ and $J = 3.80$ the angle of the resultant wind ϕ is very large. The angle ϕ_o is a close approximation to the angle ϕ near peak efficiency, and ϕ_o at $J = 3.80$ is shown in figure 29 to be about 76°. Hence, ϕ-values in the region of 0.30R are in the range in which only slight differences in ϕ cause large differences in η'_o, even if $\tan \gamma$ is the same for all three propellers. This sensitivity of the profile-drag loss to large geometric helix angles, coupled with the large power absorption of the inner radii, has a very detrimental effect on the efficiency of propellers 45S and 30S. Propeller 30S suffers an additional profile-drag loss because of the low C_L-value at 0.70R; the "bump" in the curve of the profile-drag-loss distribution of propeller 30S (fig. 37) is the result of the increased value of $\tan \gamma$.

CONCLUSIONS

Tests were made at low Mach numbers to determine the effects of pitch distribution on propeller characteristics for a large range of operating conditions.

The three-blade tractor propellers used were of 10-foot diameter and embodied NACA 16-series airfoil sections. The following conclusions are based on the results of these tests supplemented with data obtained by an analytical method:

1. Good agreement was obtained between the measured and calculated propeller characteristics.

2. High efficiency can be obtained if the pitch distribution is near the optimum at large advance-diameter ratios.

3. A propeller of design advance-diameter ratio of 3.0 or greater would have a favorable loading for lower values of the advance-diameter ratio in the take-off range ($J = 1.0$ or lower).

4. Variations in load distribution have very little effect on the magnitude of the induced axial-energy loss near peak efficiency.

5. The use of a propeller at other than design advance-diameter ratio might incur excessive rotational-energy losses if the operating advance-diameter ratio is in excess of about 2.5.

Langley Memorial Aeronautical Laboratory
National Advisory Committee for Aeronautics
Langley Field, Va.

REFERENCES

1. Crigler, John L., and Talkin, Herbert W.: Propeller Selection from Aerodynamic Considerations. NACA ACR, July 1942.

2. Crigler, John L., and Talkin, Herbert W.: Charts for Determining Propeller Efficiency. NACA ACR No. L4I29, 1944.

3. Hartman, Edwin P., and Feldman, Lewis: Aerodynamic Problems in the Design of Efficient Propellers. NACA ACR, Aug. 1942.

4. Stickle, George W., and Crigler, John L.: Propeller Analysis from Experimental Data. NACA Rep. No. 712, 1941.

5. Crigler, John L.: Comparison of Calculated and Experimental Propeller Characteristics for Four-, Six-, and Eight-Blade Single-Rotating Propellers. NACA ACR No. 4B04, 1944.

6. Stack, John: Tests of Airfoils Designed to Delay the Compressibility Burble. NACA TN No. 976, Dec. 1944. (Reprint of ACR, June 1939.)

7. Hartman, Edwin P., and Biermann, David: The Torsional and Bending Deflection of Full-Scale Aluminum-Alloy Propeller Blades under Normal Operating Conditions. NACA Rep. No. 644, 1938.

8. Pendley, Robert E.: Effect of Propeller-Axis Angle of Attack on Thrust Distribution over the Propeller Disk in Relation to Wake-Survey Measurement of Thrust. NACA ARR No. L5J02b, 1945.

TABLE I

CALCULATED AND EXPERIMENTAL THRUST AND POWER COEFFICIENTS AND BREAKDOWN OF PROPELLER EFFICIENCY LOSSES FOR SEVERAL SIMULATED FLIGHT CONDITIONS

Propeller	Observed η	E_a/P	E_r/P	E_D/P	$\frac{E_a + E_r + E_D}{P}$	$1 - \eta$	Calculated C_P	Observed C_T	Calculated C_T
Take-off; J, 0.80; C_P, 0.080									
55S	0.841	0.090	0.019	0.048	0.157	0.159	0.080	0.0841	0.082
45S	.815	.089	.023	.049	.161	.185	.080	.0815	.084
30S	.850	.087	.019	.047	.153	.150	.079	.0850	.083
Climb; J, 2.00; C_P, 0.246									
55S	0.892	0.037	0.036	0.042	0.115	0.108	0.248	0.1097	0.1073
45S	.883	.033	.036	.037	.106	.117	.244	.1086	.1087
30S	.863	.034	.037	.044	.115	.137	.246	.1062	.1105
High Speed; J, 3.15; C_P, 0.246									
55S	0.930	0.012	0.026	0.051	0.089	0.070	0.244	0.0726	0.071
45S	.905	.009	.034	.049	.092	.095	.248	.0706	.071
30S	.873	.009	.034	.050	.093	.127	.238	.0682	.067
High Speed; J, 3.00; C_P, 0.400									
55S	0.902	0.019	0.043	0.039	0.101	0.098	0.394	0.1202	0.1195
45S	.875	.016	.051	.042	.109	.125	.396	.1168	.1181
30S	.860	.018	.051	.044	.113	.140	.394	.1147	.1185
High Speed; J, 3.80; C_P, 0.320									
55S	0.914	0.007	0.029	0.047	0.083	0.086	0.315	0.0770	0.0751
45S	.873	.006	.050	.064	.120	.127	.313	.0736	.0727
30S	.831	.006	.053	.070	.129	.169	.311	.0700	.0716

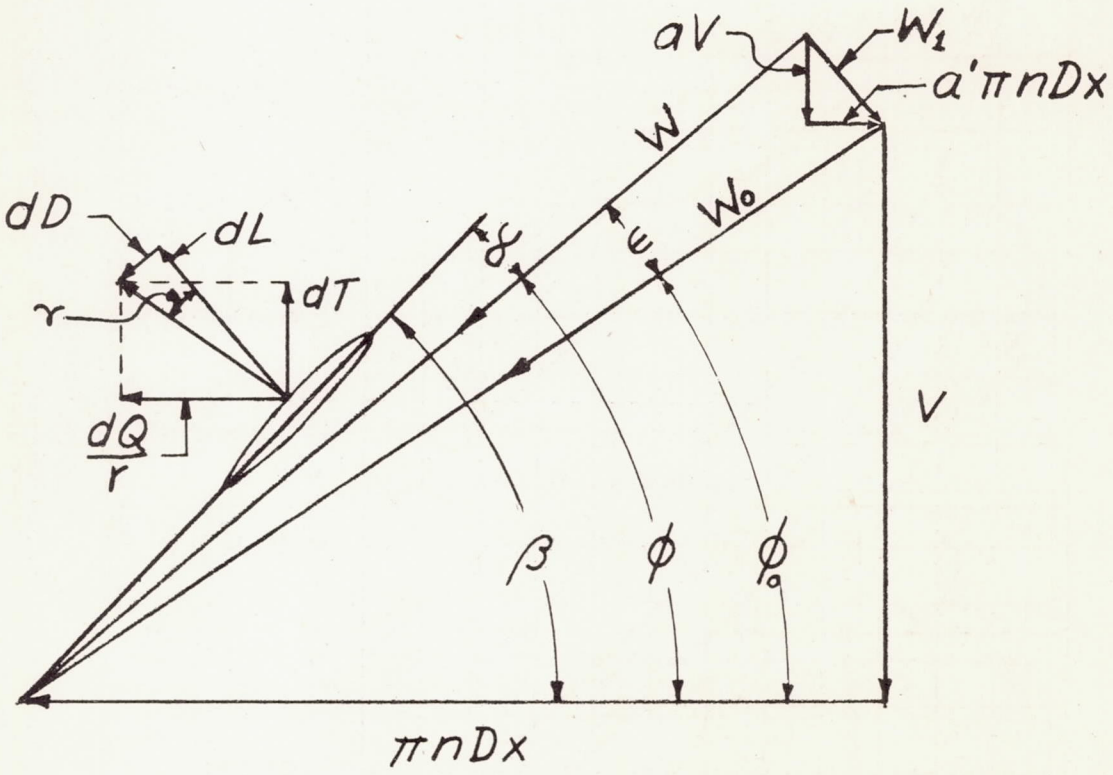
NATIONAL ADVISORY
COMMITTEE FOR AERONAUTICS

INDUCED EFFICIENCY LOSSES OF PROPELLERS 55S, 45S, AND 30S AND OPTIMUM ENERGY LOSSES FOR SEVERAL SIMULATED FLIGHT CONDITIONS

Propeller	Calculated E_a/P	Optimum E_a/P (a)	Calculated E_r/P	Optimum E_r/P (a)
$C_P = 0.080$; $J = 0.80$				
55S	0.090	0.090	0.019	0.024
45S	.089	.090	.023	.024
30S	.087	.090	.019	.024
$C_P = 0.246$; $J = 2.00$				
55S	0.037	0.033	0.036	0.037
45S	.033	.033	.036	.037
30S	.034	.033	.037	.037
$C_P = 0.246$; $J = 3.15$				
55S	0.012	0.014	0.026	0.025
45S	.009	.014	.034	.025
30S	.009	.014	.034	.025
$C_P = 0.400$; $J = 3.00$				
55S	0.019	0.018	0.043	0.045
45S	.016	.018	.051	.045
30S	.018	.018	.051	.045
$C_P = 0.320$; $J = 3.80$				
55S	0.007	0.010	0.029	0.029
45S	.006	.010	.050	.029
30S	.006	.010	.053	.029

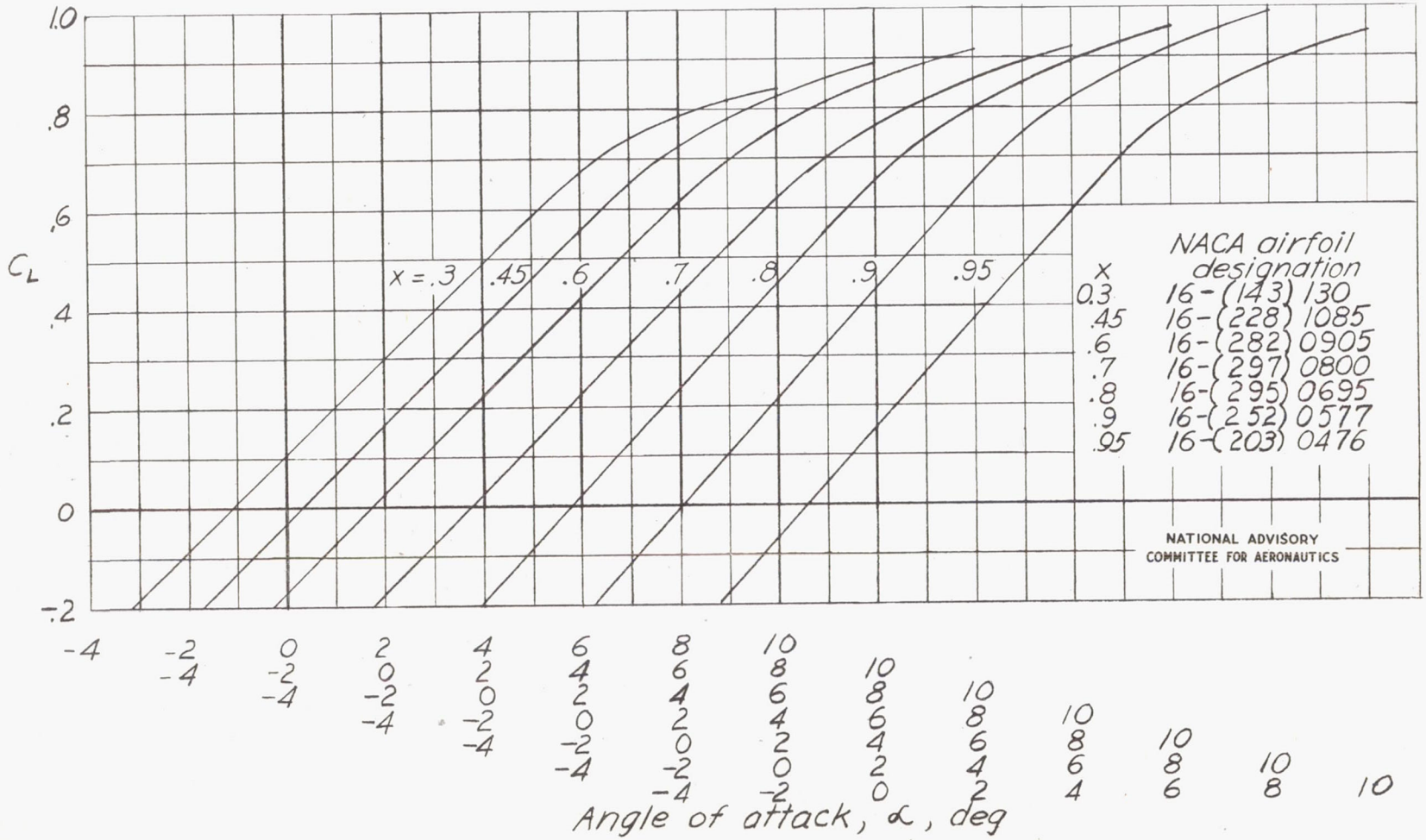
[a]Optimum values are from figures 2 and 3 of reference 2.

NATIONAL ADVISORY
COMMITTEE FOR AERONAUTICS



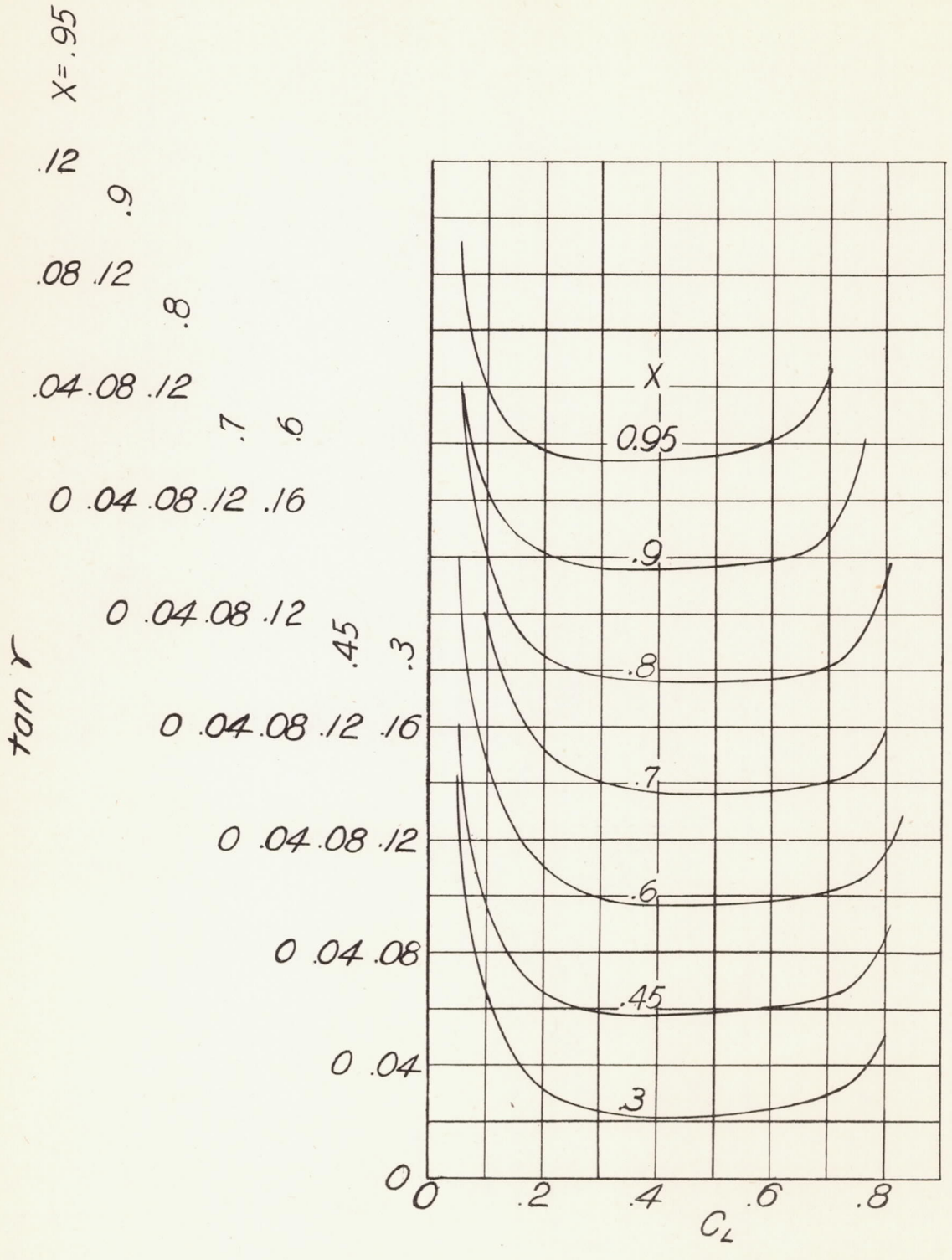
NATIONAL ADVISORY
COMMITTEE FOR AERONAUTICS

Figure 1.- Geometric relation of blade-element forces and velocities.



(a) C_L curves.

Figure 2.- Two-dimensional airfoil characteristics. NACA 10-308-03 propeller sections. Mach number, 0.3.



NATIONAL ADVISORY COMMITTEE FOR AERONAUTICS

(b) Tan γ curves.

Figure 2.- Concluded.



Figure 3.- Photograph of test setup.

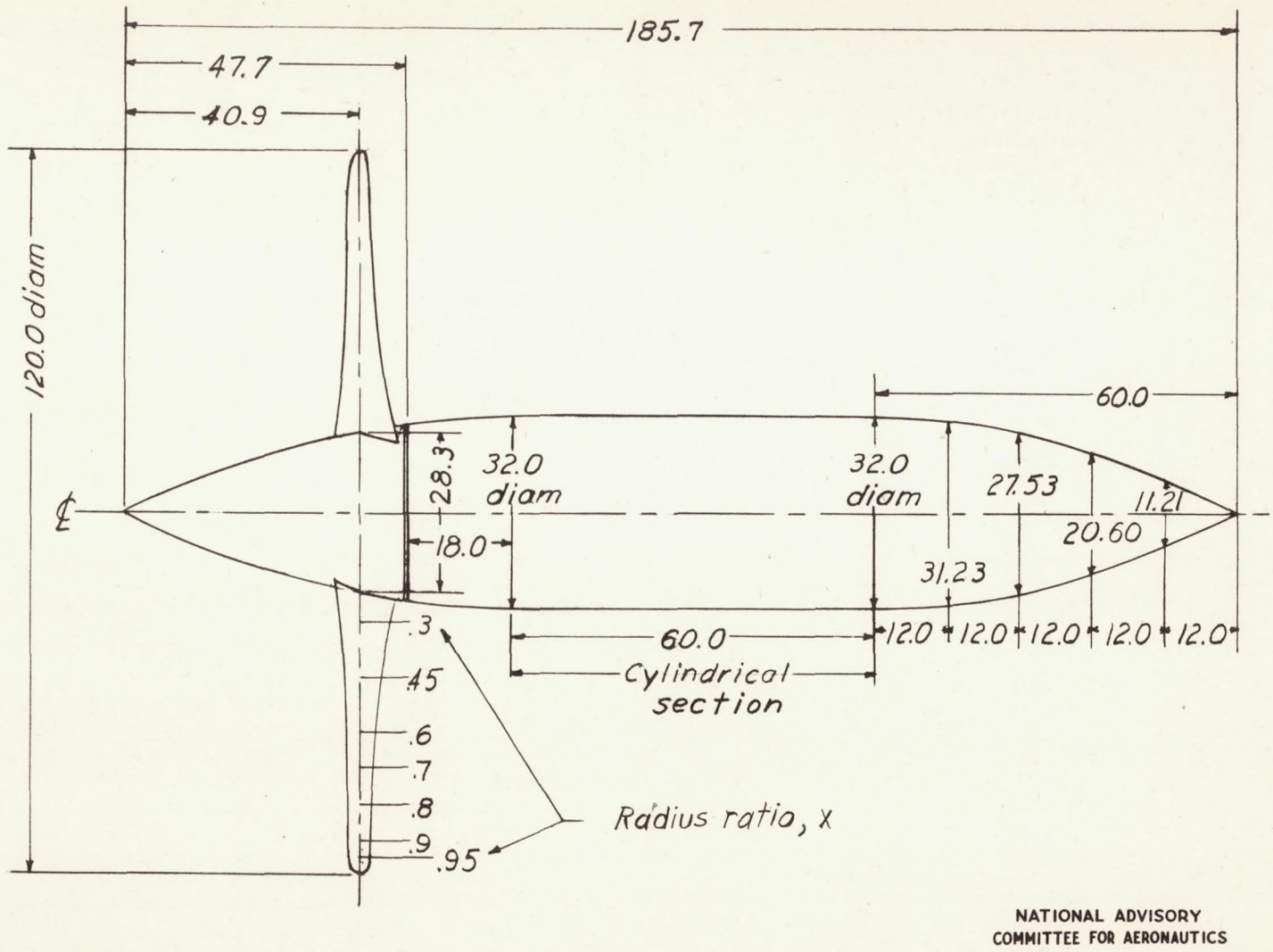


Figure 4.- Dimensional details of test setup. (All dimensions except x are in inches.)

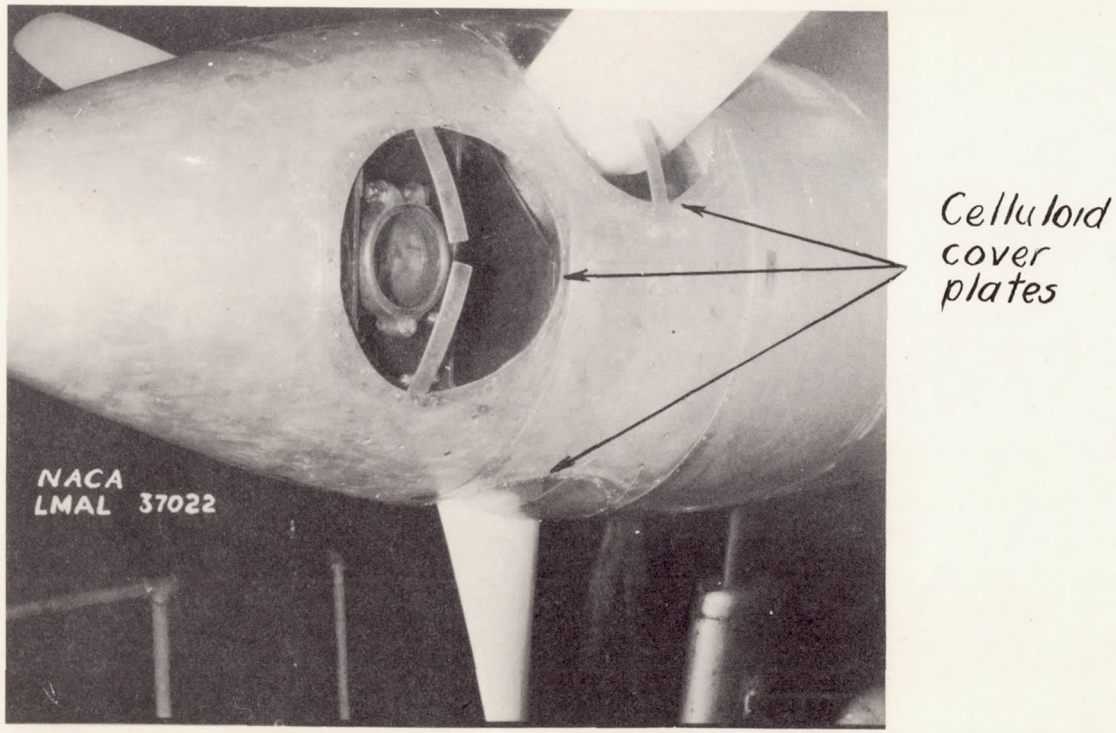


Figure 5.- Close-up showing spinner cut-outs and celluloid cover plates.

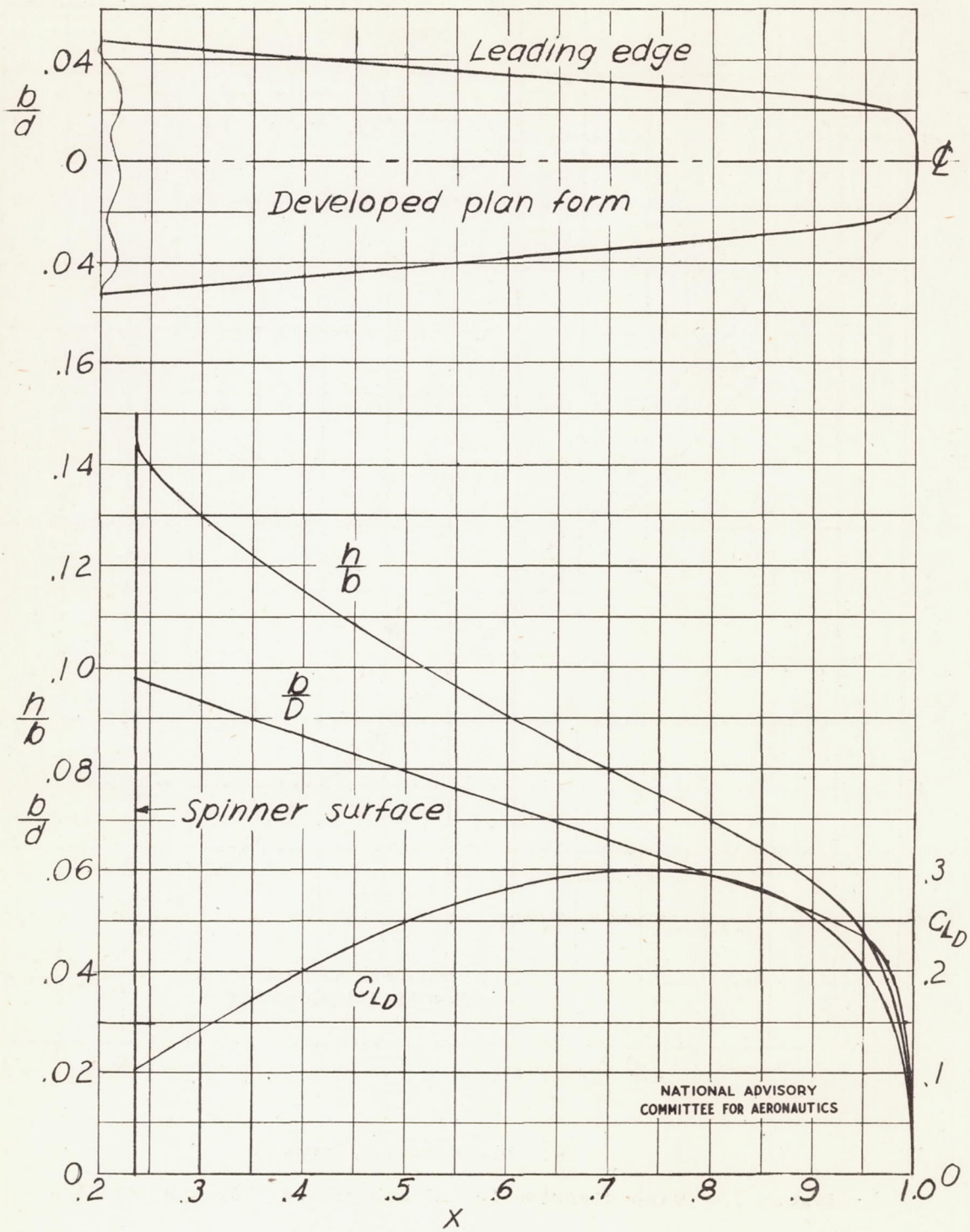
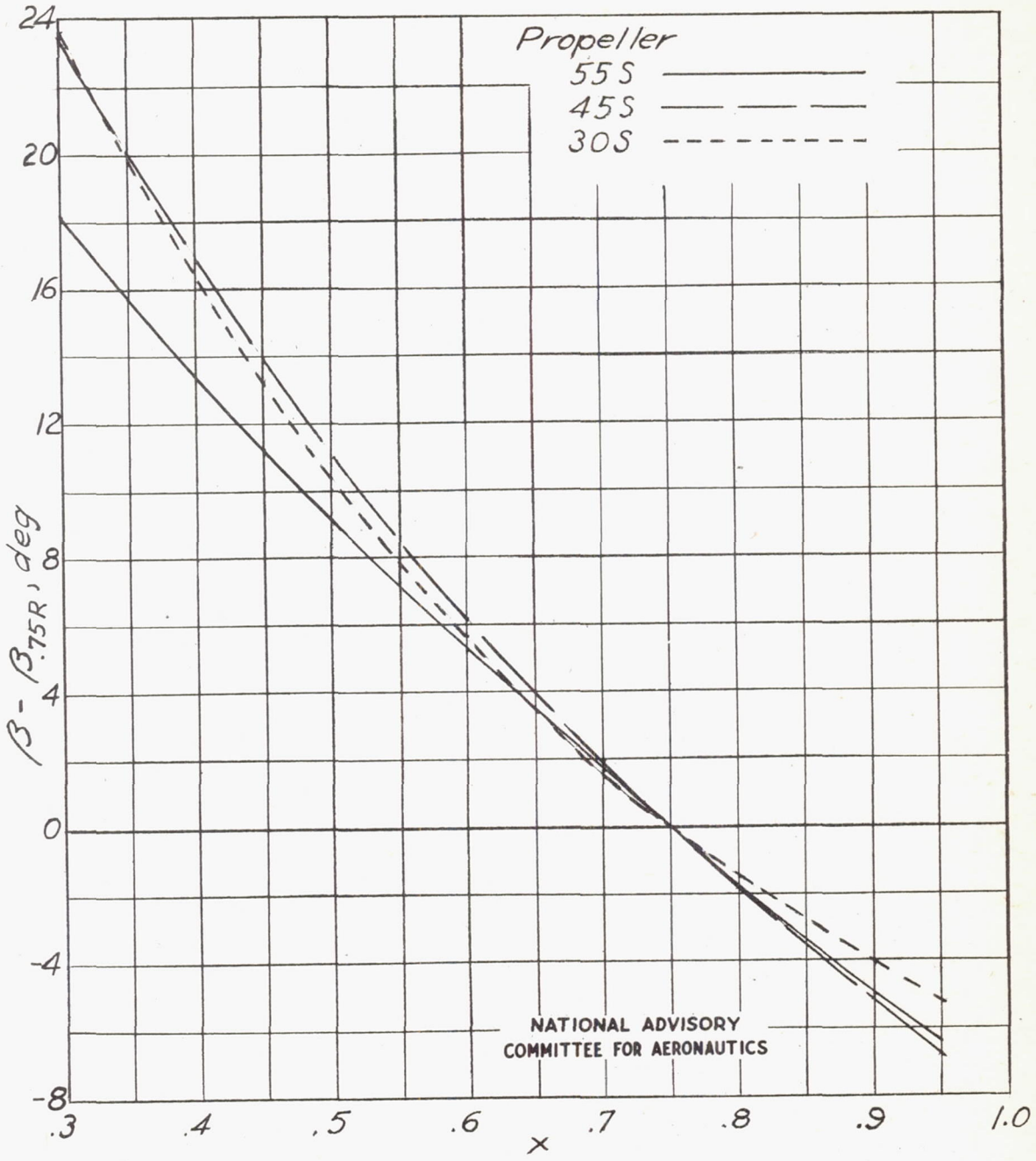
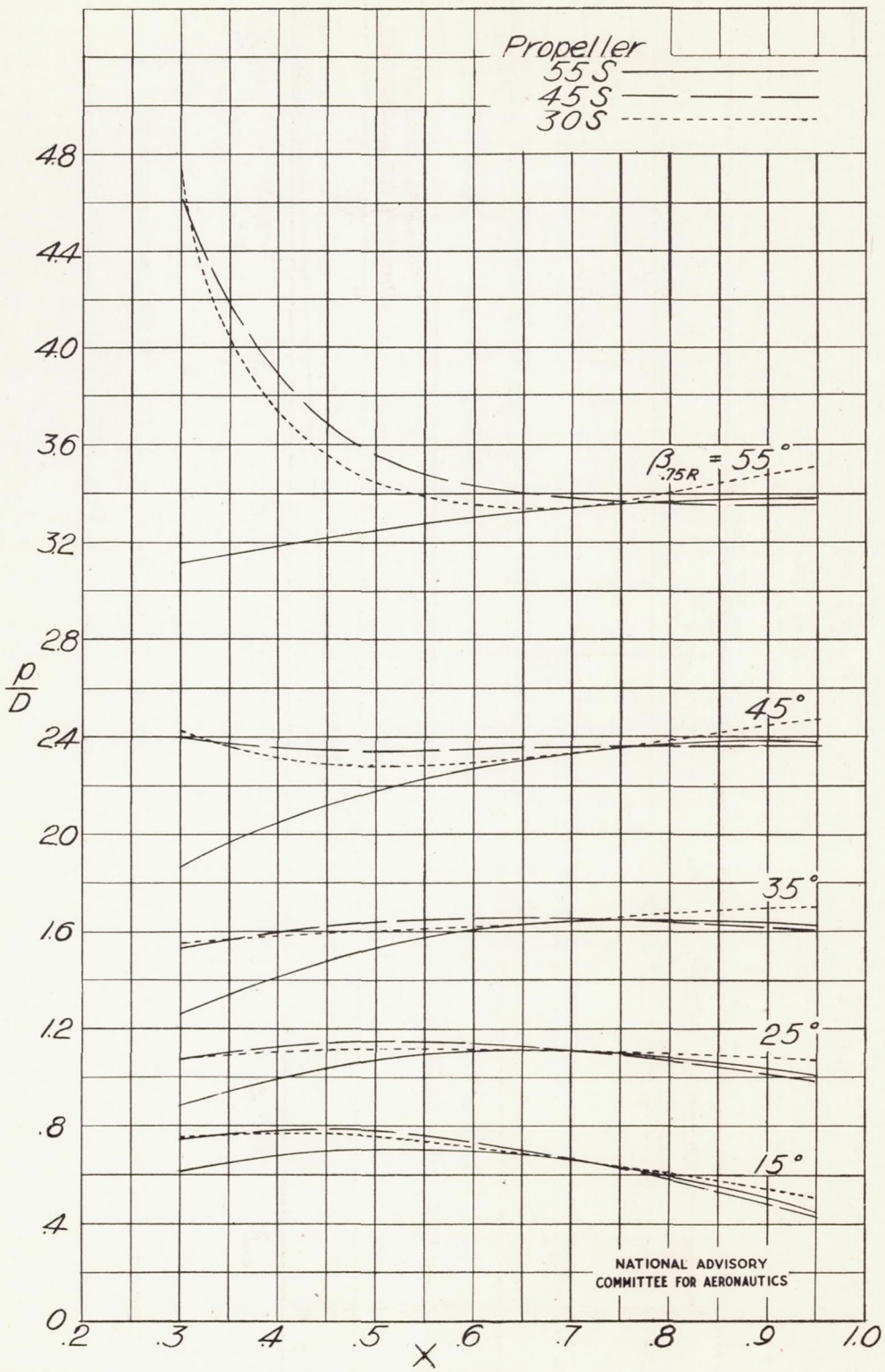


Figure 6.- Blade-form curves and C_{L_D} distribution of NACA propeller 10-308-03.



(a) Blade-twist curves.

Figure 7.- Pitch distribution of propellers 55S, 45S, and 30S.



(b) Geometric-pitch curves.

Figure 7.- Concluded.

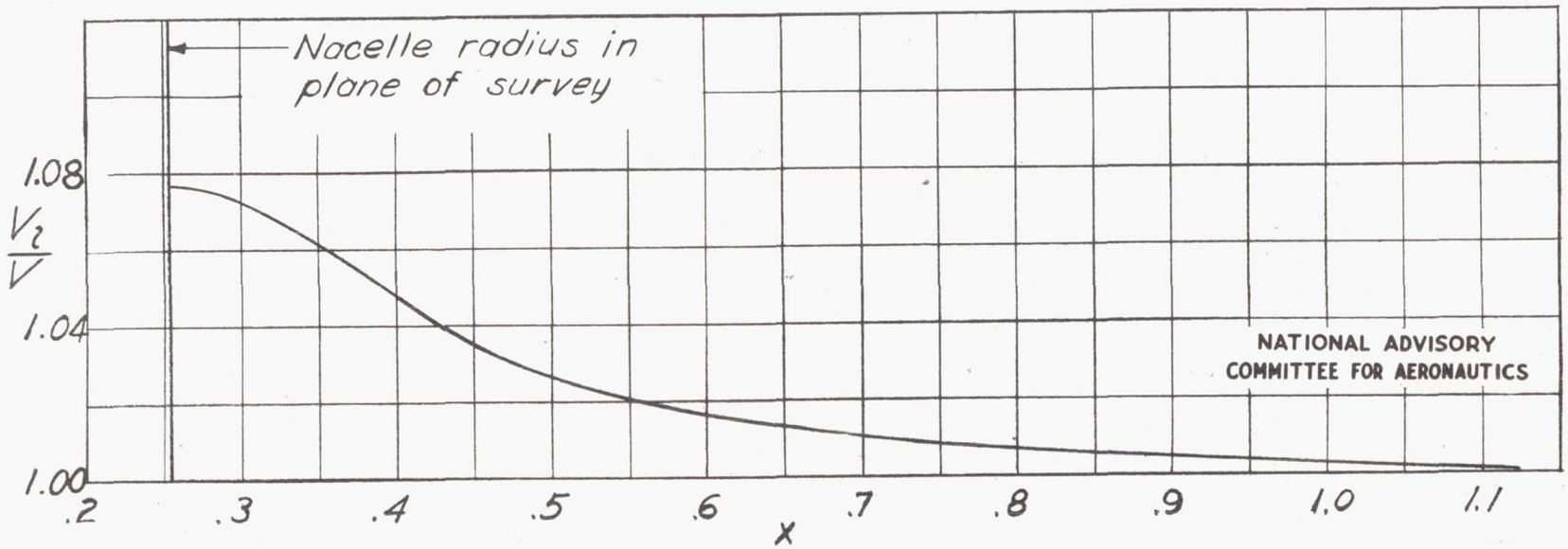
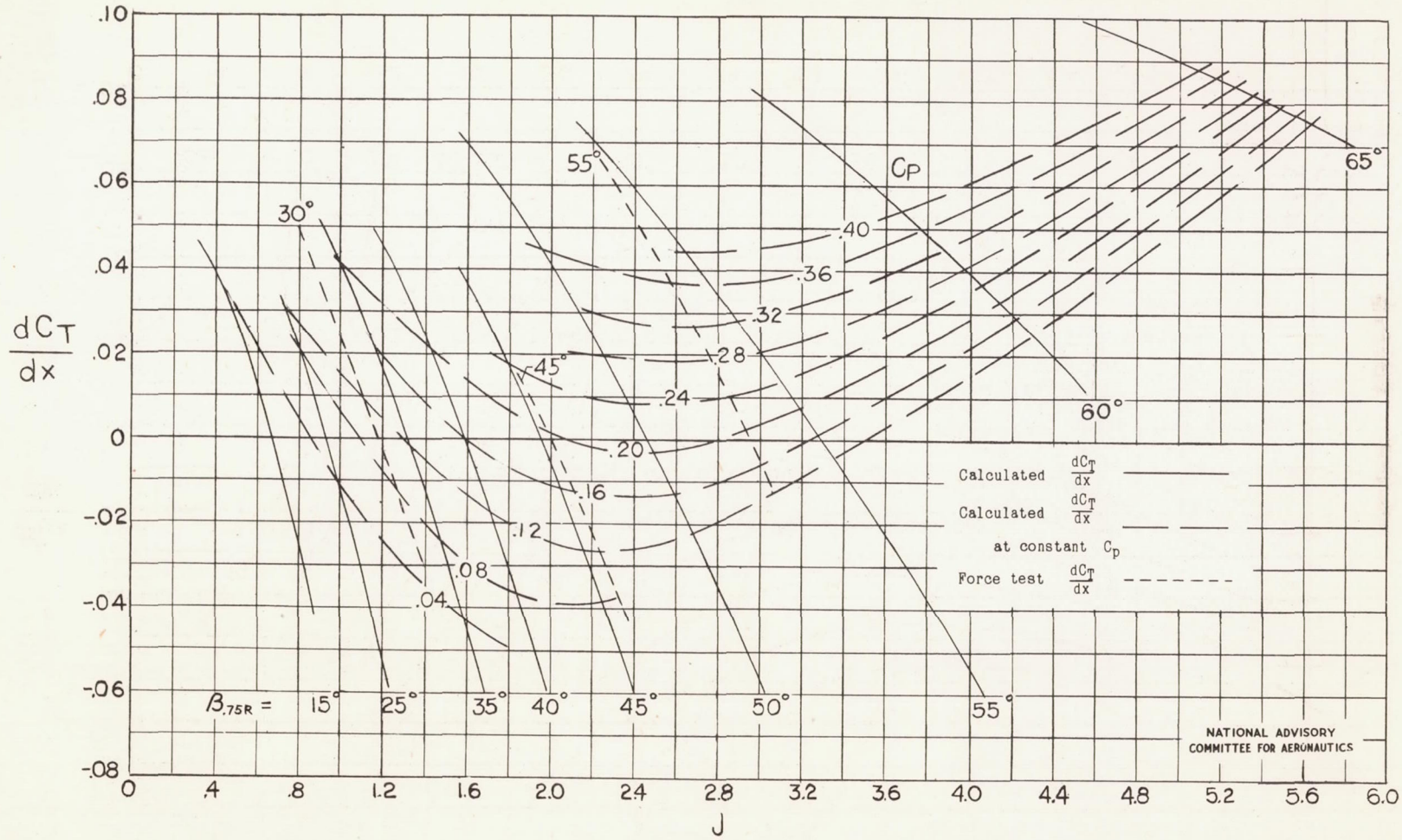
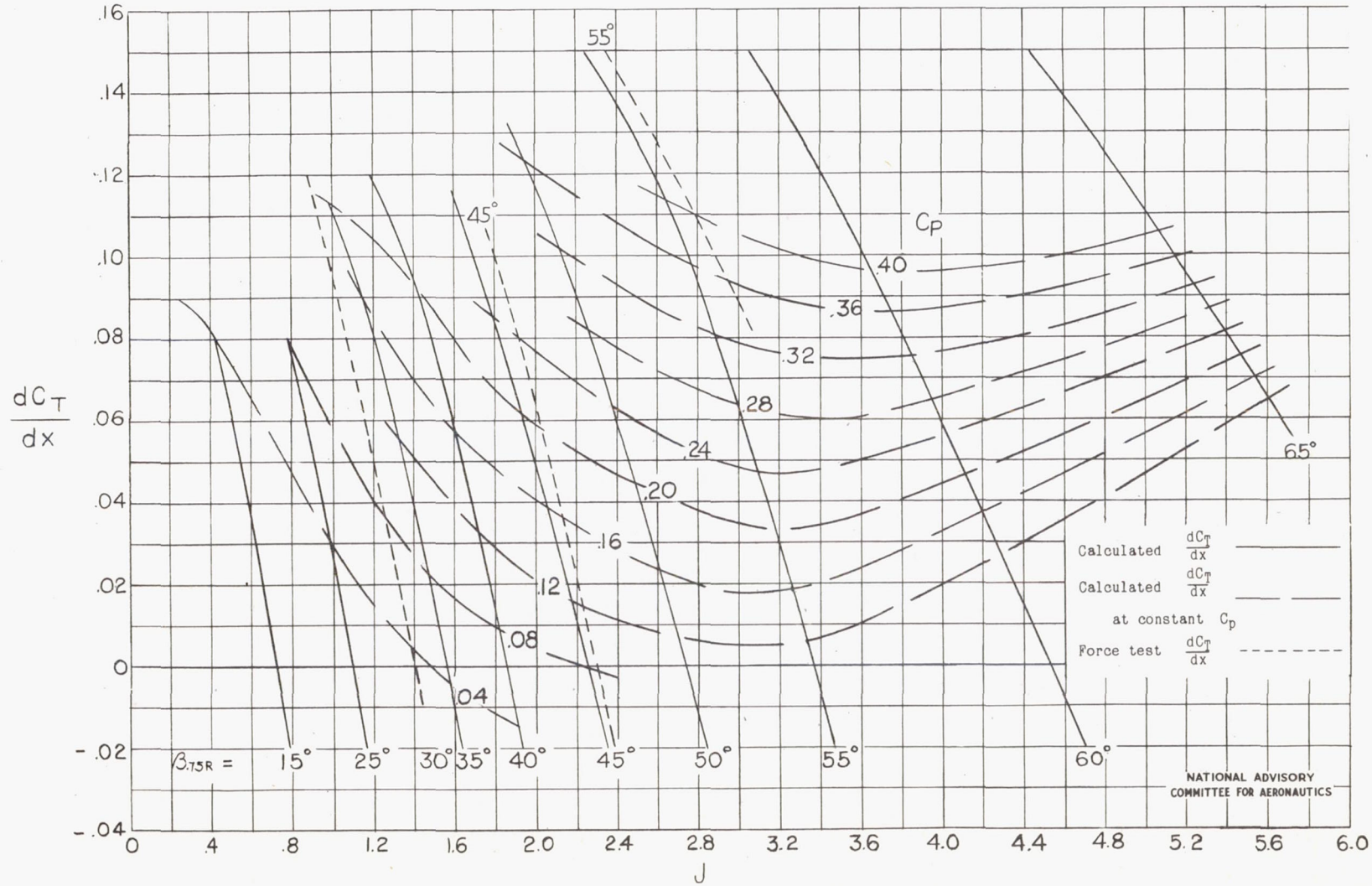


Figure 8.- Velocity distribution $7\frac{1}{2}$ inches behind propeller disk. Propeller removed.



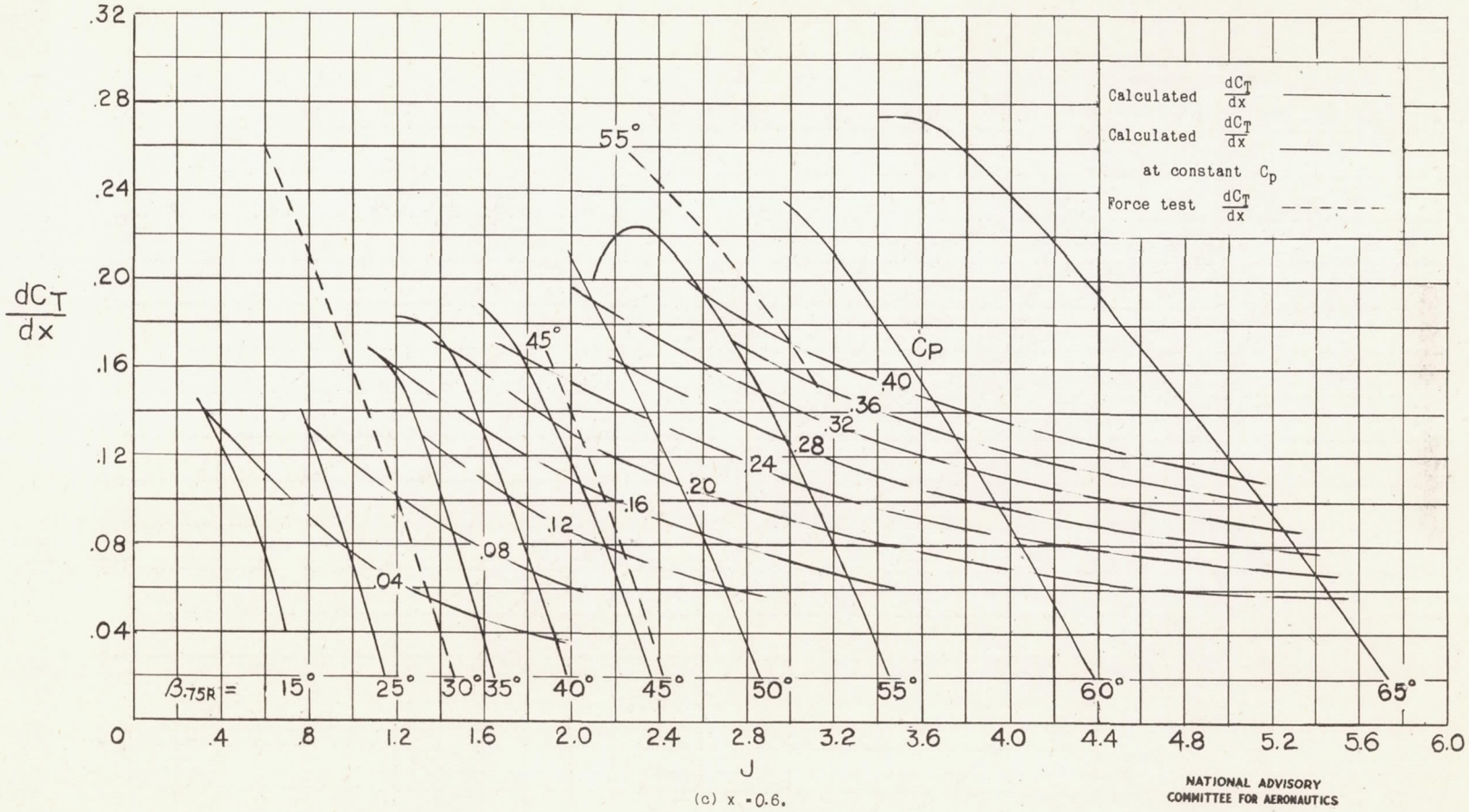
(a) x = 0.3.

Figure 9.- Element thrust coefficients. Propeller 55S.



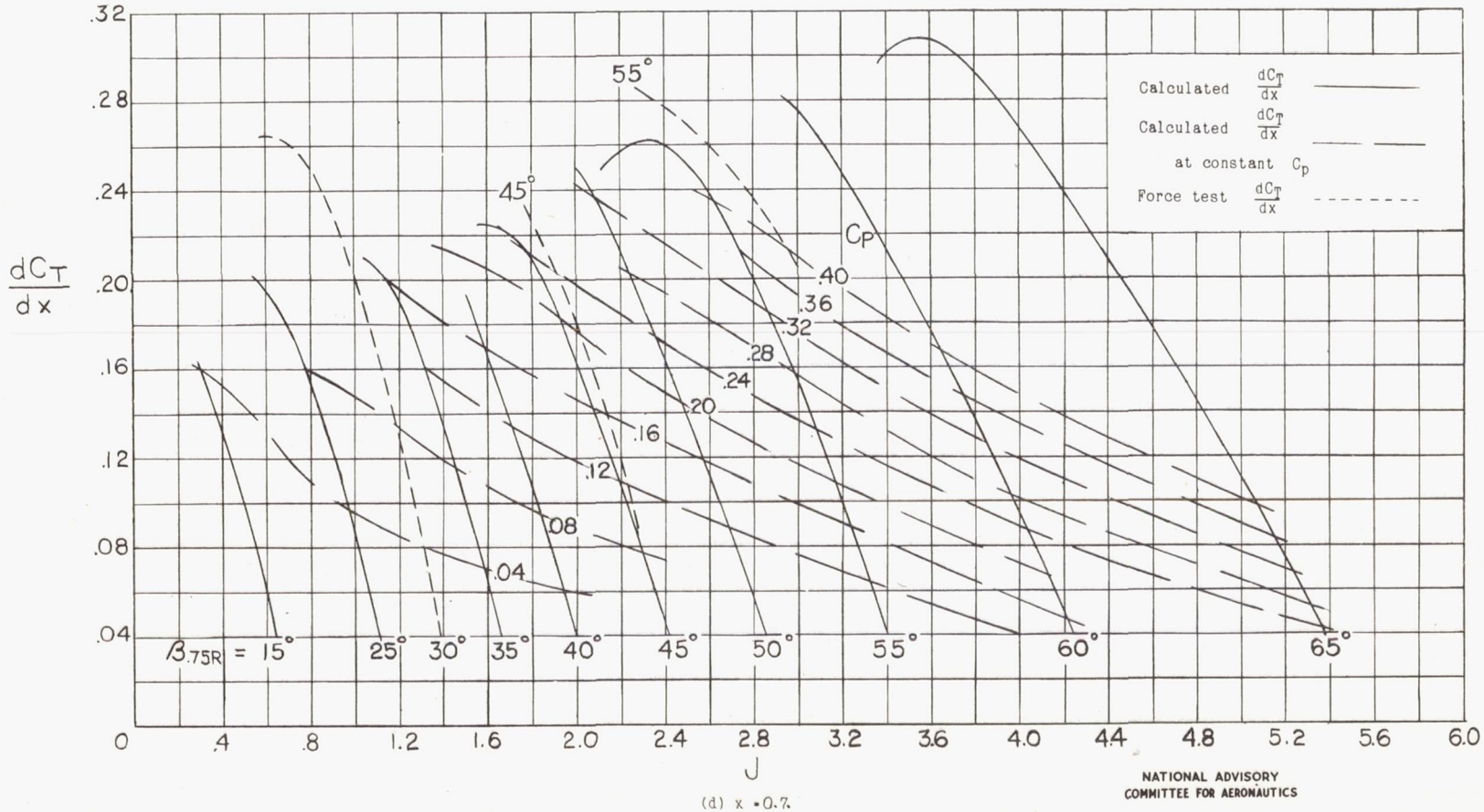
(b) x -0.45.

Figure 9.- Continued.



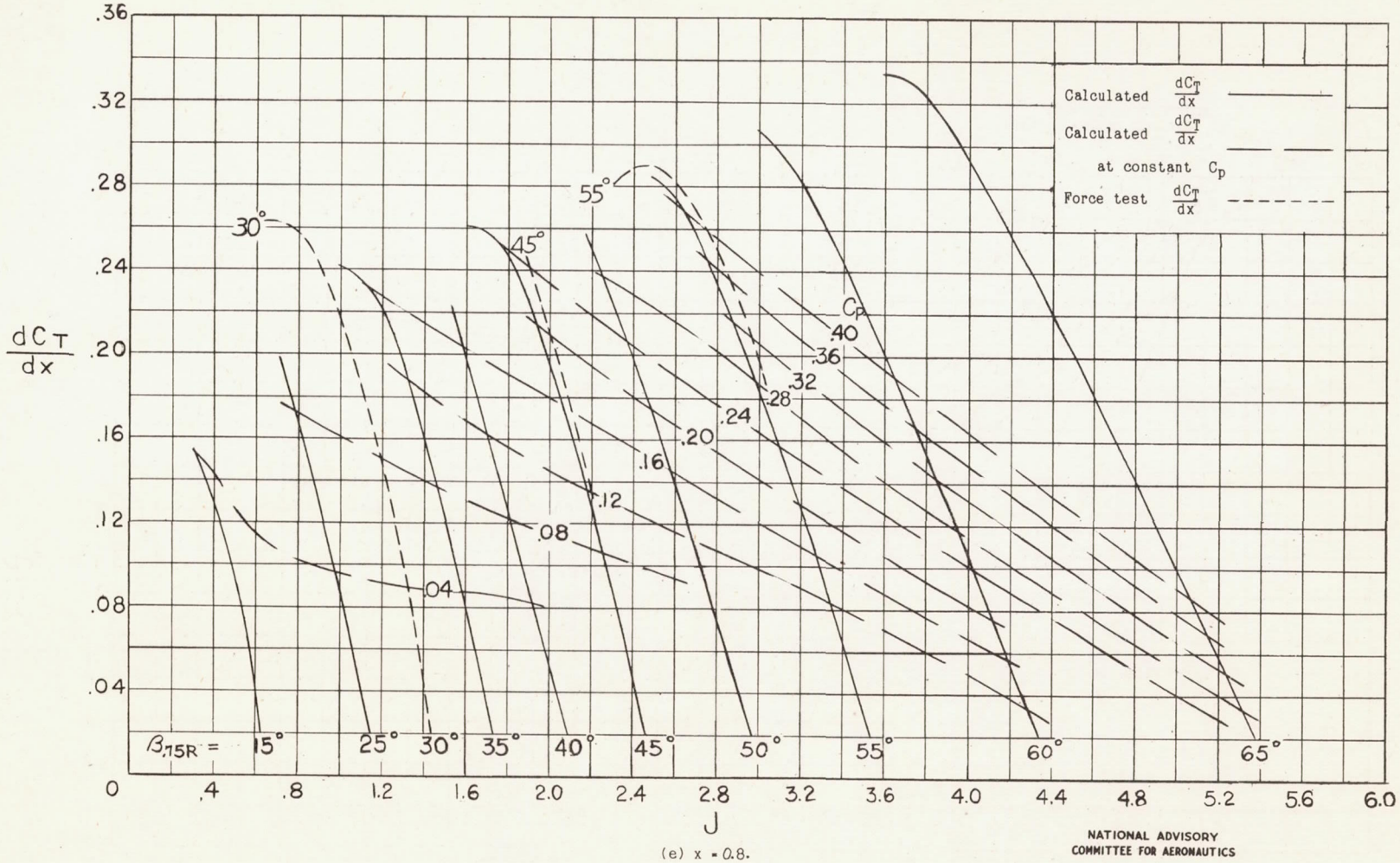
(c) x -0.6.

Figure 9.- Continued.



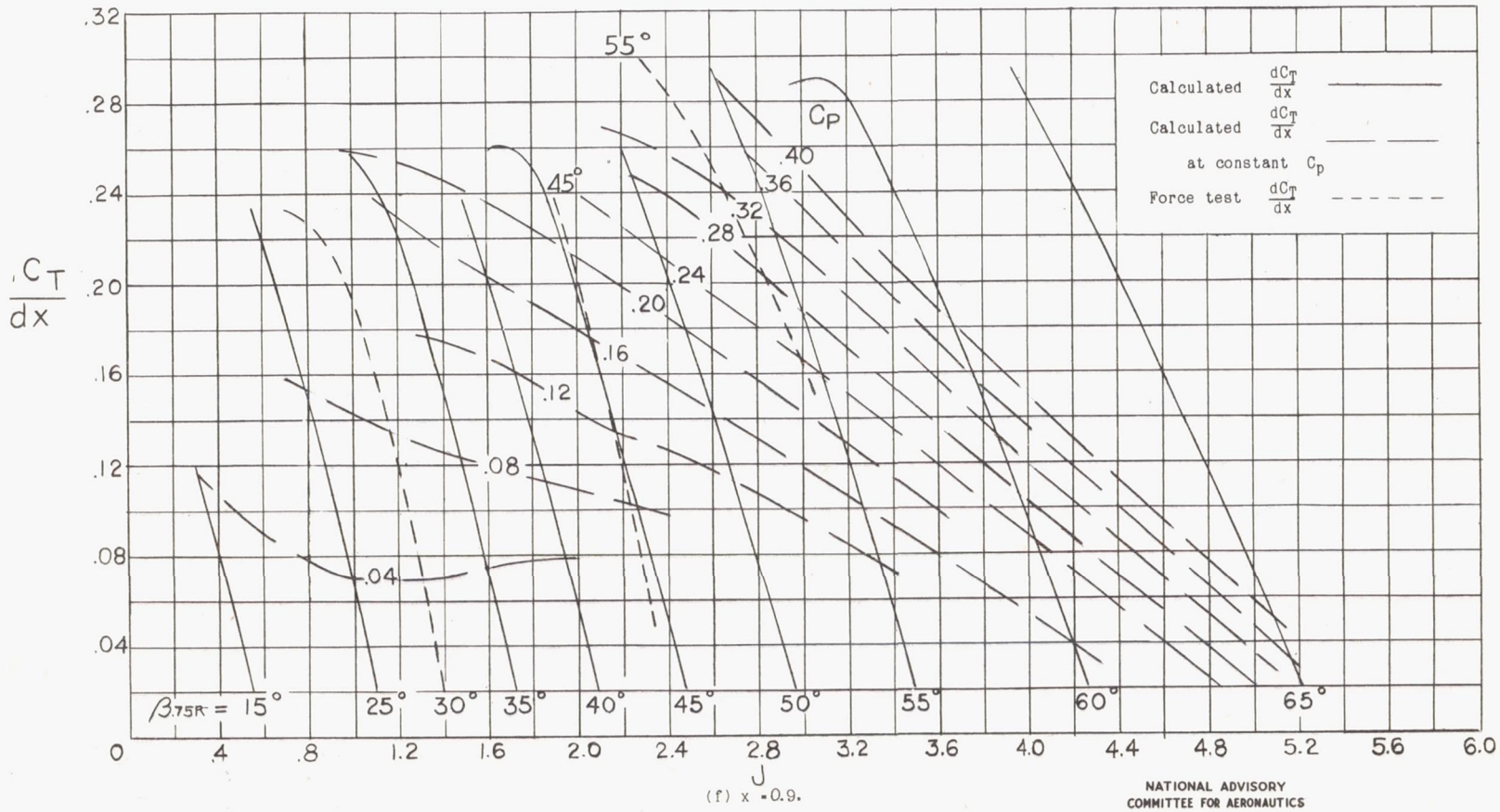
(d) x = 0.7.

Figure 9.- Continued.



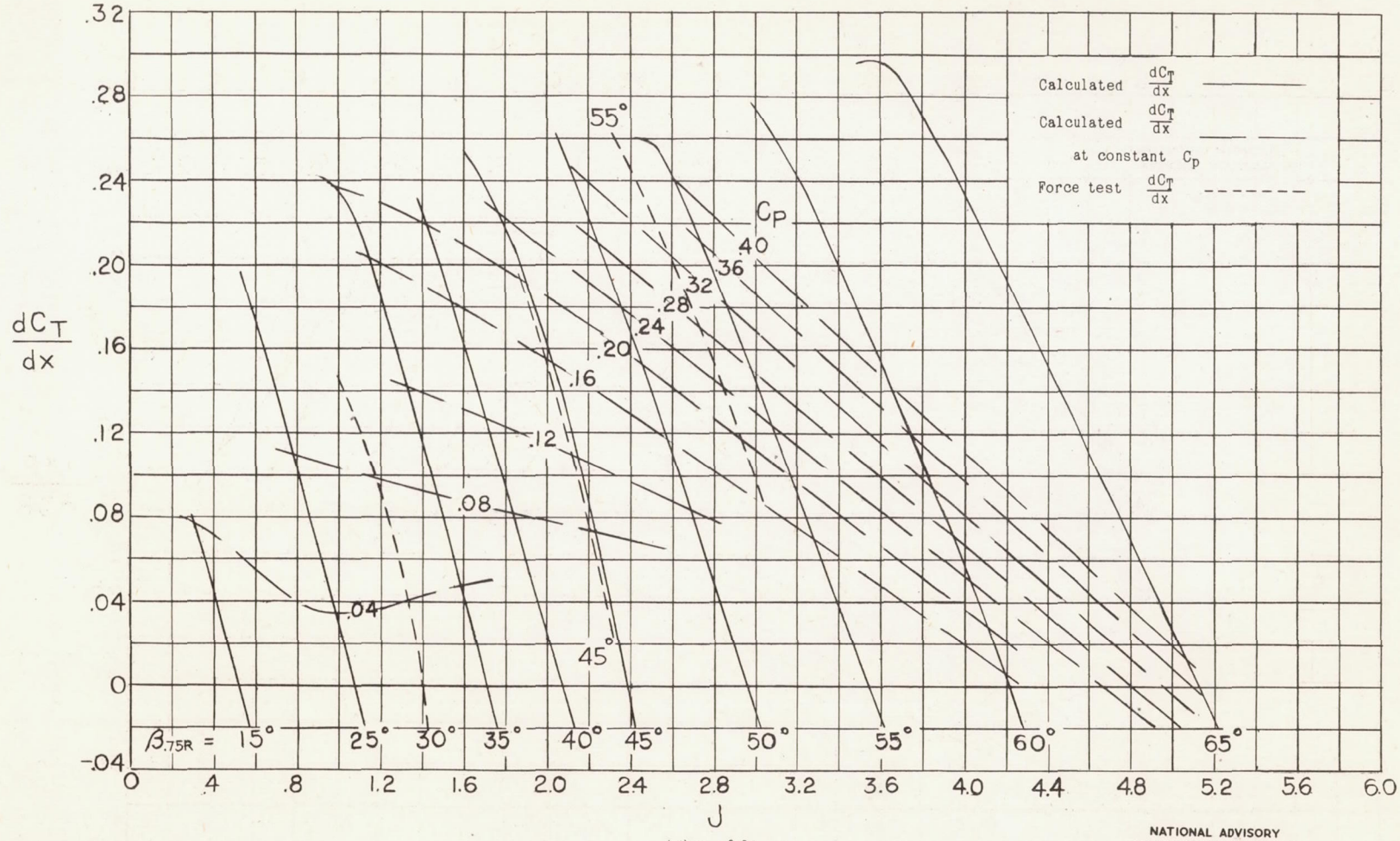
(e) x = 0.8.

Figure 9.- Continued.



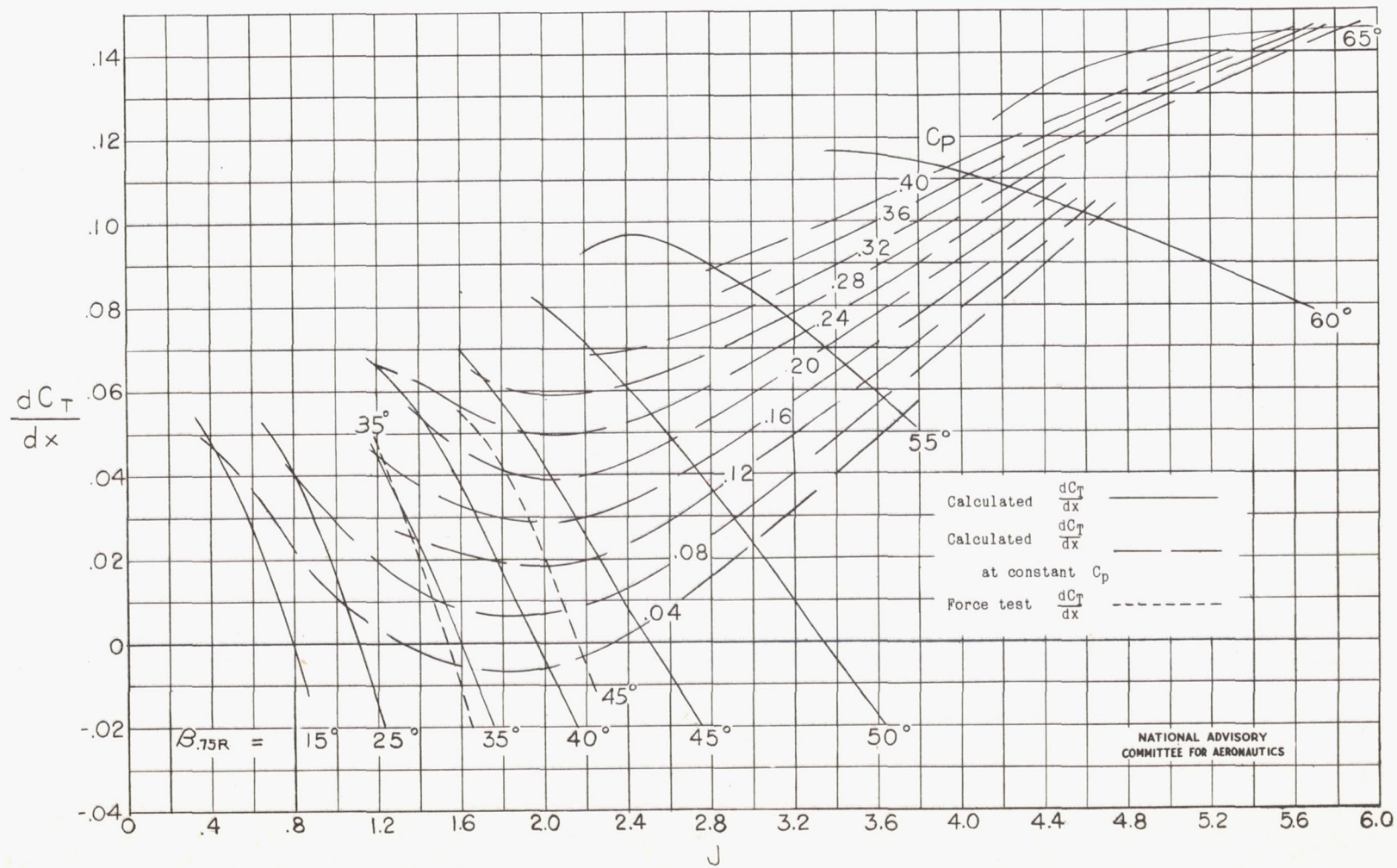
(f) x = 0.9.

Figure 9.- Continued.



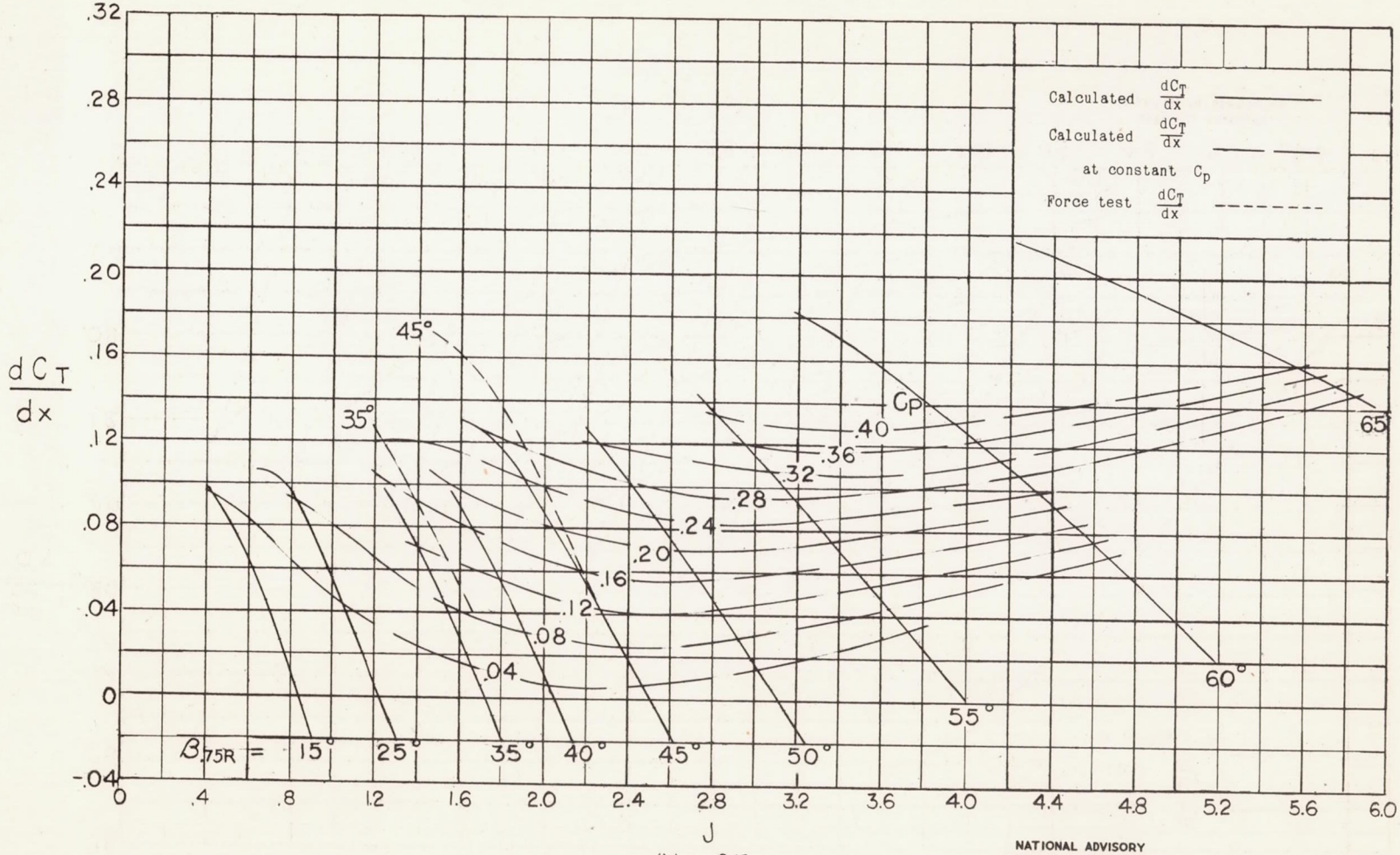
(g) x = 0.95.

Figure 9.- Concluded.



(a) x = 0.3.

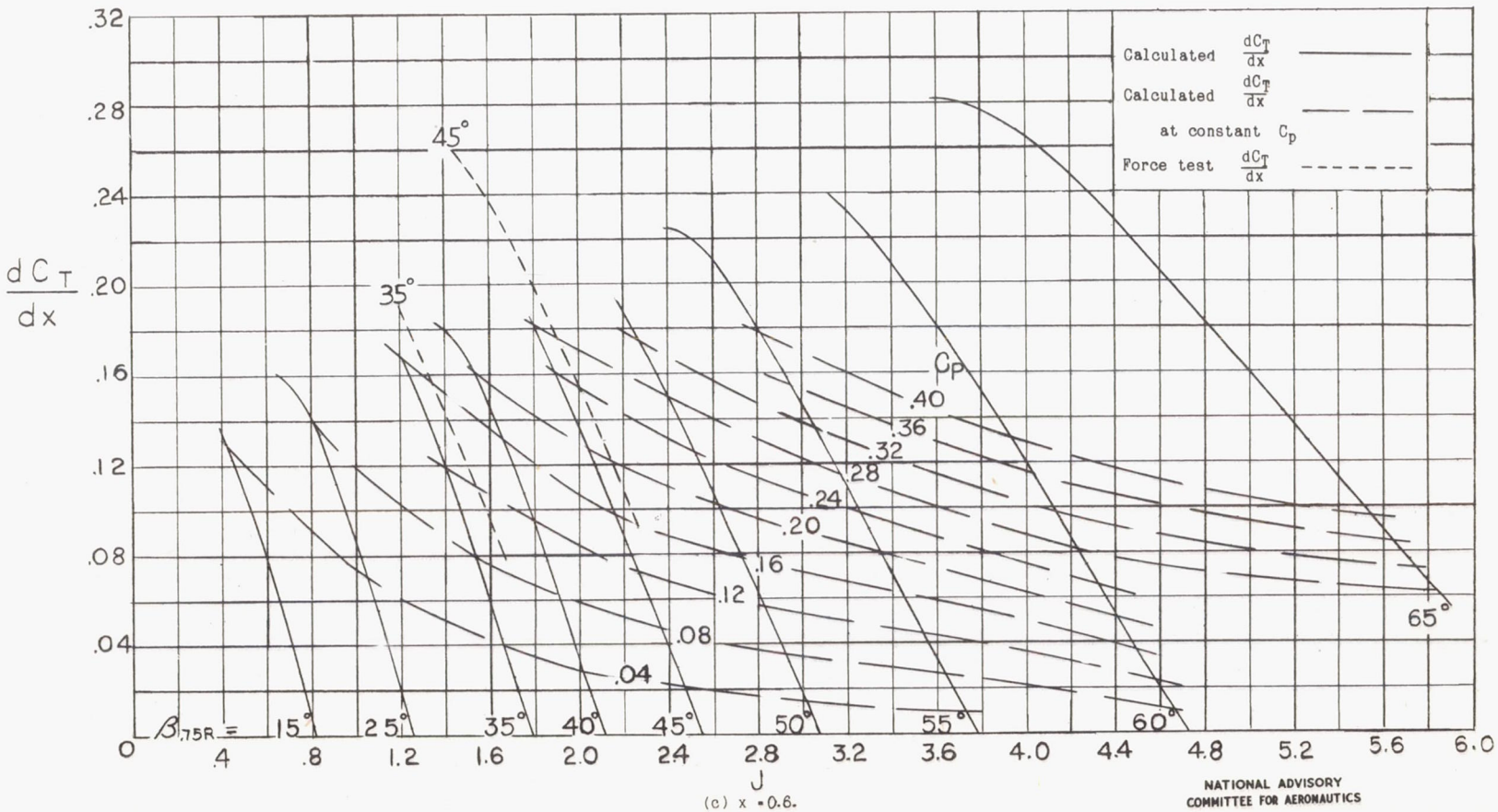
Figure 10. - Element thrust coefficients. Propeller 45S.



NATIONAL ADVISORY COMMITTEE FOR AERONAUTICS

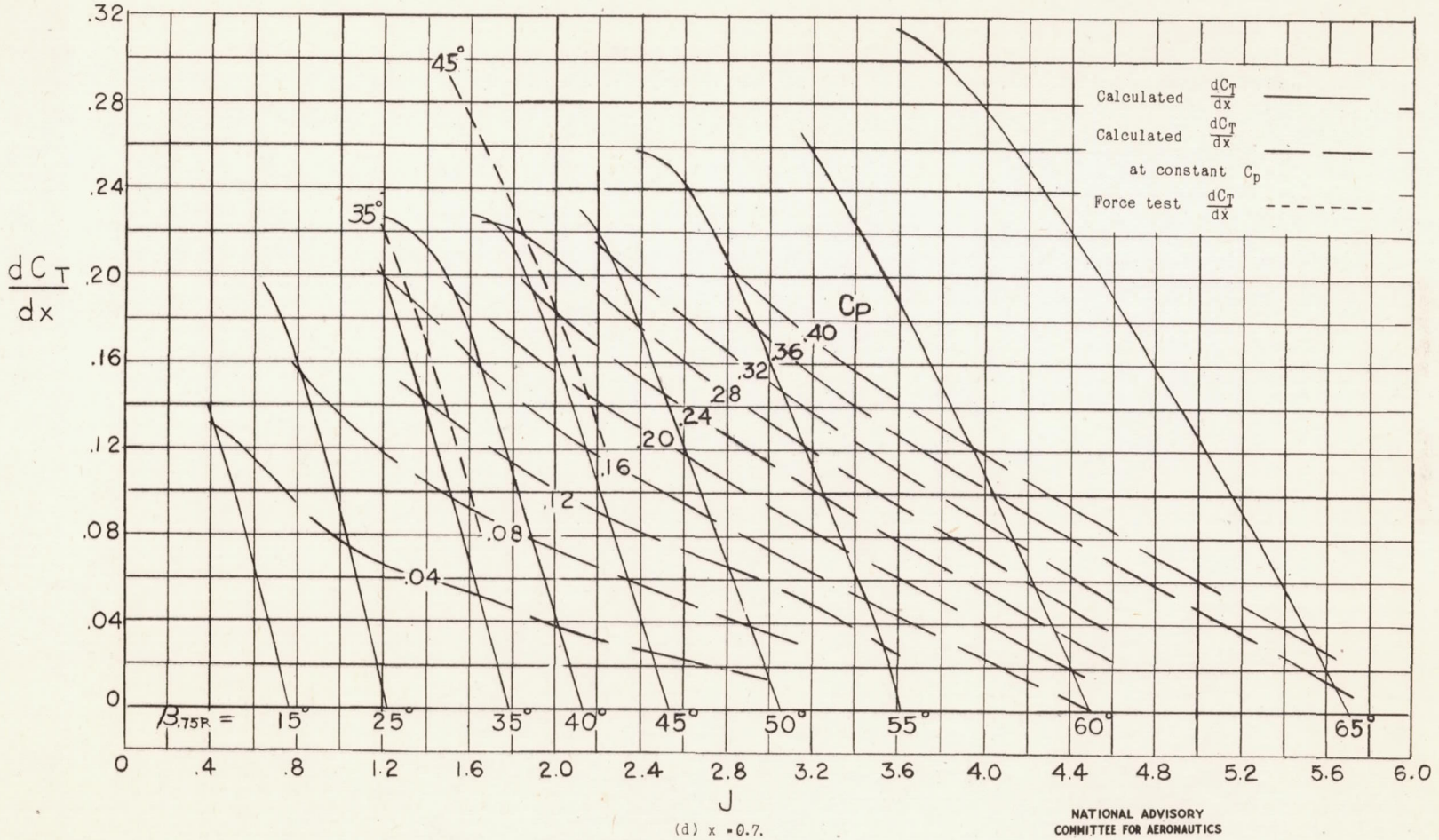
(b) x = 0.45.

Figure 10. - Continued.



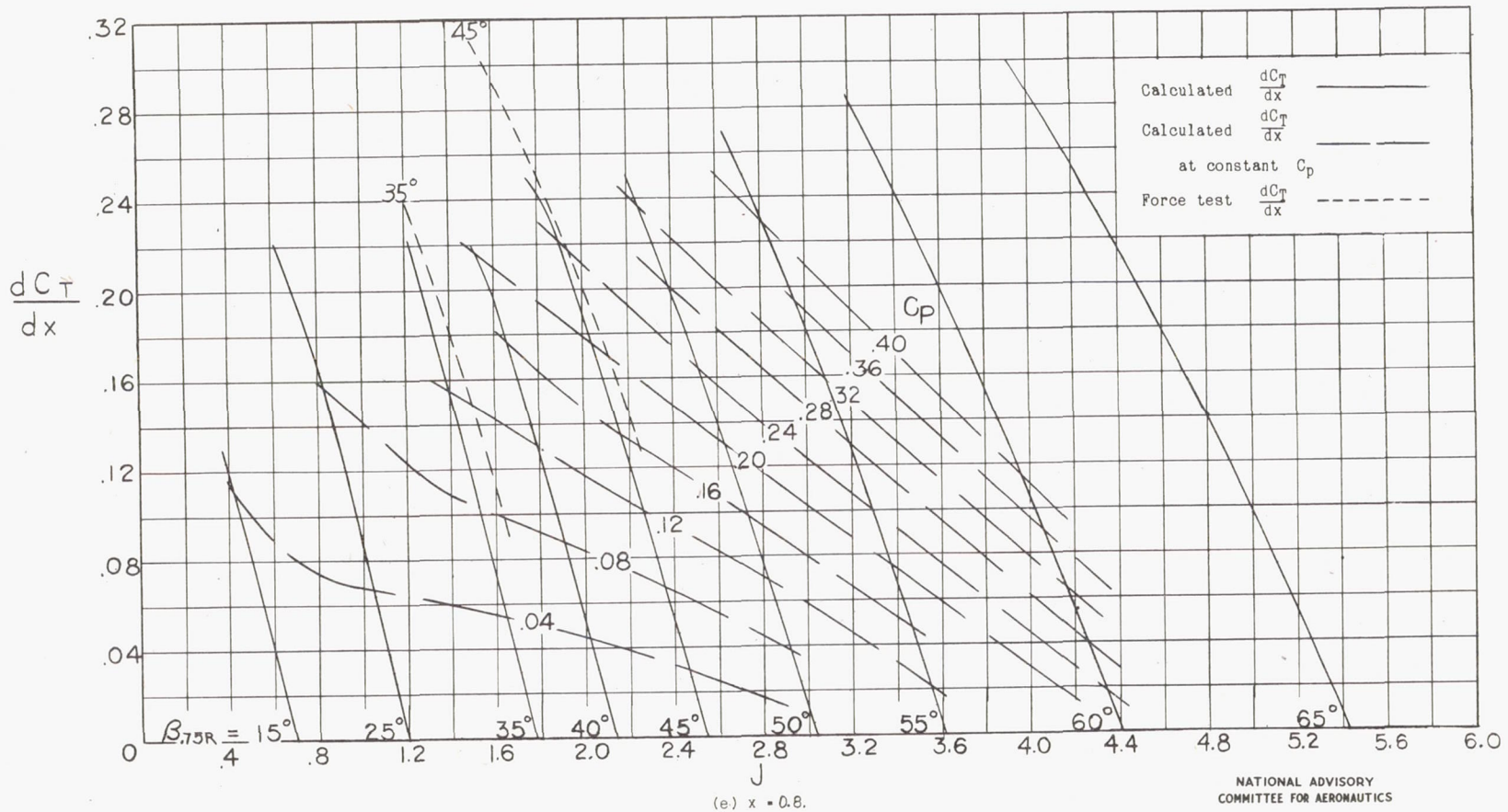
(c) x = 0.6.

Figure 10. - Continued.



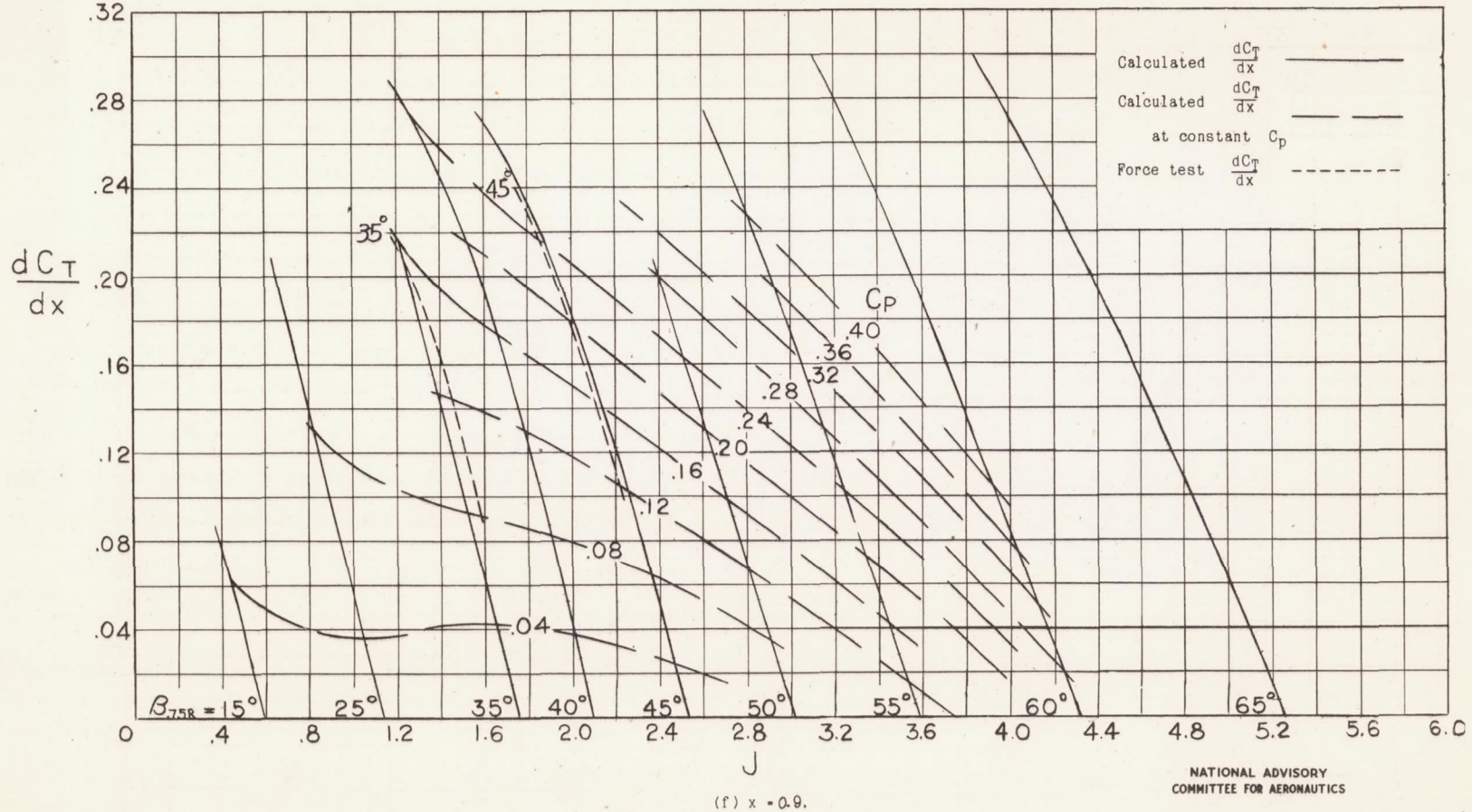
(d) x = 0.7.

Figure 10. - Continued.



(e) x = 0.8.

Figure 10.- Continued.



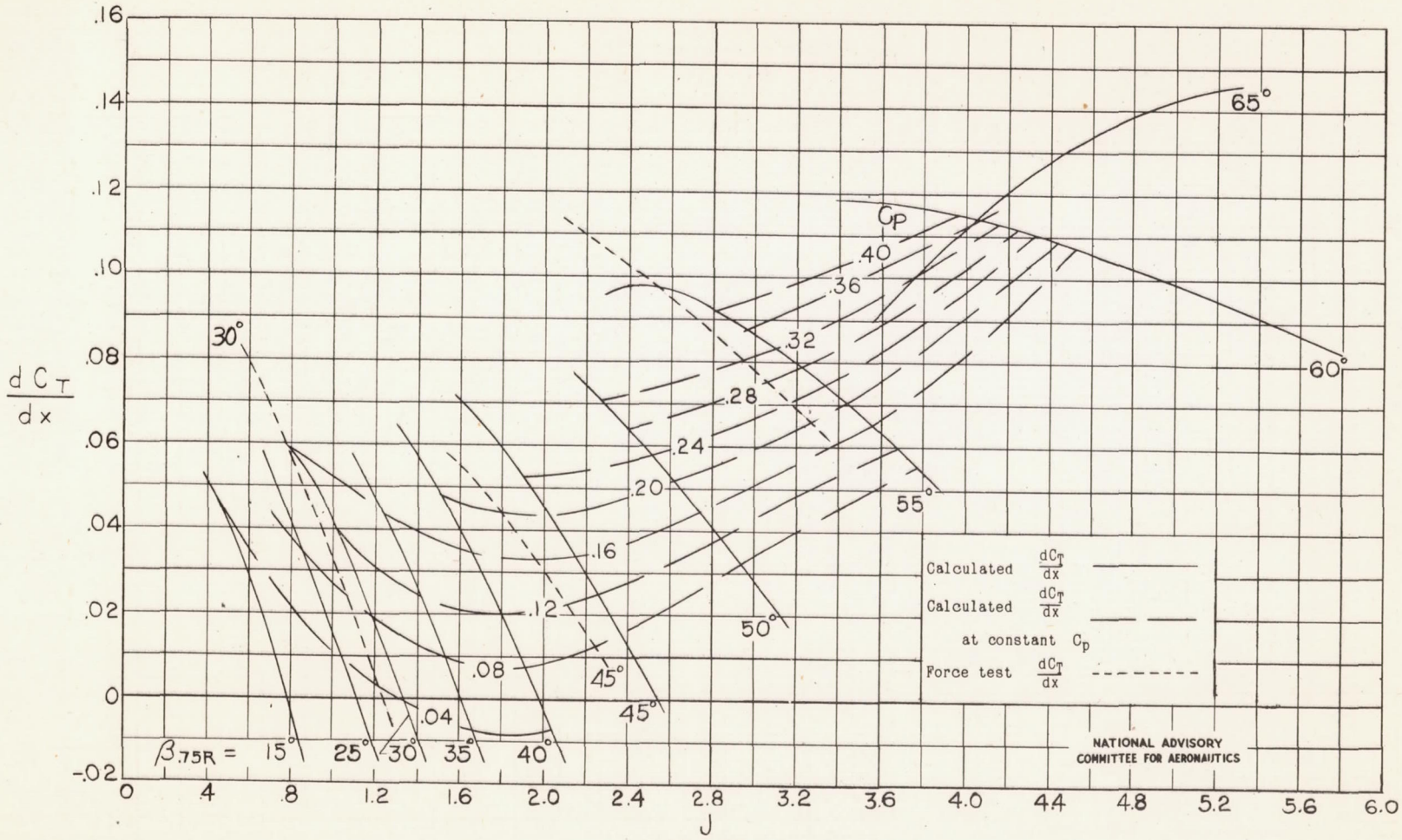
(f) x = 0.9.

Figure 10. - Continued.



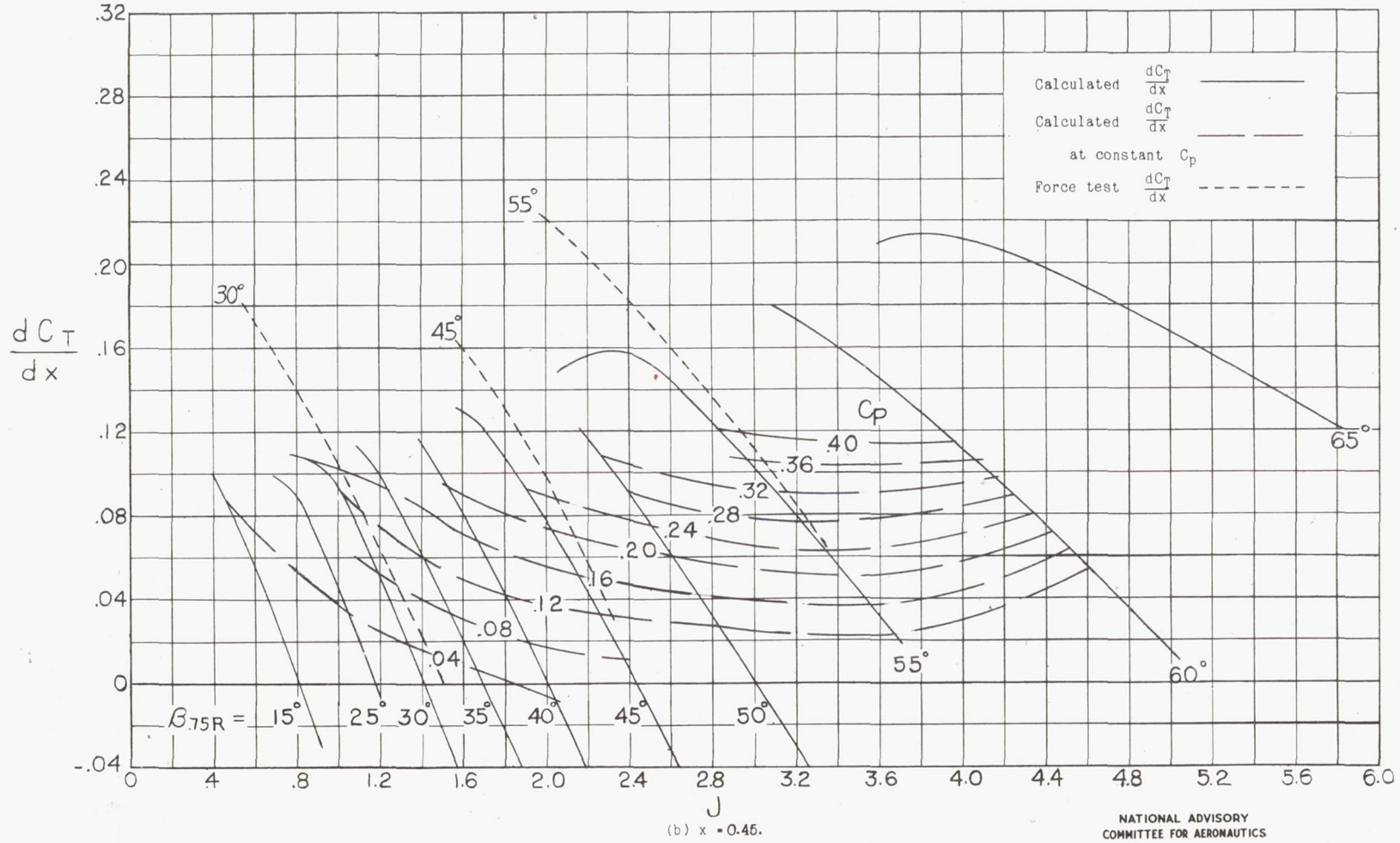
(g) $x = 0.95$.

Figure 10.- Concluded.



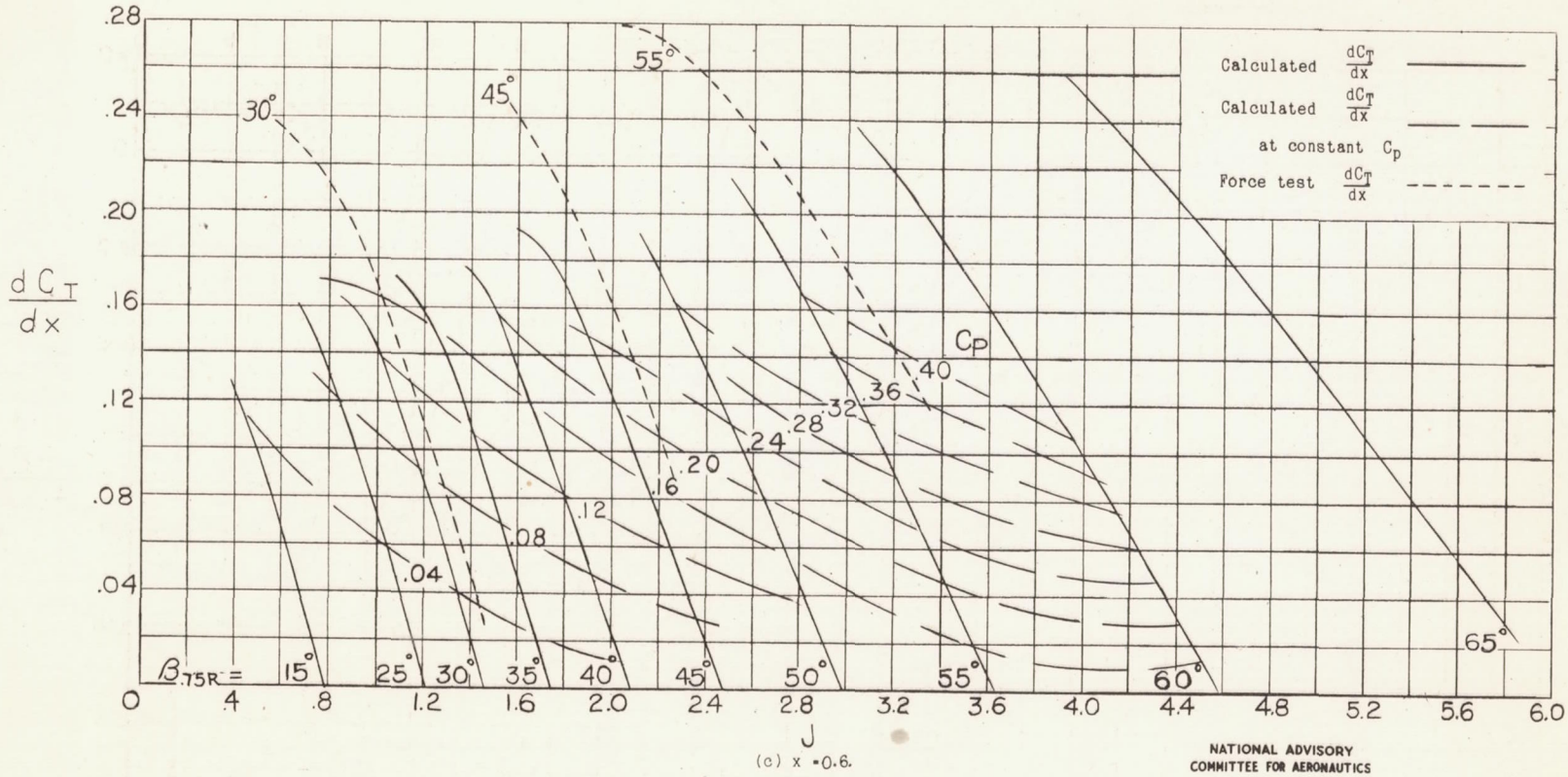
(a) x = 0.3.

Figure 11.- Element thrust coefficient.. Propeller 30S.



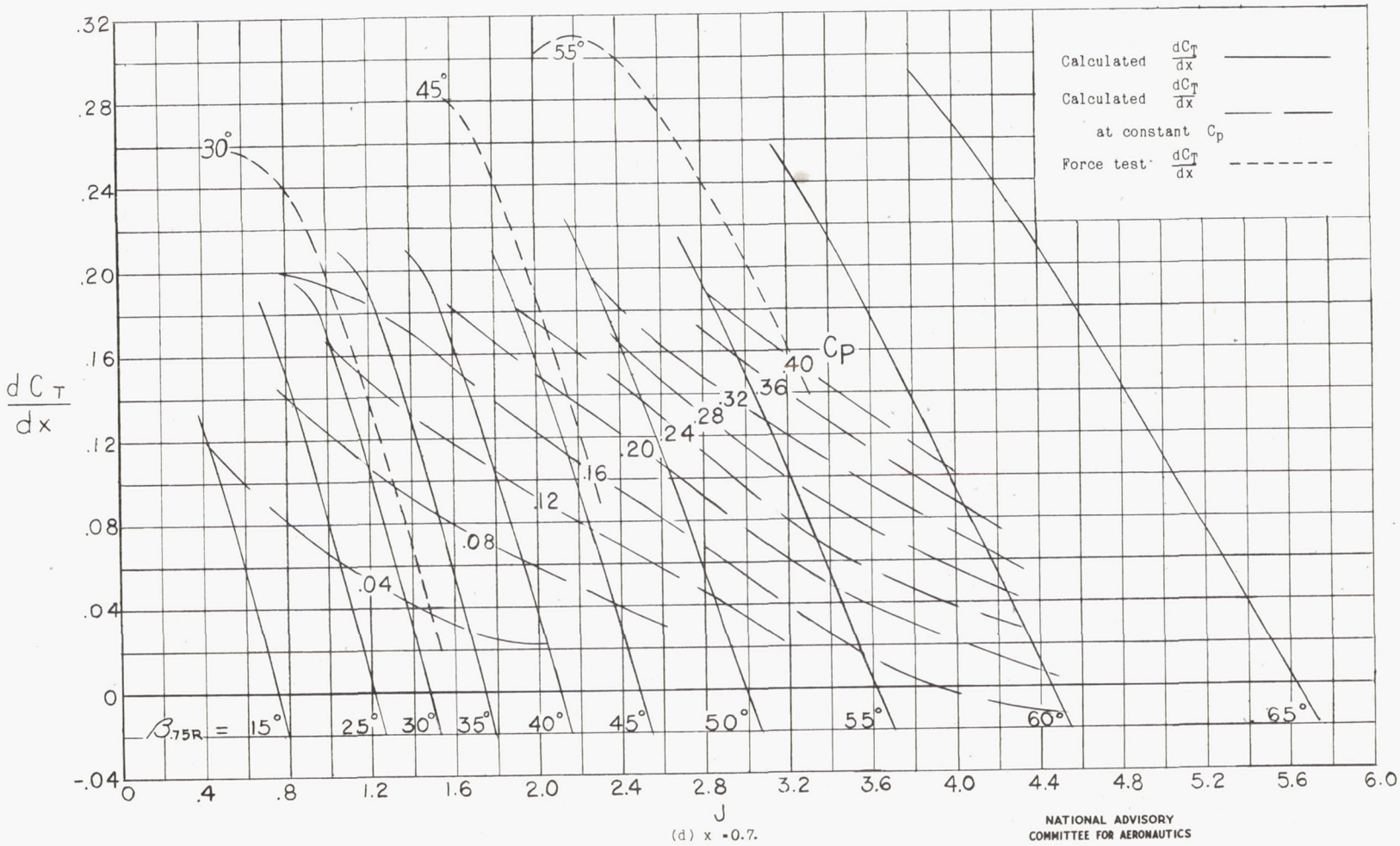
(b) x = 0.45.

Figure 11.- Continued.



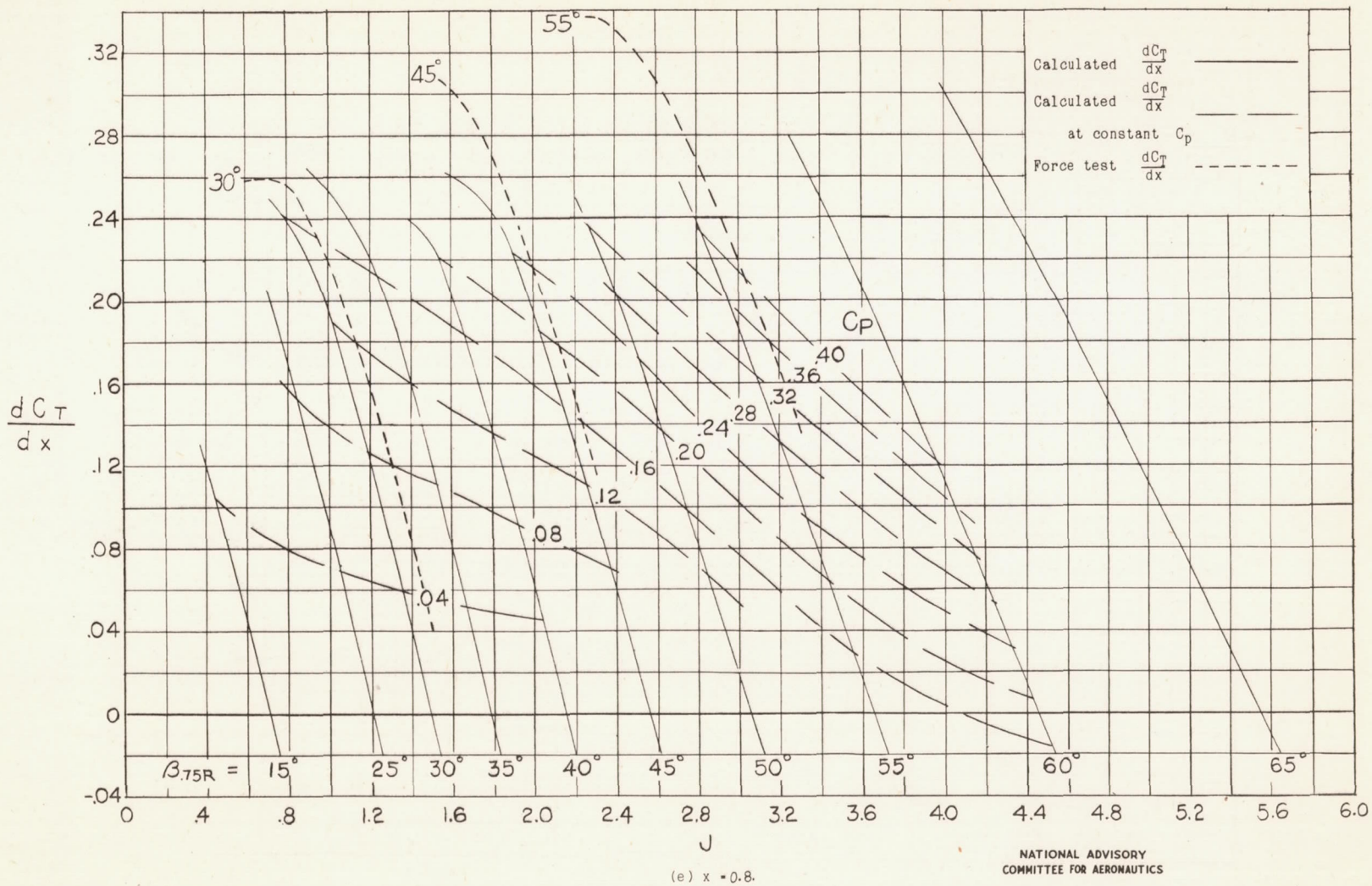
(c) x = 0.6.

Figure 11. - Continued.



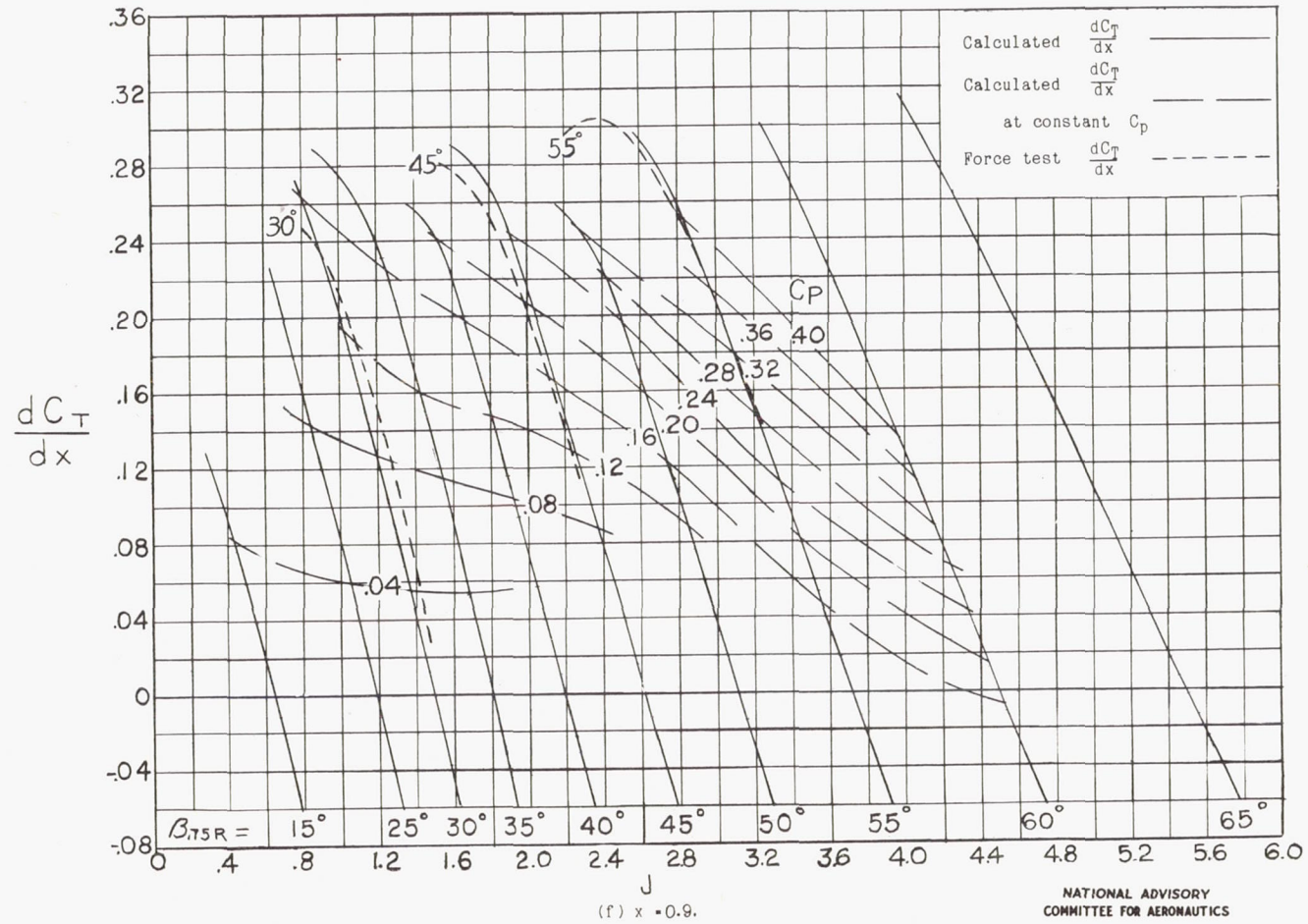
(d) x = 0.7.

Figure 11.- Continued.



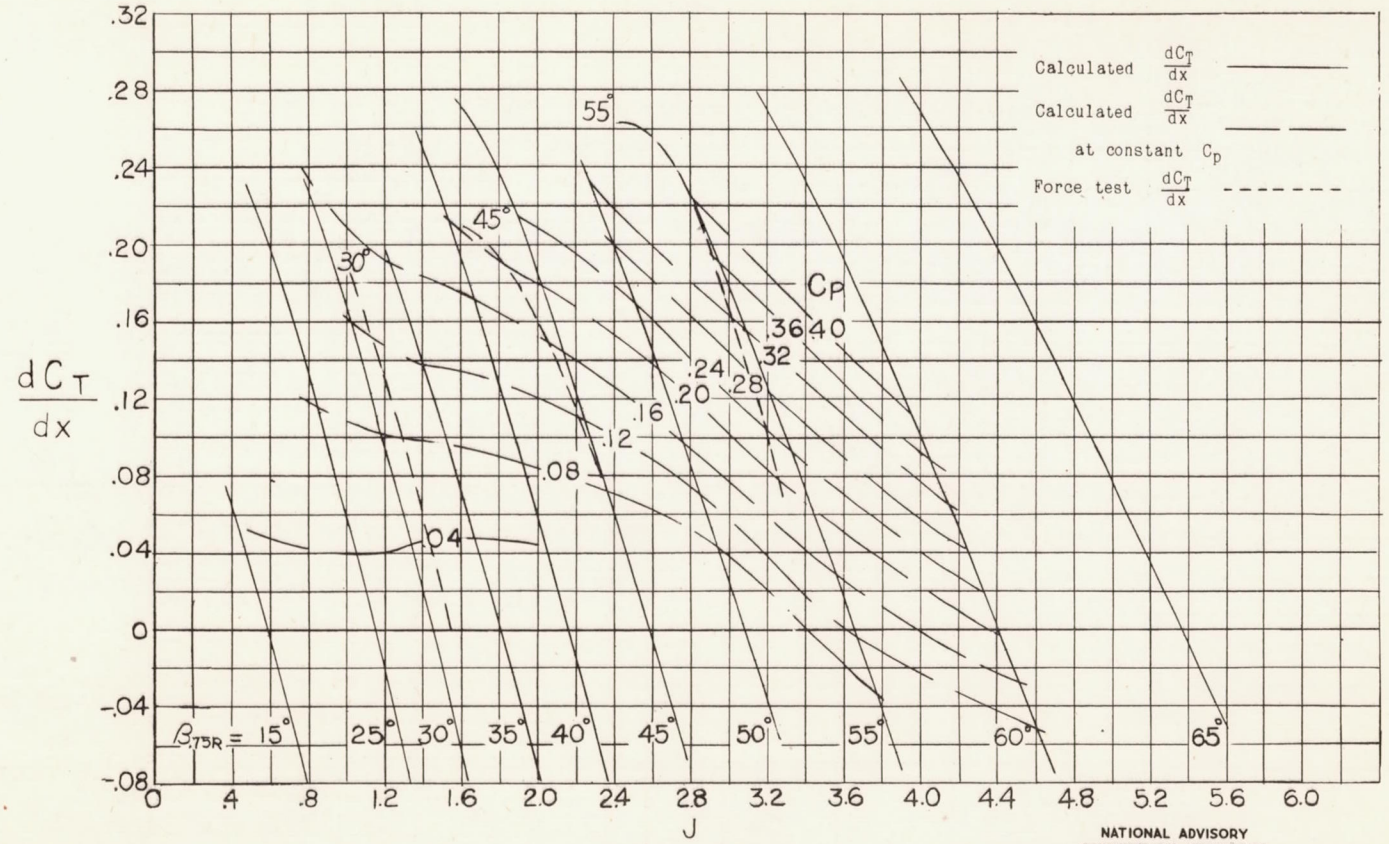
(e) x = 0.8.

Figure 11.- Continued.



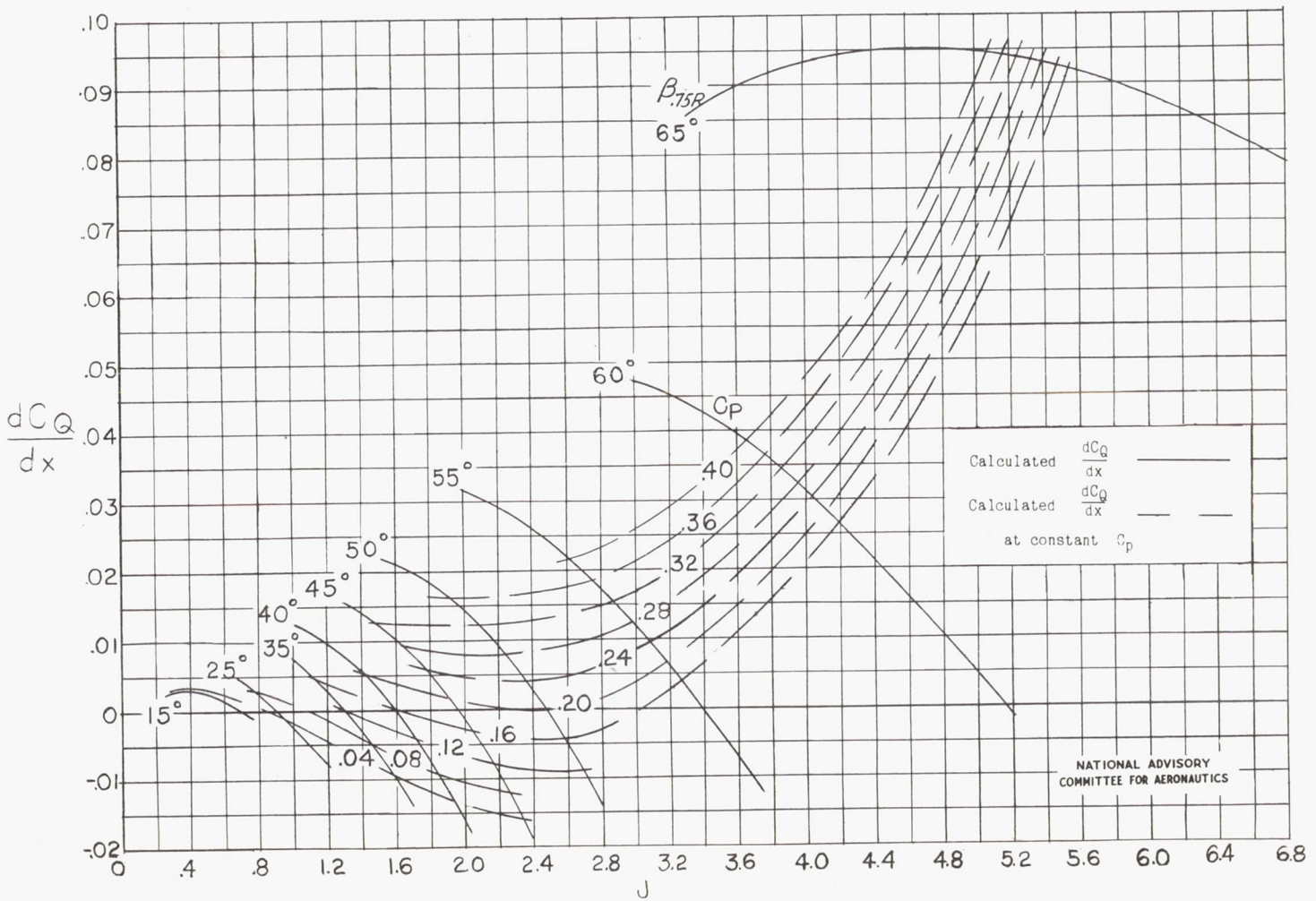
(f) x = 0.9.

Figure 11. - Continued.



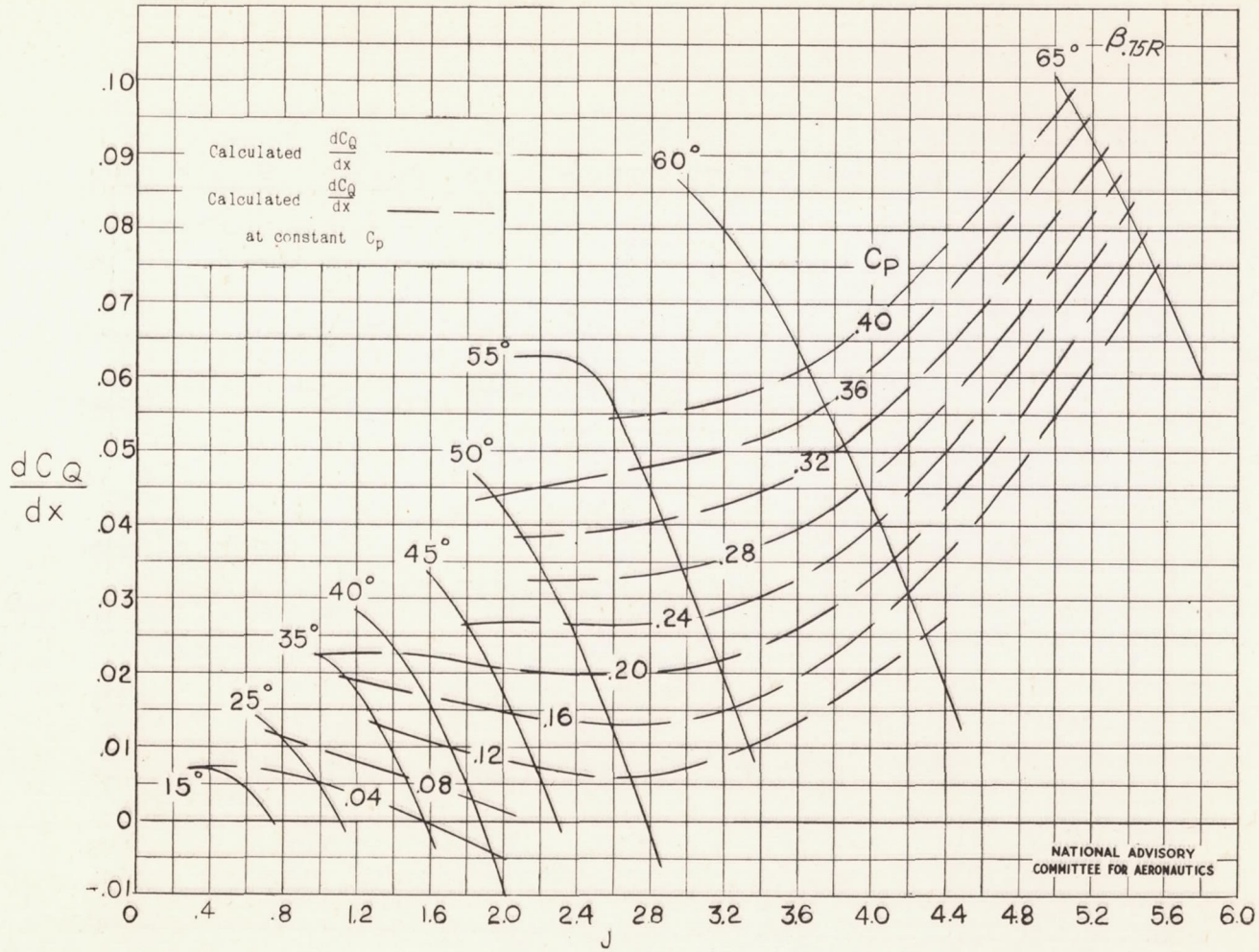
(g) x = 0.95.

Figure 11. - Concluded.



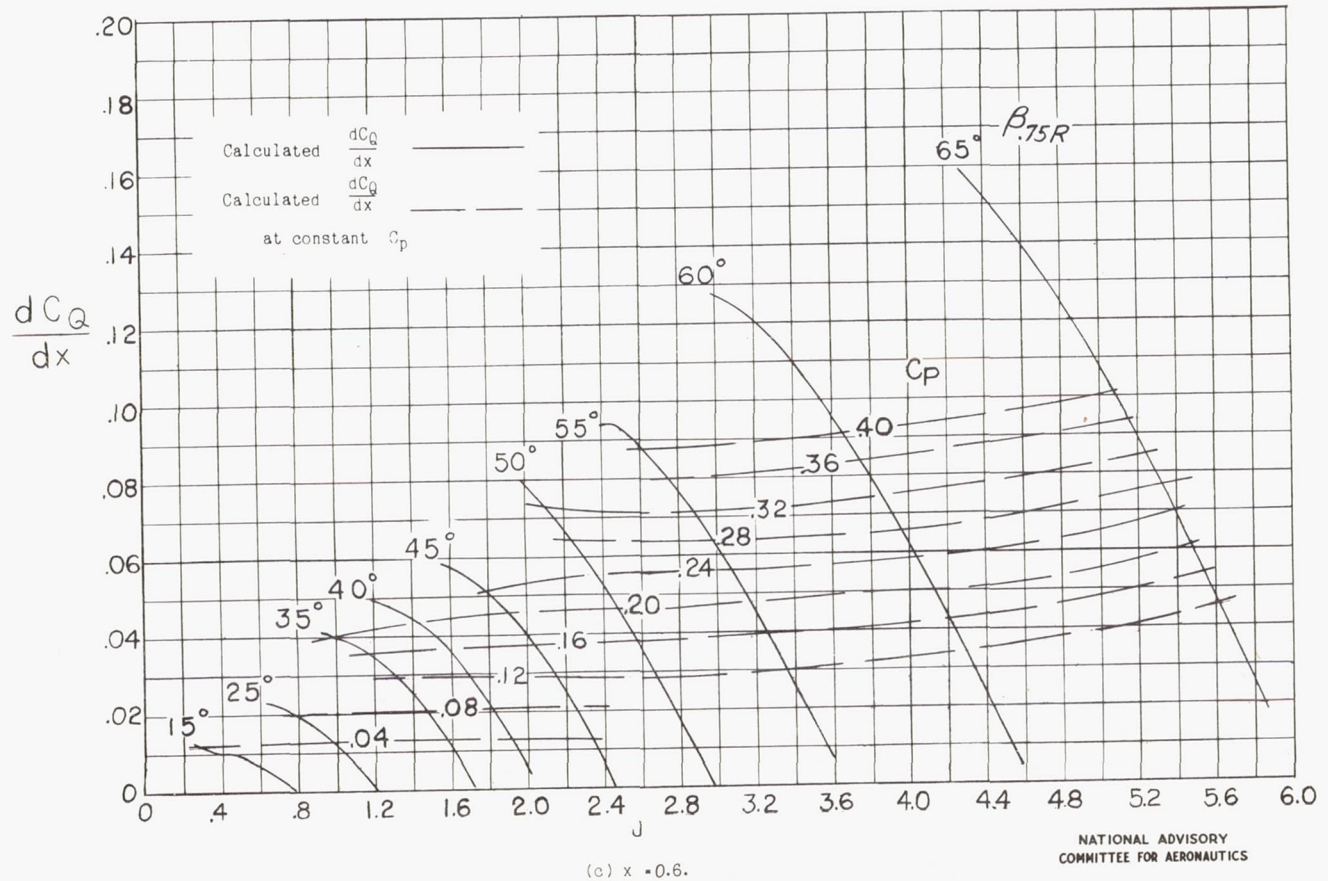
(a) x = 0.3.

Figure 12.- Element torque coefficients. Propeller 55S.



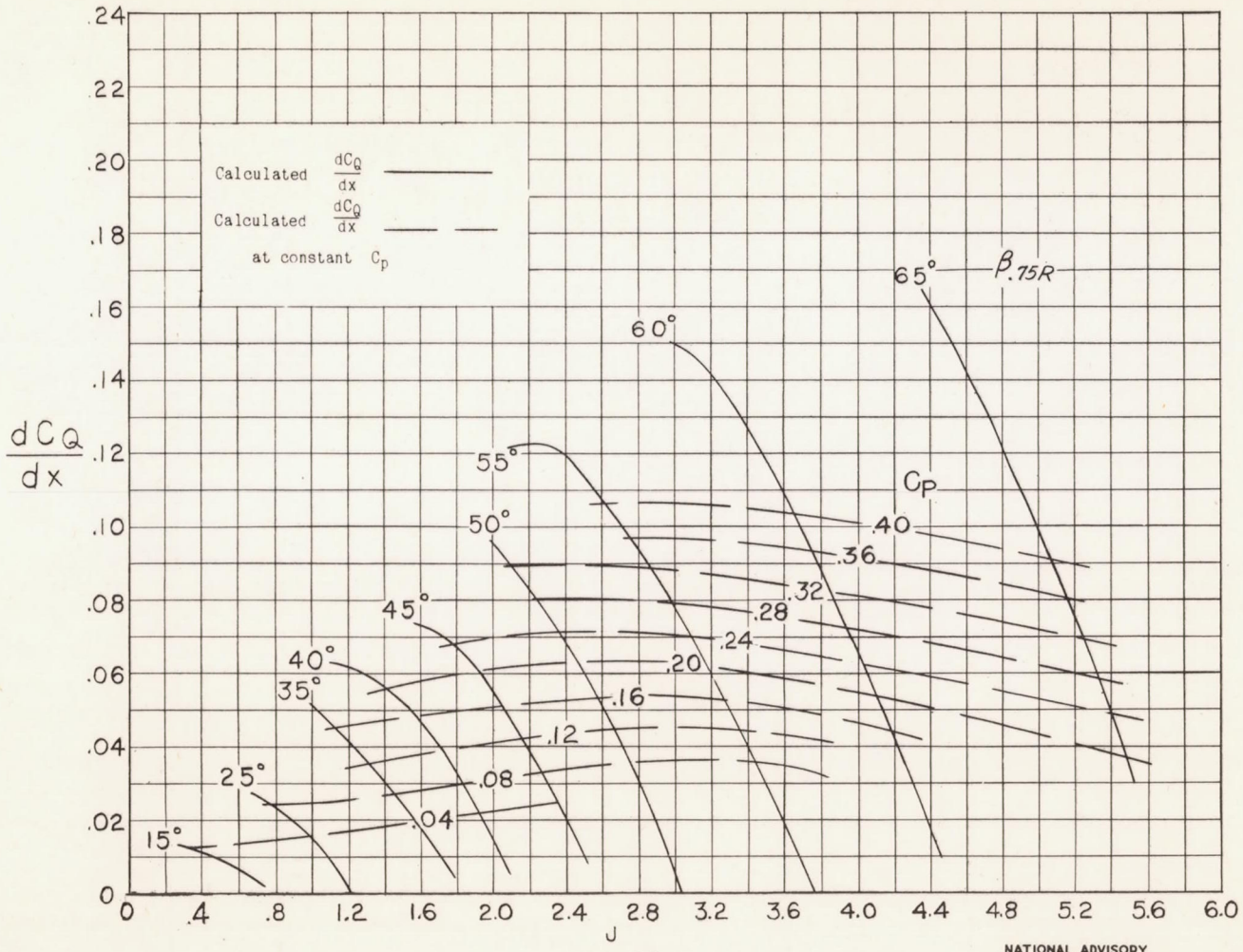
(b) x = 0.45.

Figure 12.- Continued.



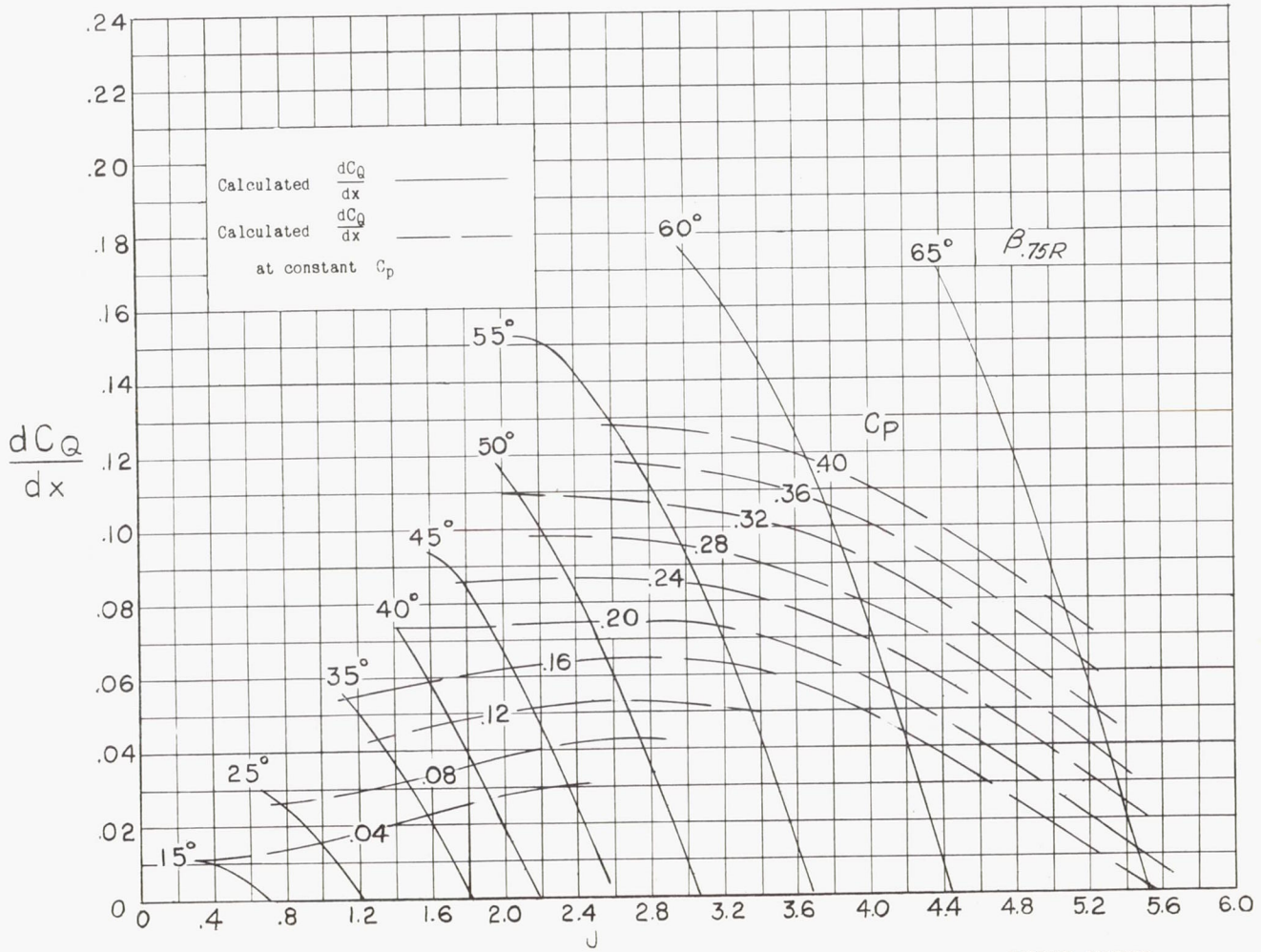
(c) x -0.6.

Figure 12.- Continued.



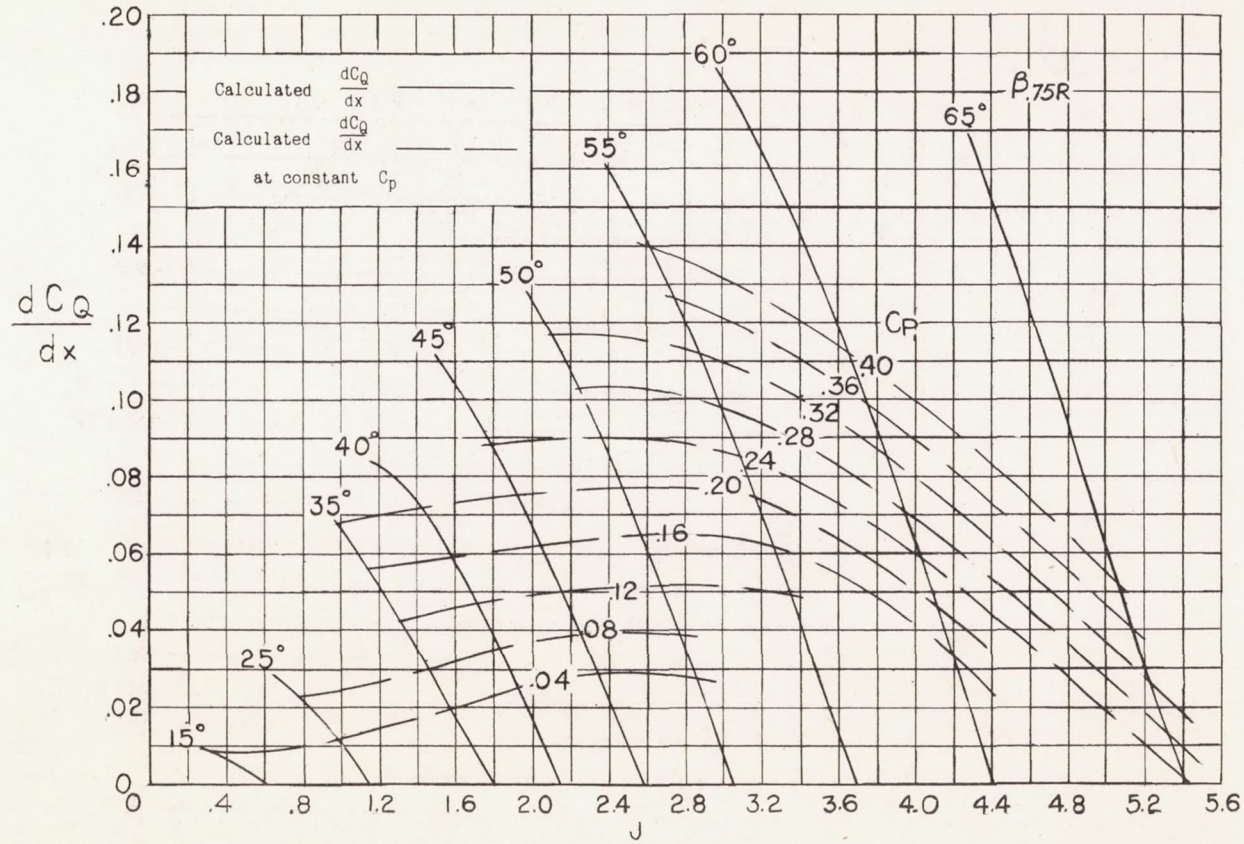
(d) x = 0.7.

Figure 12.- Continued.



(e) x = 0.8.

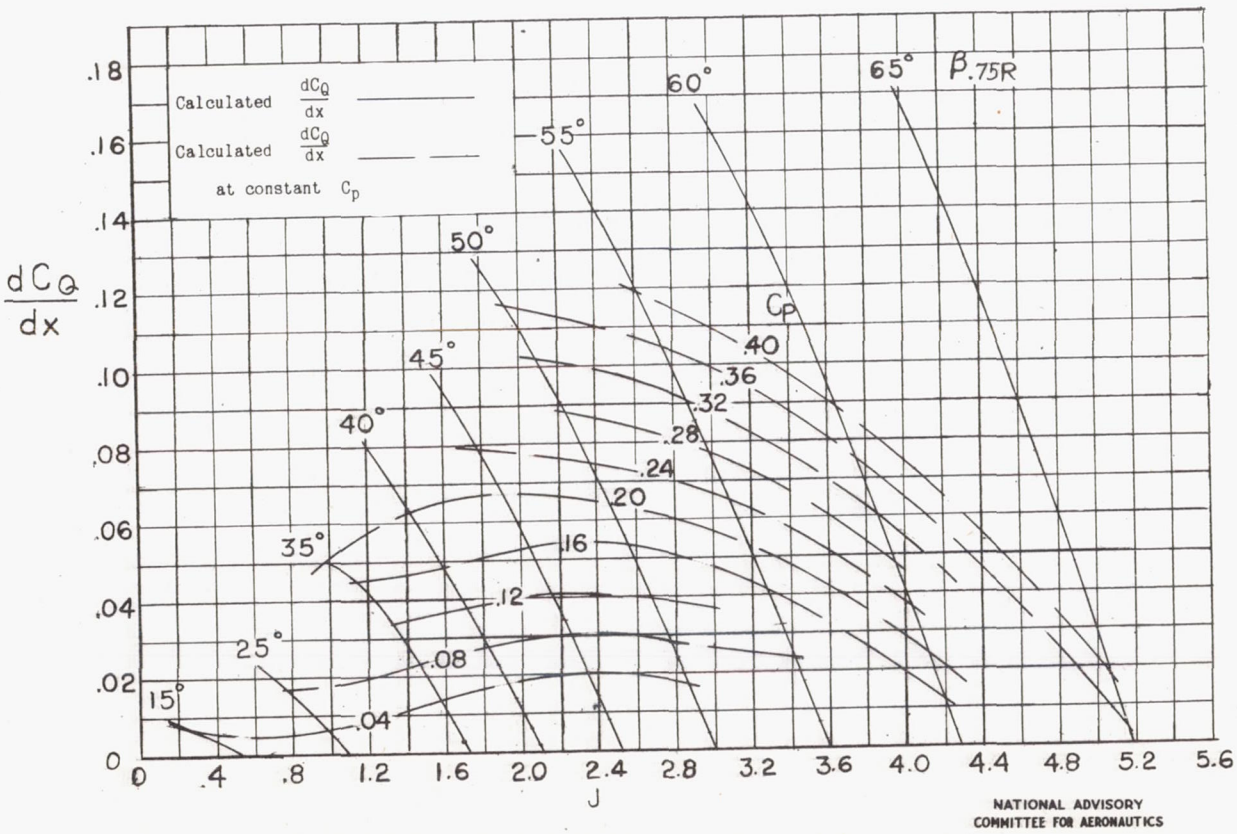
Figure 12.- Continued.



NATIONAL ADVISORY COMMITTEE FOR AERONAUTICS

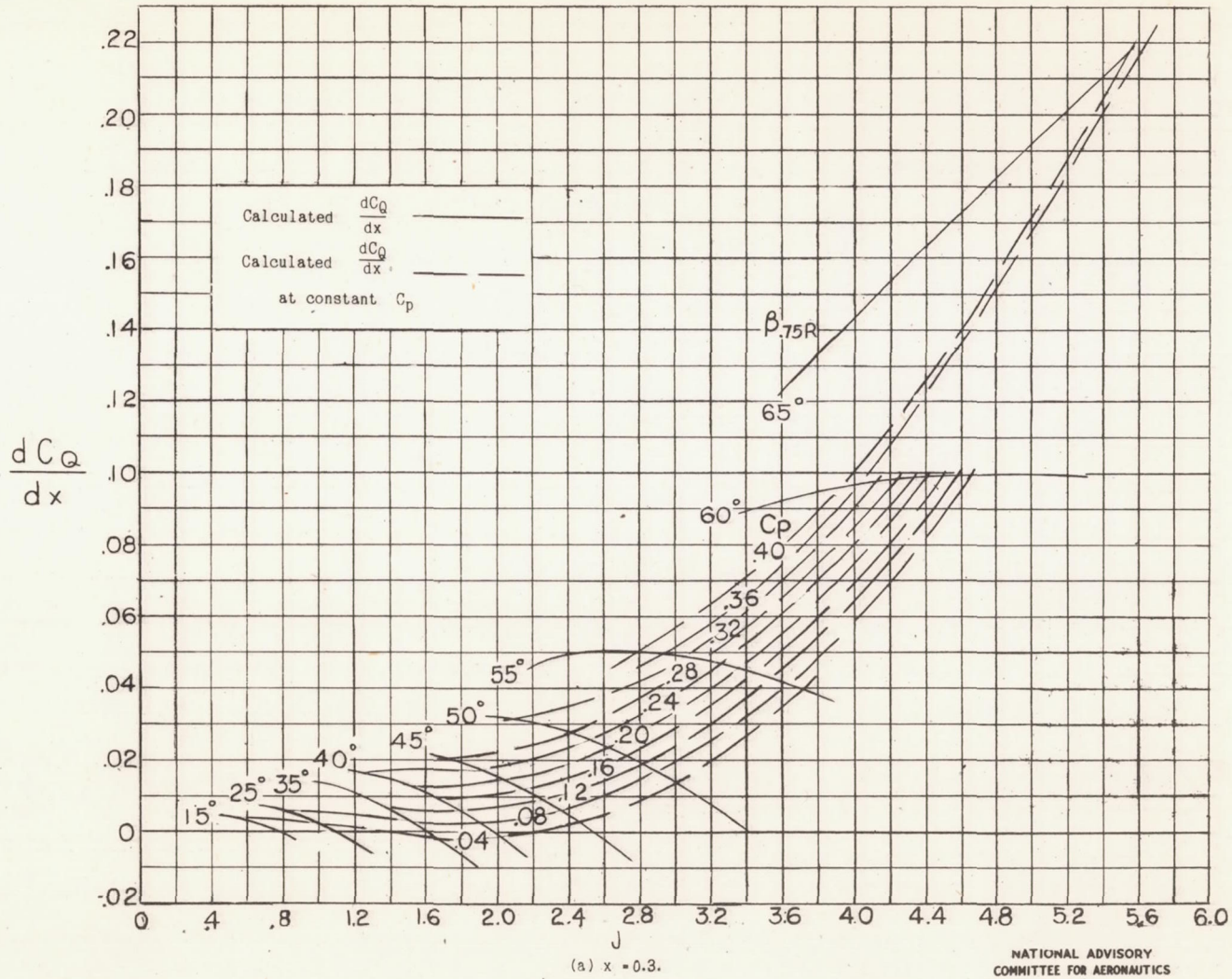
(f) x = 0.9.

Figure 12.- Continued.



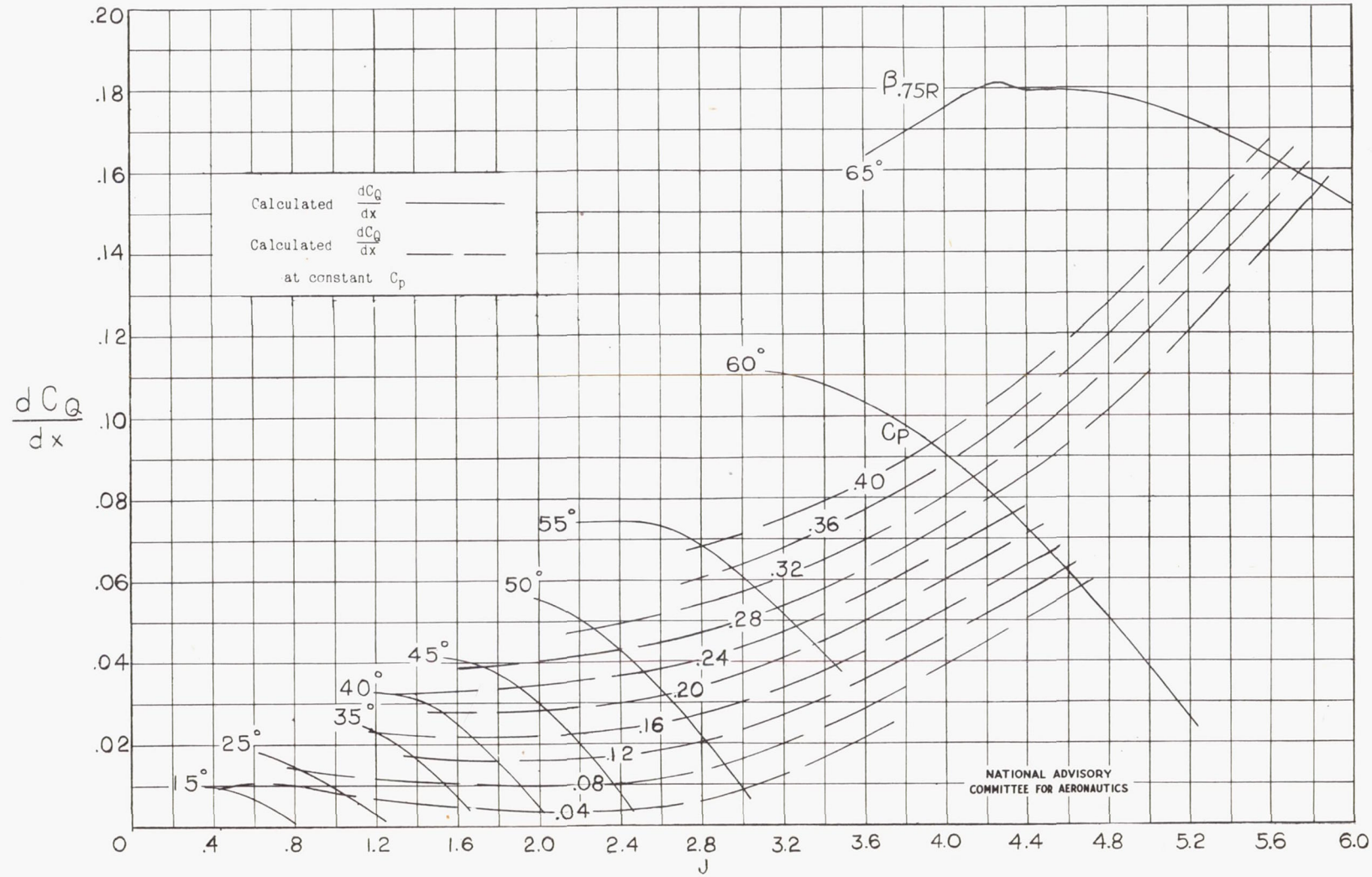
(g) x = 0.95.

Figure 12.- Concluded.



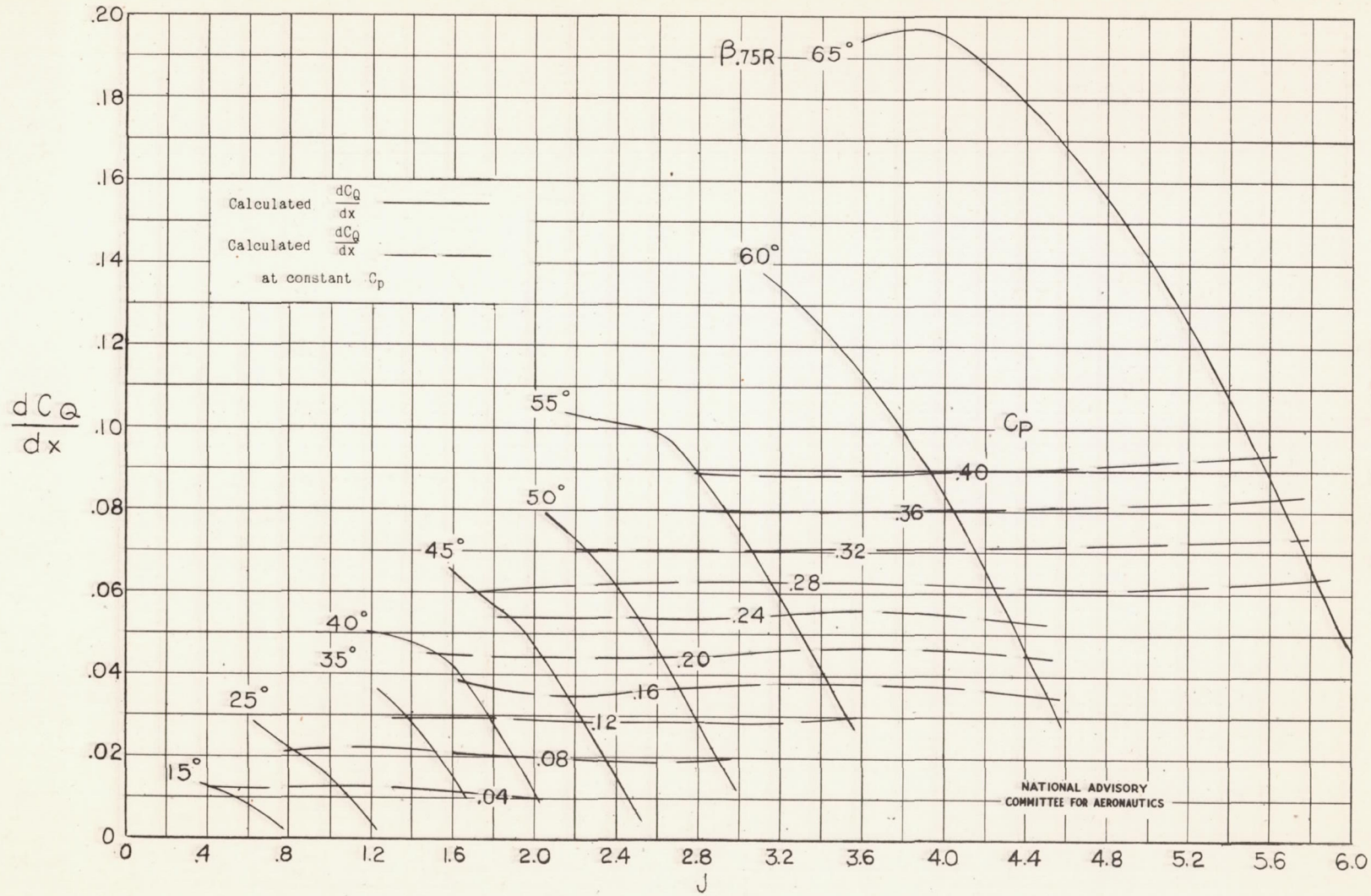
(a) x = 0.3.

Figure 13.- Element torque coefficients. Propeller 45S.



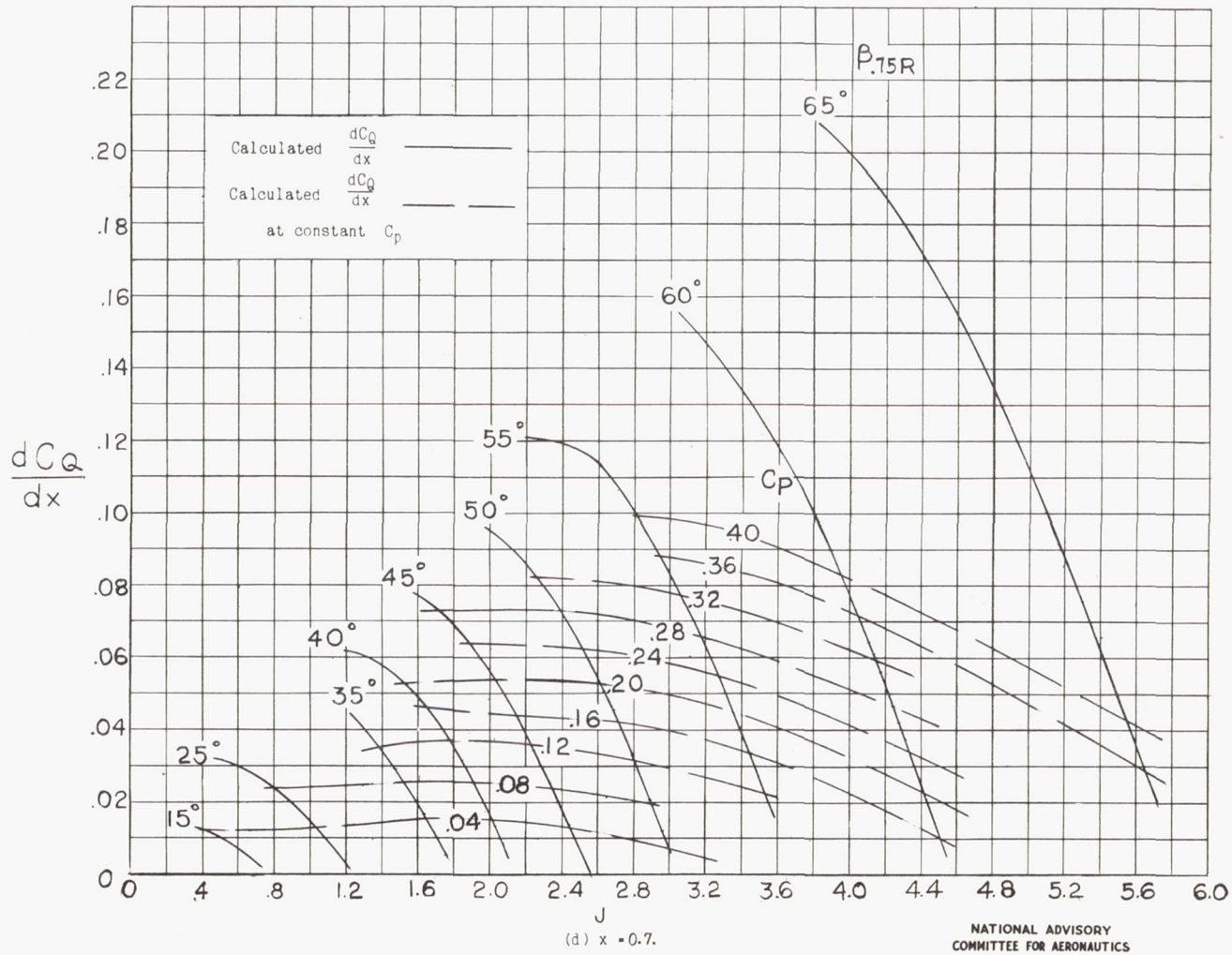
(b) x = 0.45.

Figure 13.- Continued.



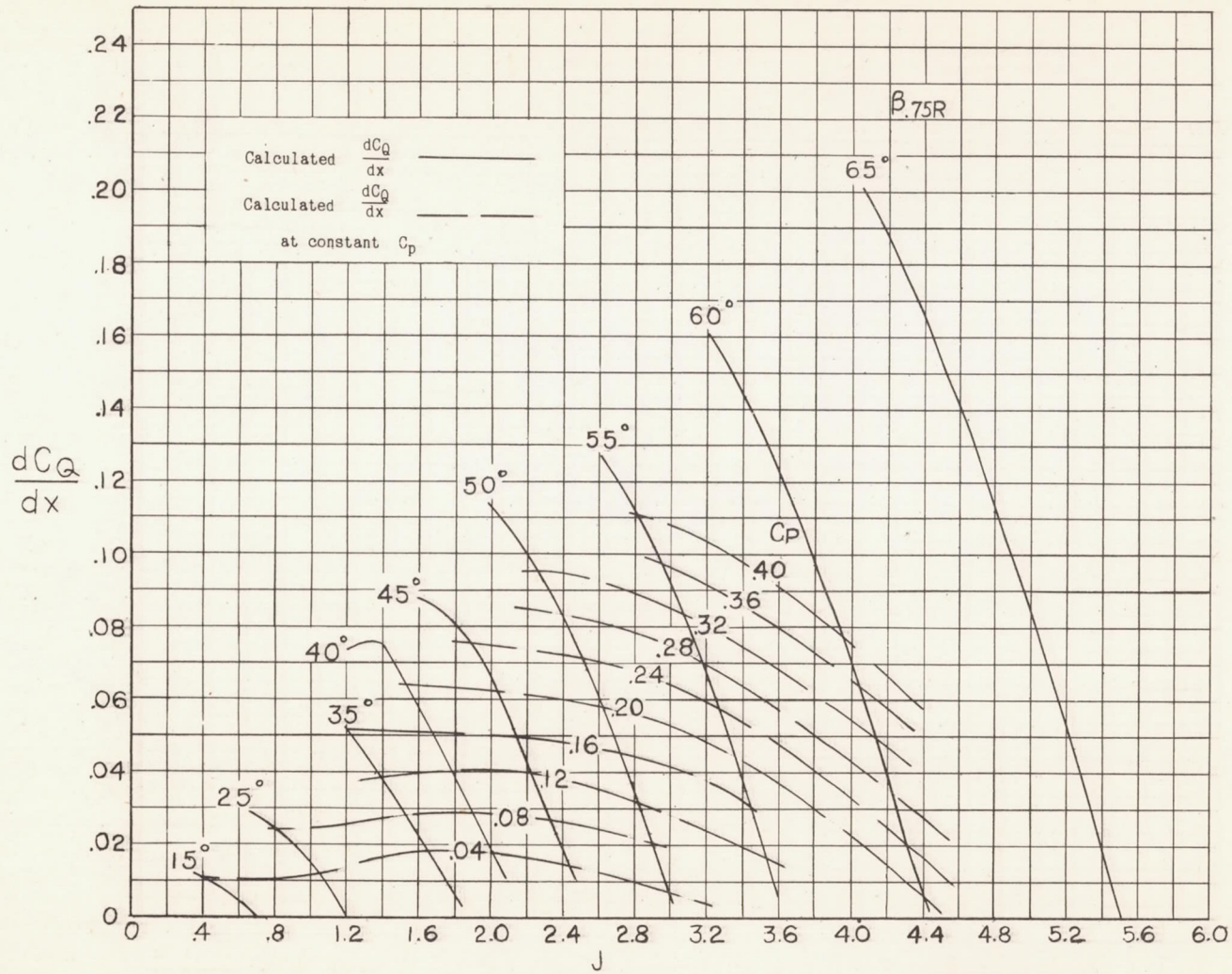
(c) x = 0.6.

Figure 13.- Continued.



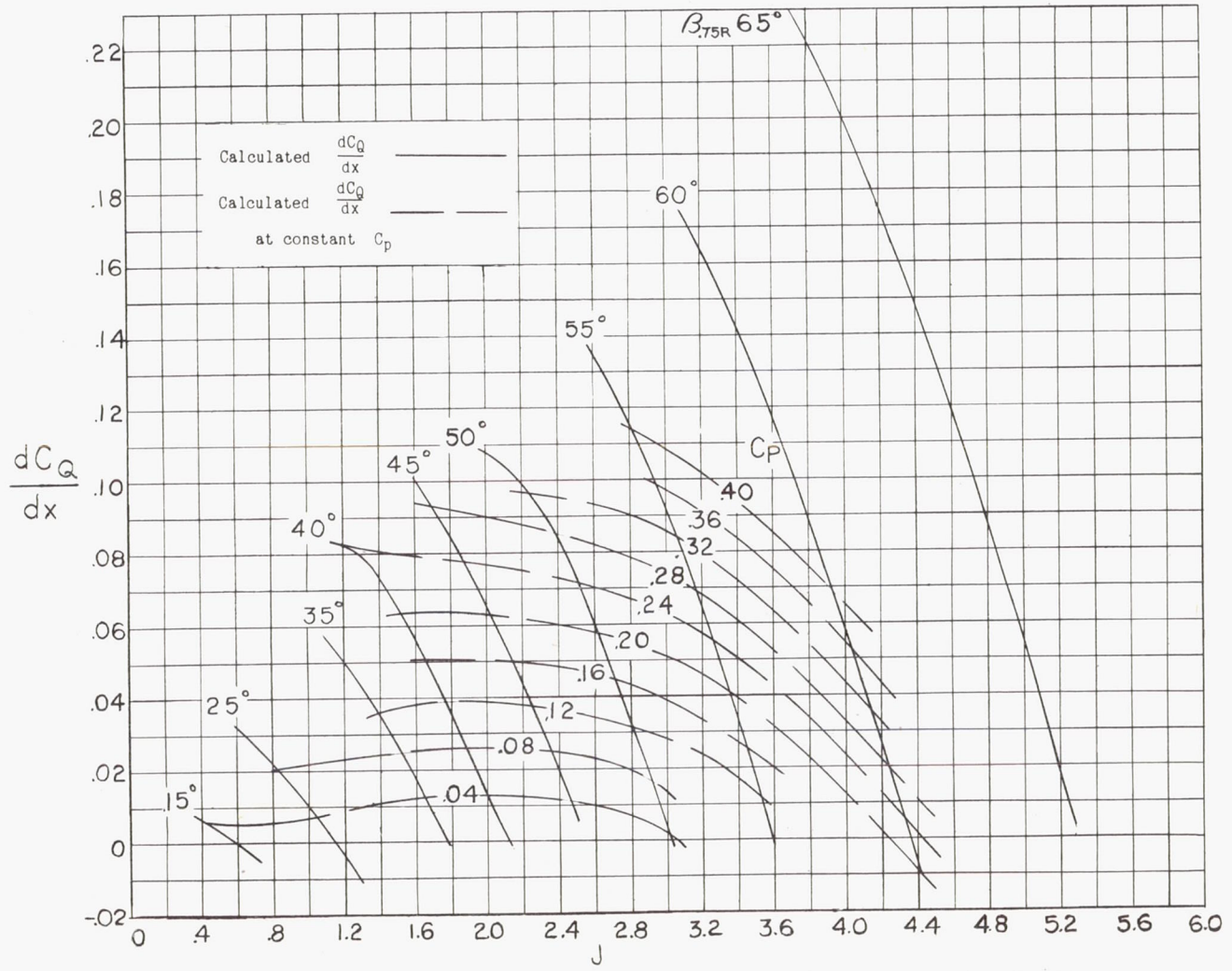
(d) x = 0.7.

Figure 13.- Continued.



(e) x = 0.8.

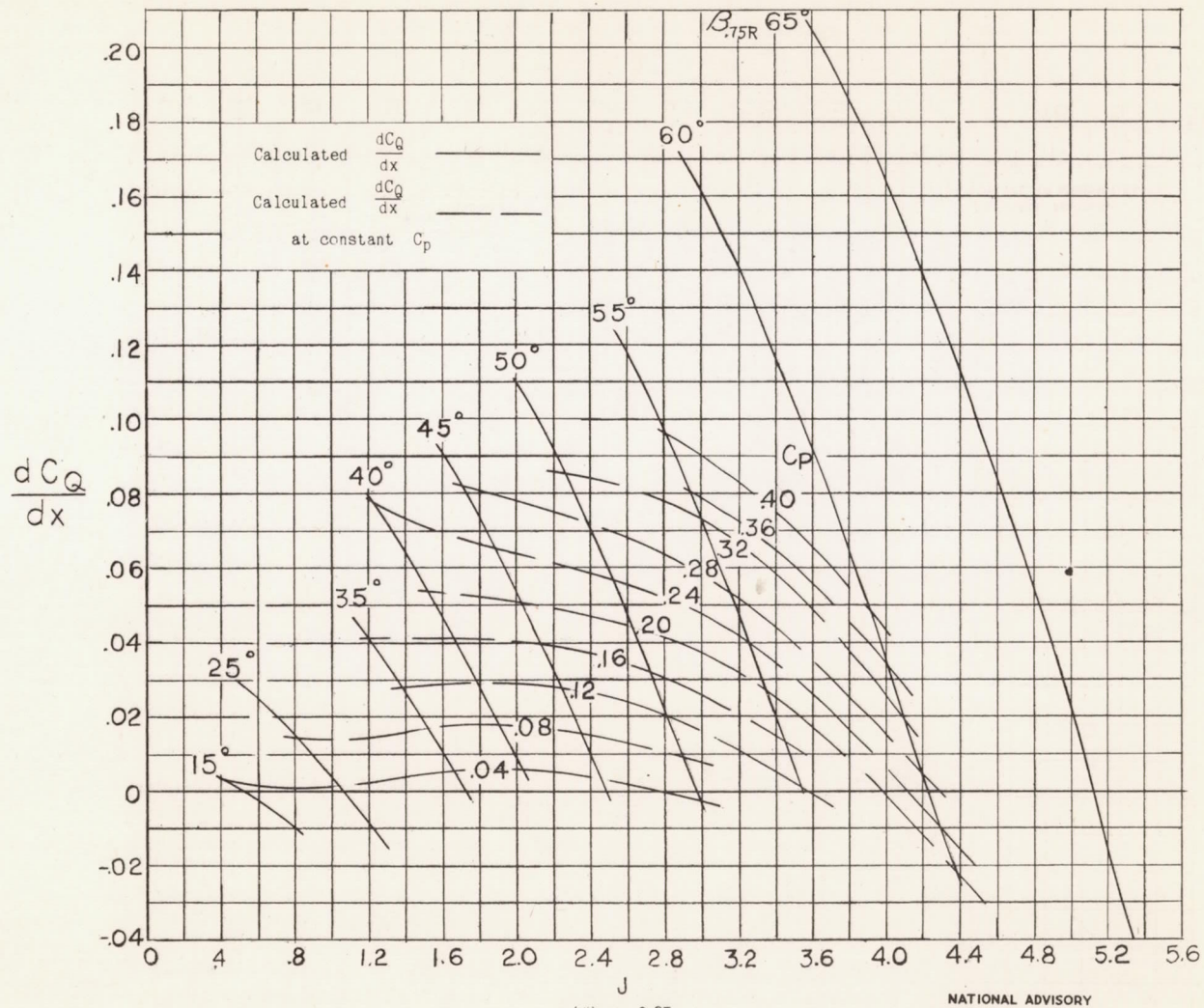
Figure 13.- Continued.



(f) x = 0.9.

Figure 13.- Continued.

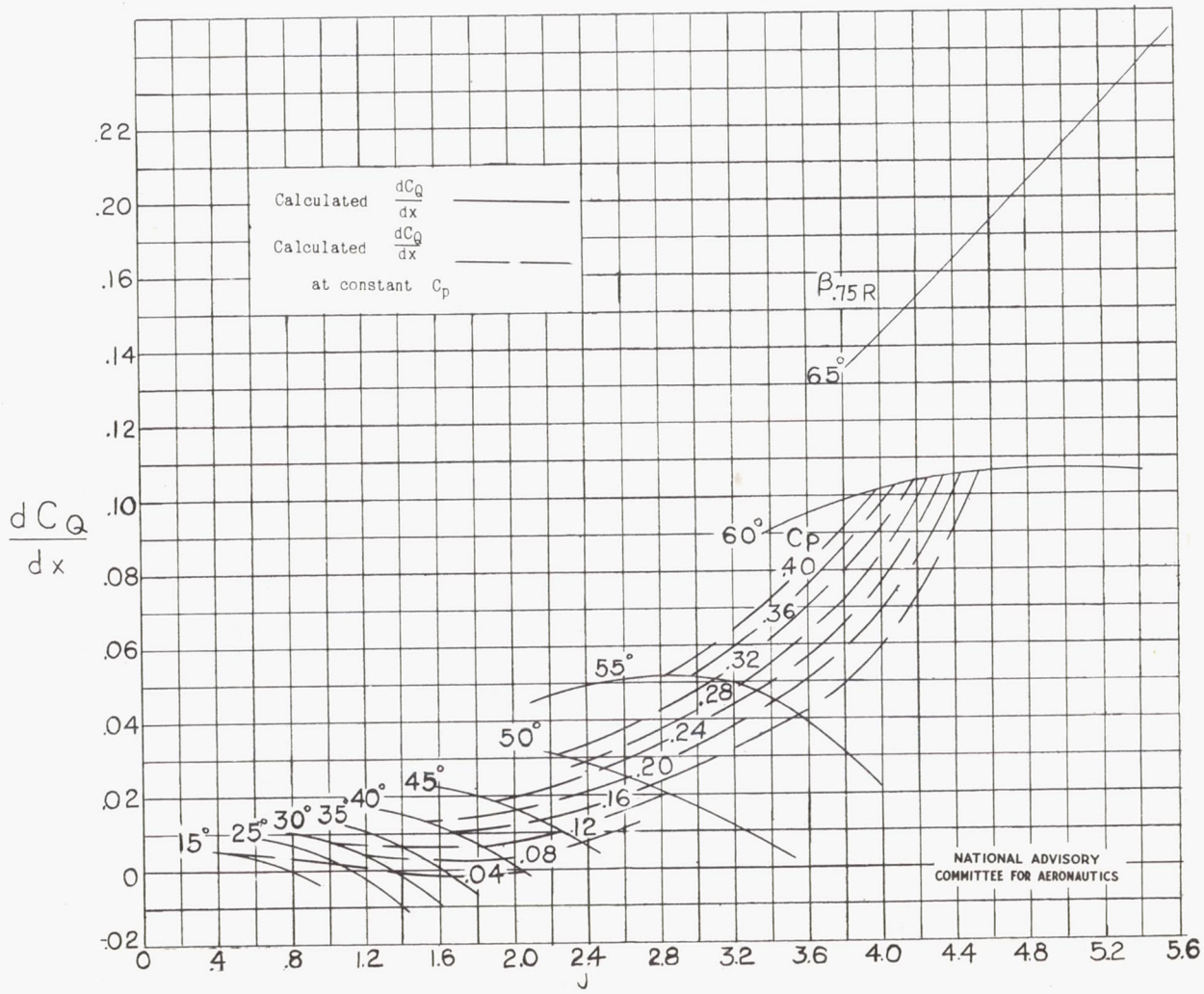
NATIONAL ADVISORY
COMMITTEE FOR AERONAUTICS



(g) x = 0.95.

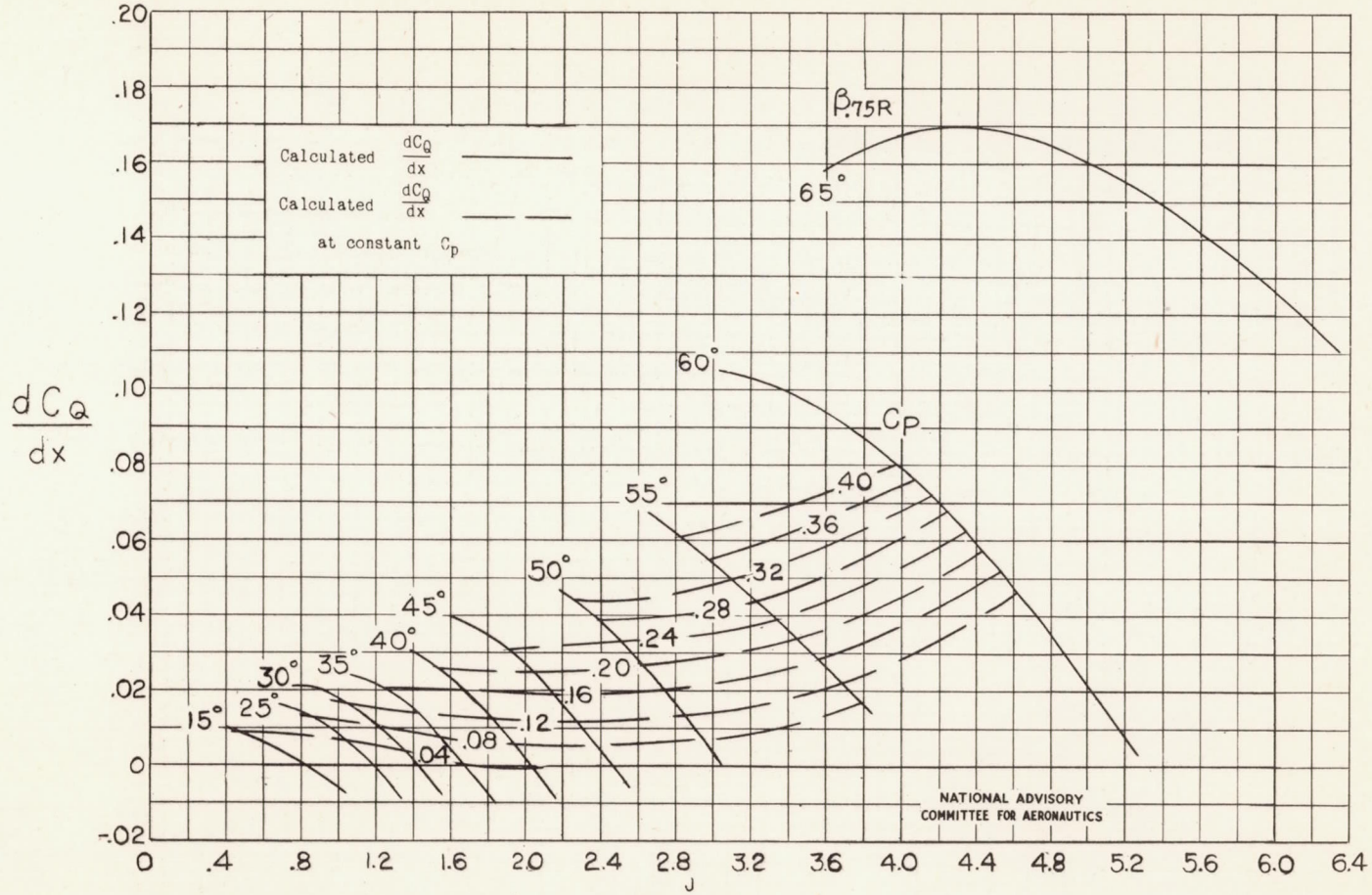
NATIONAL ADVISORY COMMITTEE FOR AERONAUTICS

Figure 13.- Concluded.



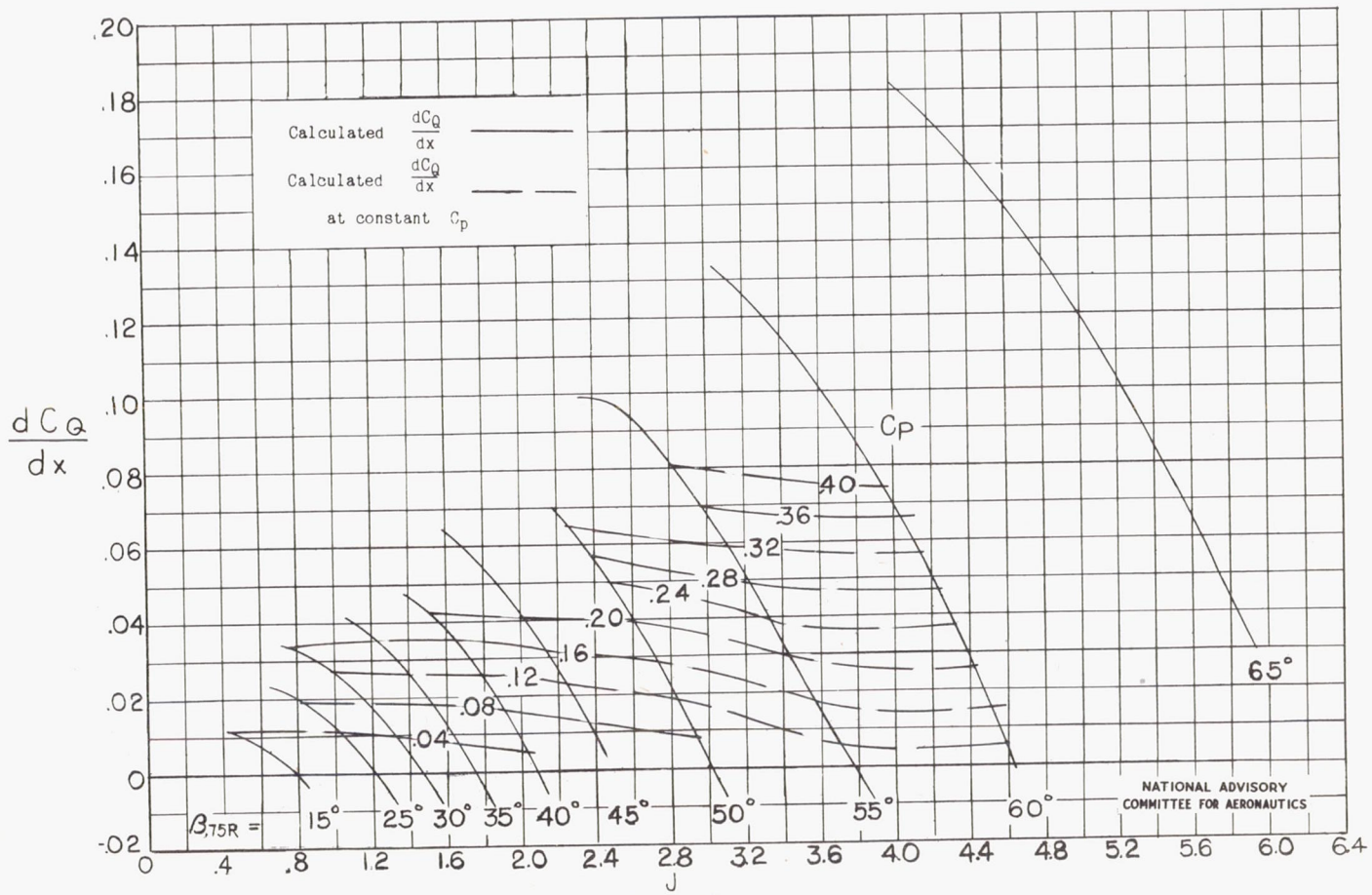
(a) x = 0.3.

Figure 14.- Element torque coefficient. Propeller 30S.



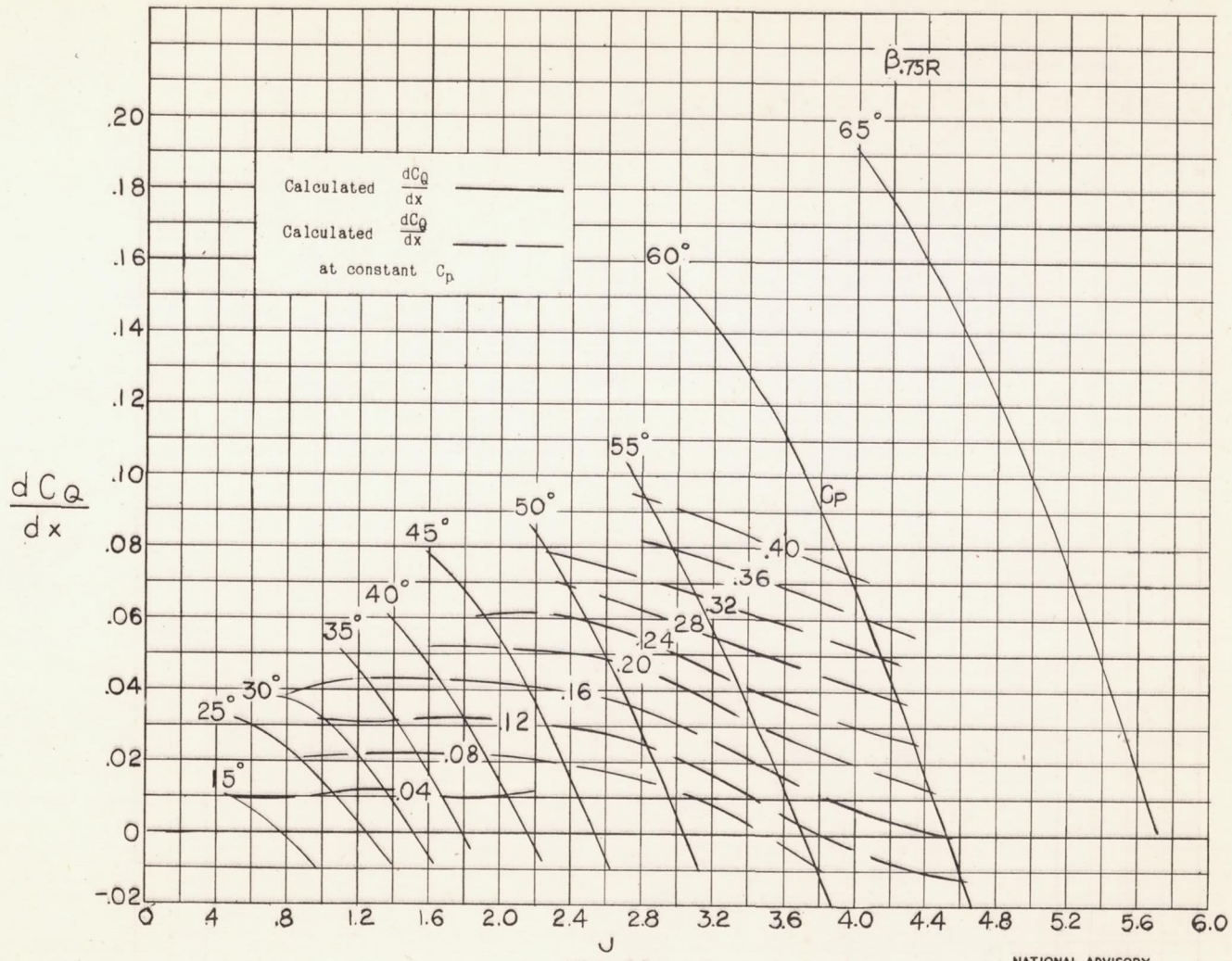
(b) x = 0.45.

Figure 14.- Continued.



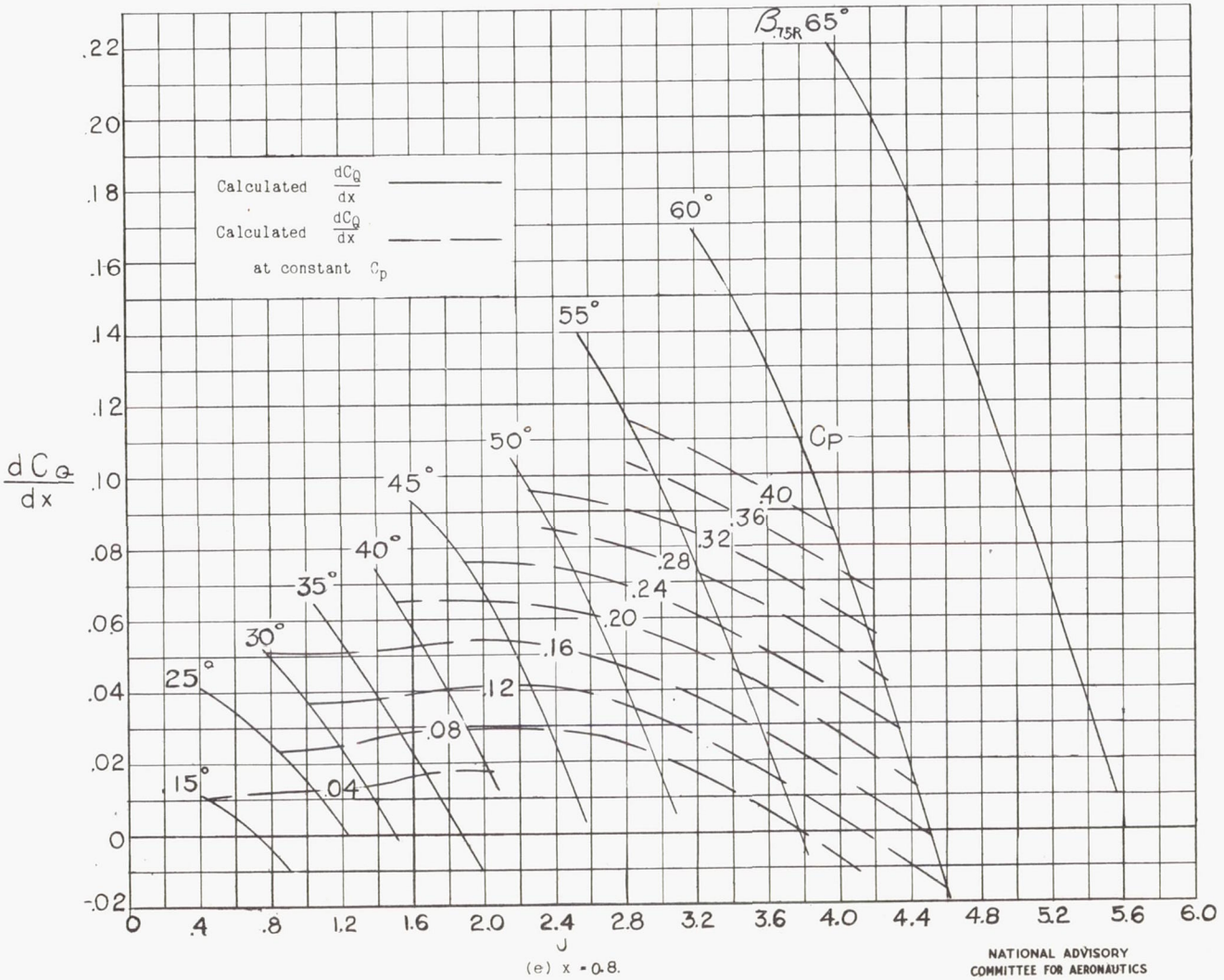
(c) x = 0.6.

Figure 14.- Continued.



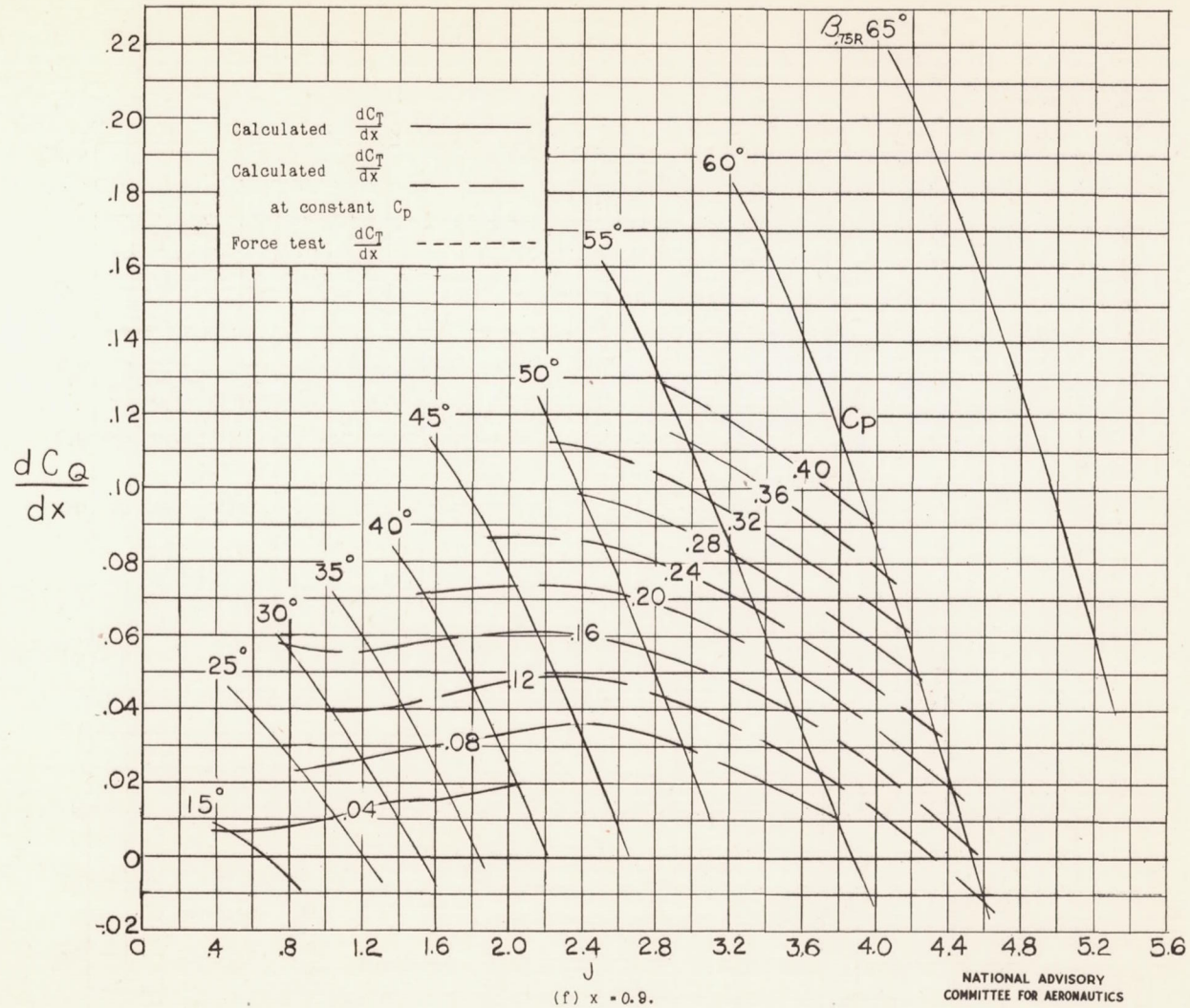
(d) x =0.7.

Figure 14.- Continued.



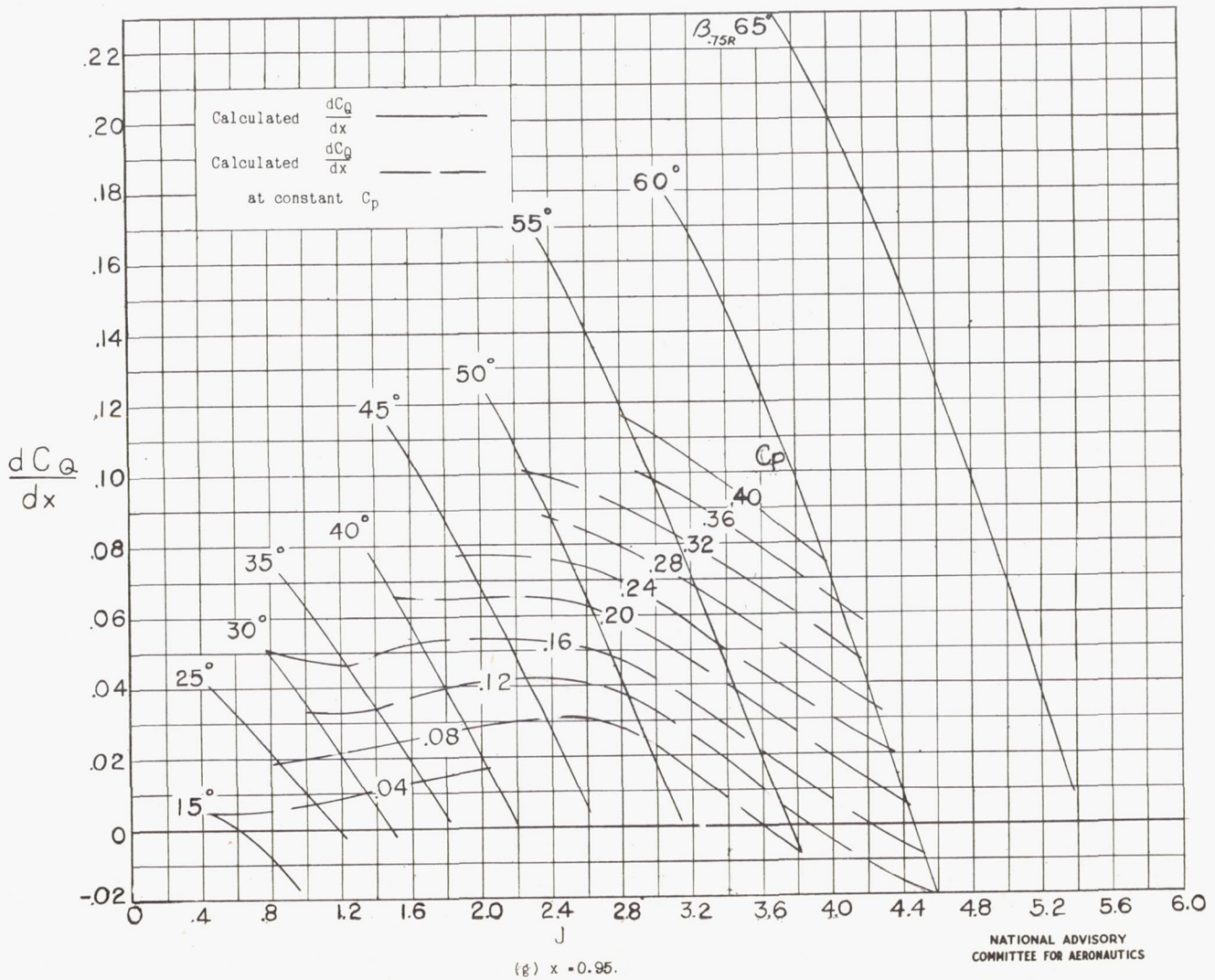
(e) x = 0.8.

Figure 14.- Continued.



(f) x = 0.9.

Figure 14.- Continued.



(g) x = 0.95.

Figure 14.- Concluded.

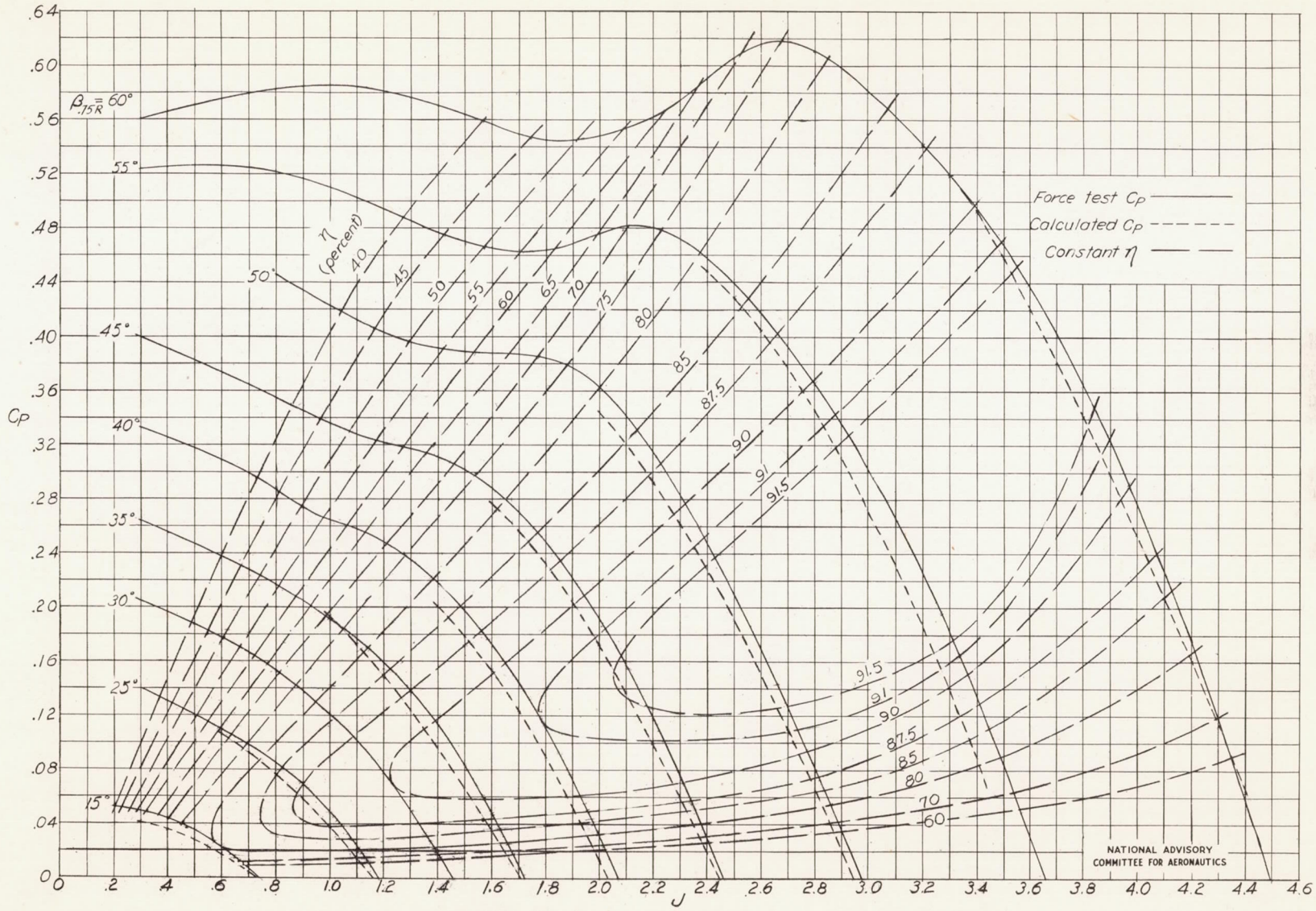


Figure 15.- Propeller operating chart. Propeller 55S.

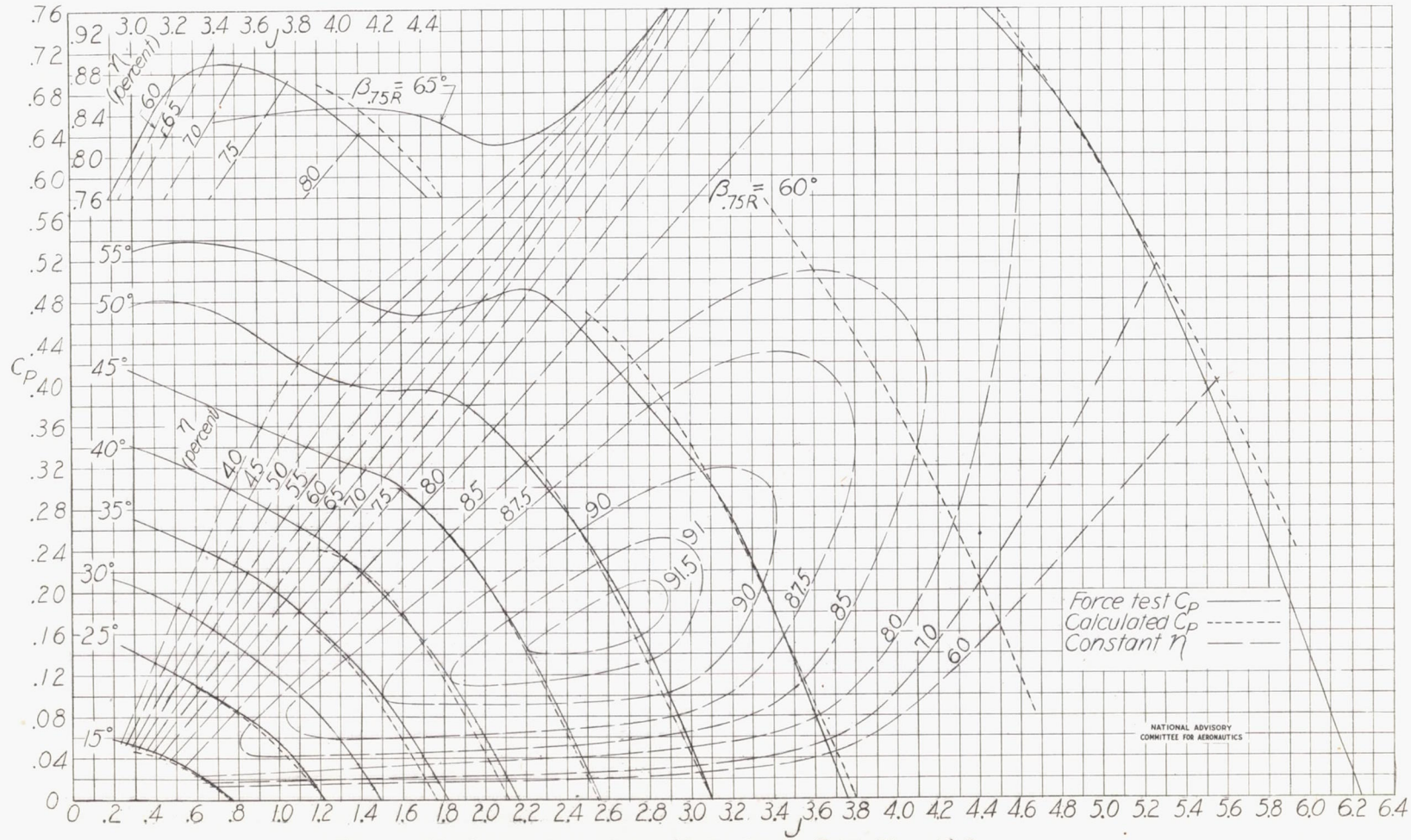


Figure 16.- Propeller operating chart. Propeller 45 S.

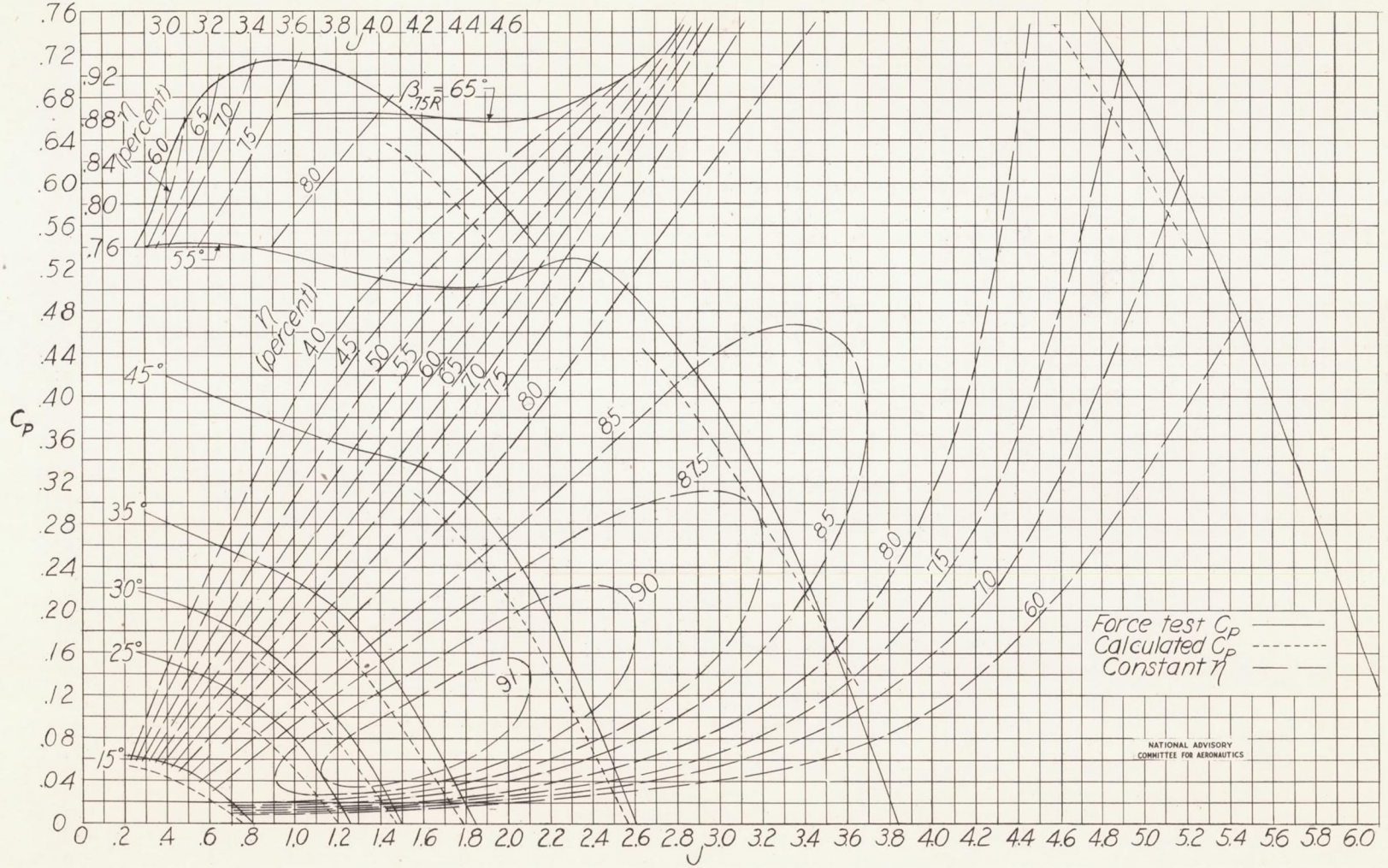


Figure 17.- Propeller operating chart. Propeller 30 S.

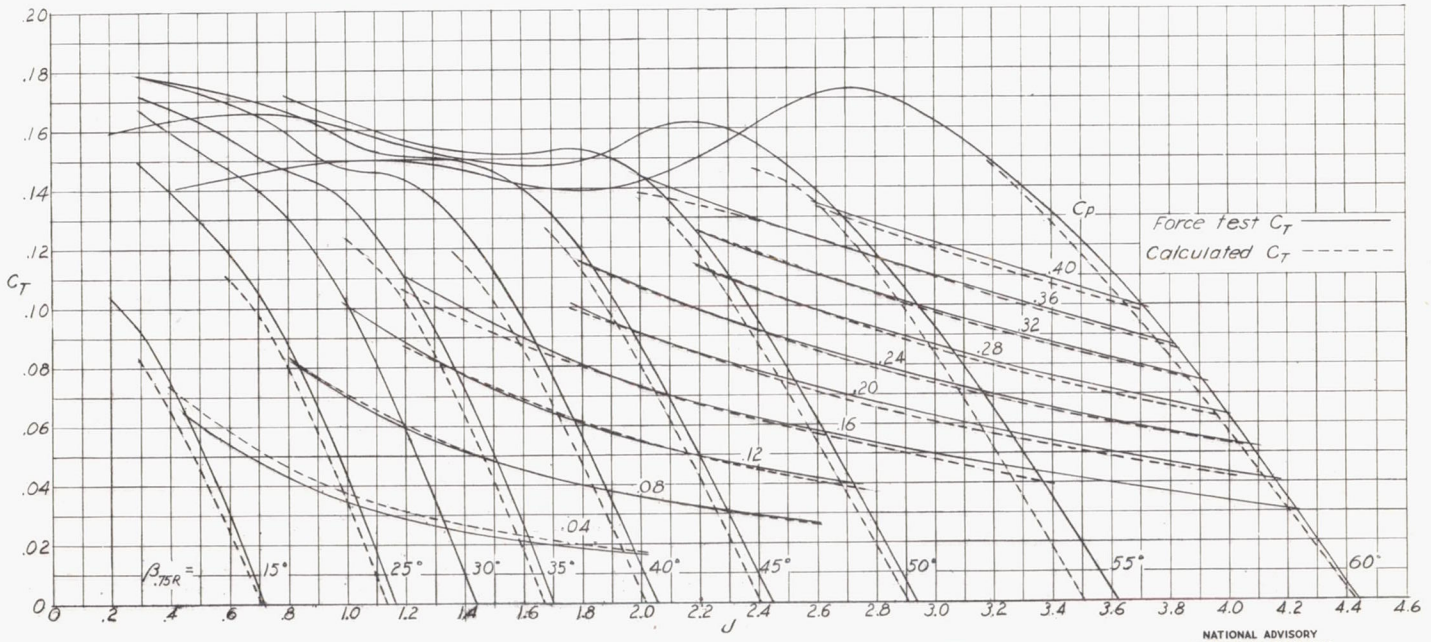


Figure 18.- Thrust coefficient curves. Propeller 5S.

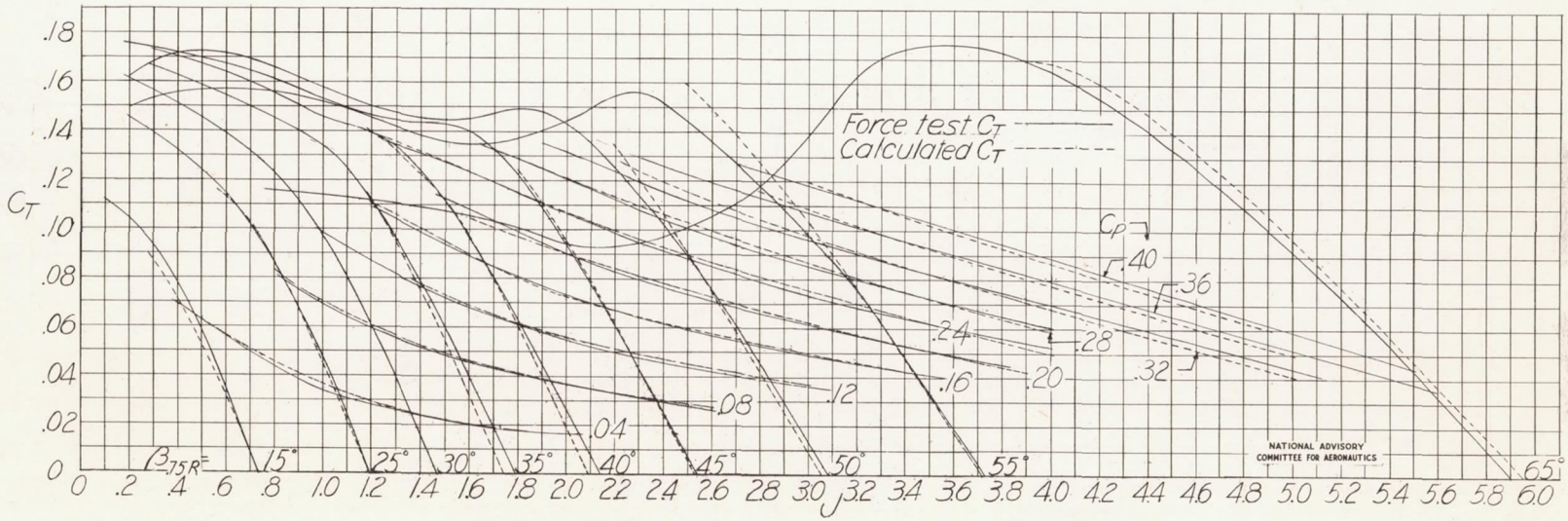


Figure 19.- Thrust-coefficient curves. Propeller 45S.

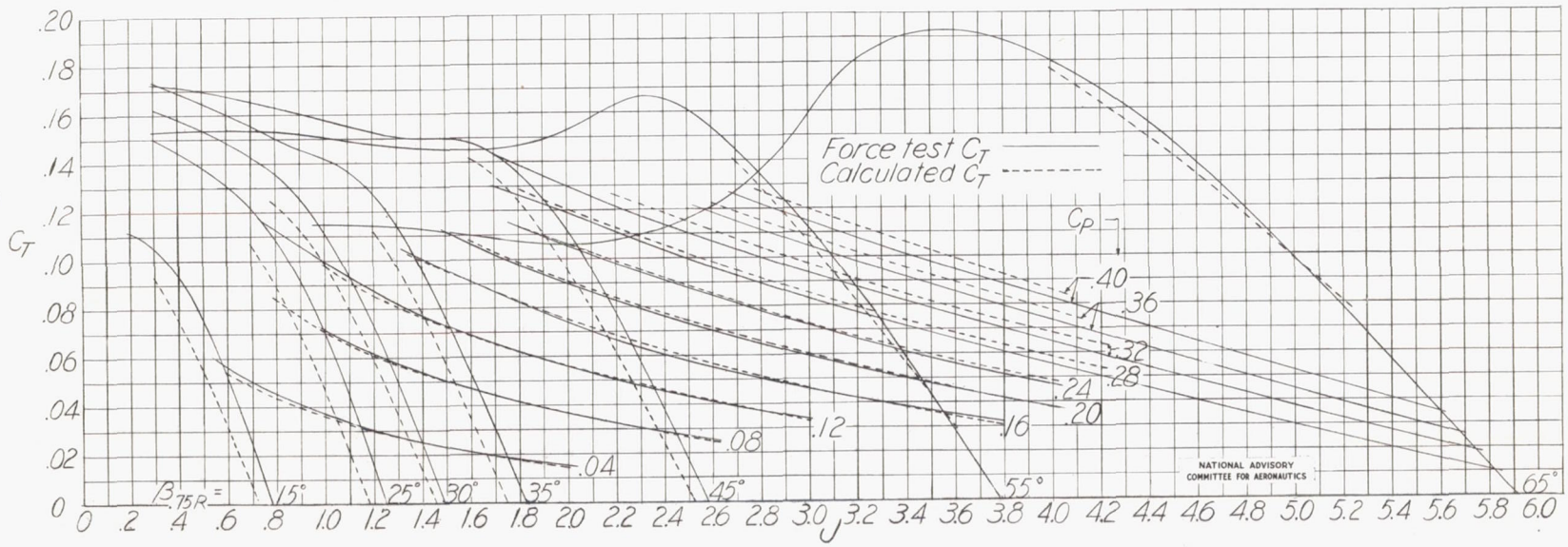


Figure 20.- Thrust- coefficient curves. Propeller 30S.

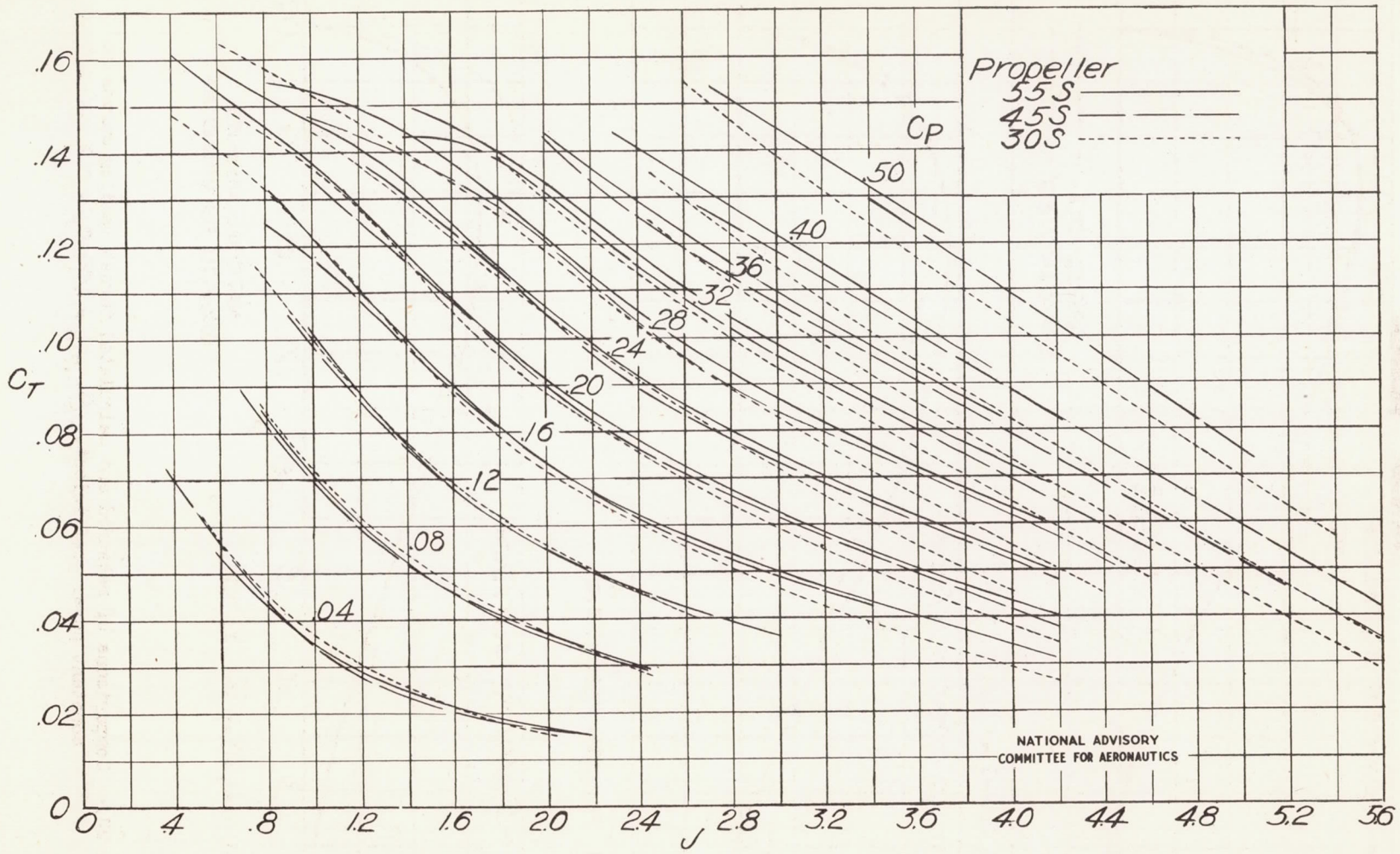
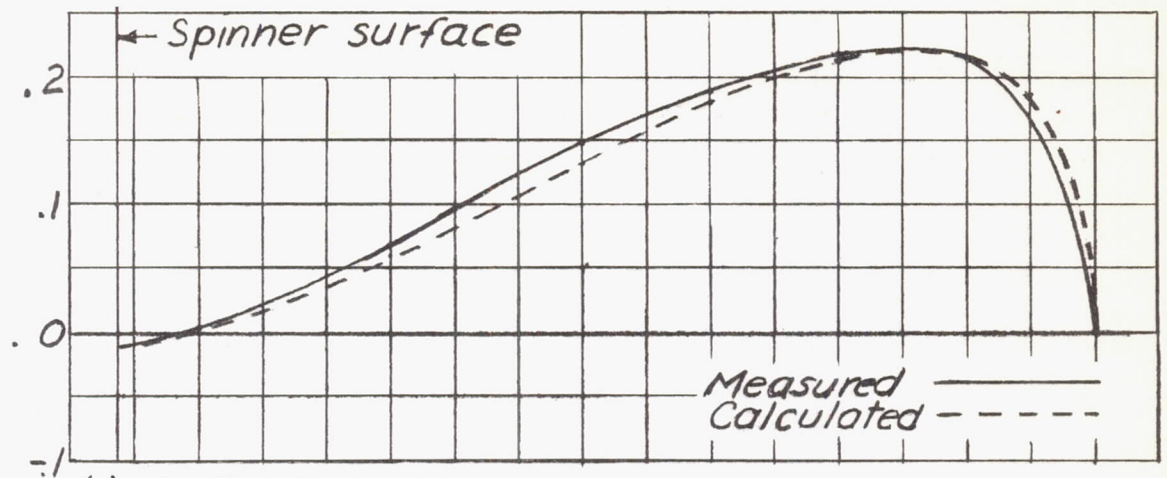
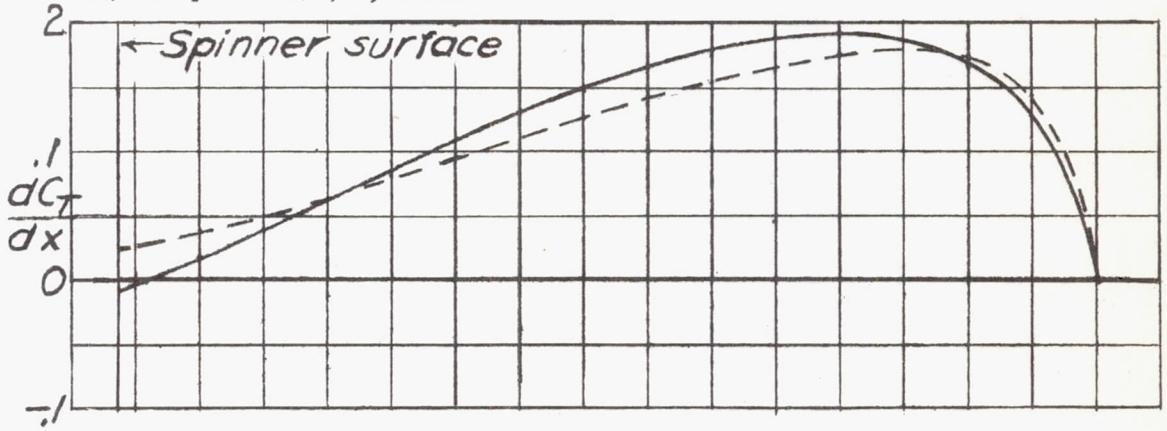


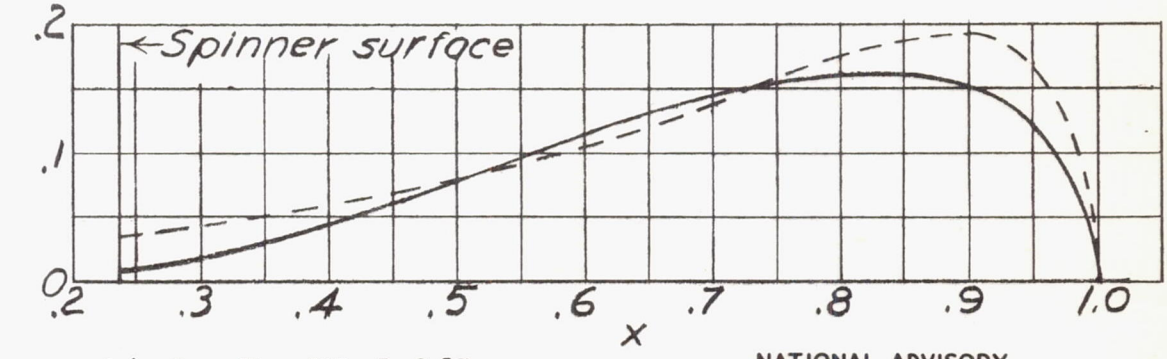
Figure 21.- Comparison of C_T at constant values of C_p. Propellers 55S, 45S, and 30S.



(a) Propeller 55S; J, 1.97.



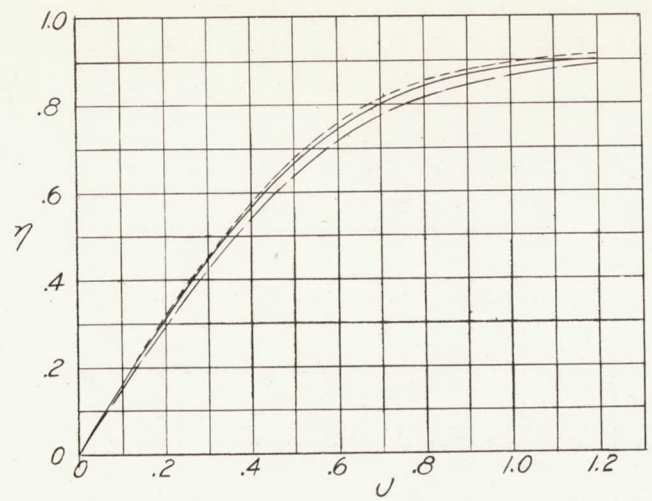
(b) Propeller 45S; J, 2.03.



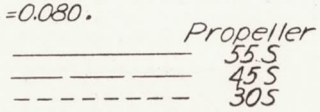
(c) Propeller 30S; J, 2.17.

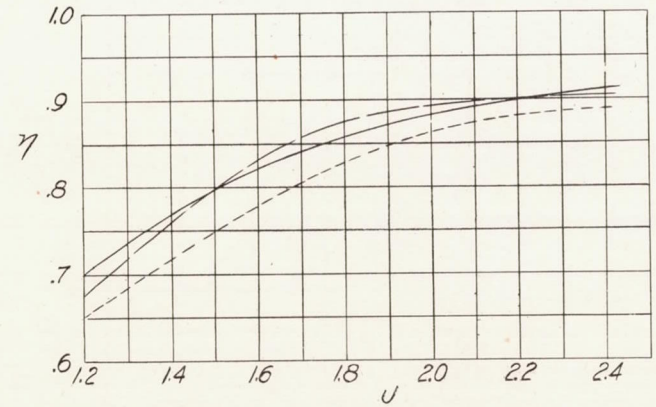
NATIONAL ADVISORY
COMMITTEE FOR AERONAUTICS

Figure 22.- Comparisons of measured and calculated thrust loading curves at constant power coefficient. $\beta_{0.75R} = 45^{\circ}$; $C_P = 0.2$.

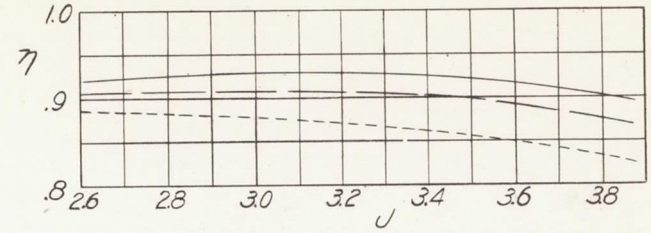


(a) Take-off. $C_p = 0.080$.

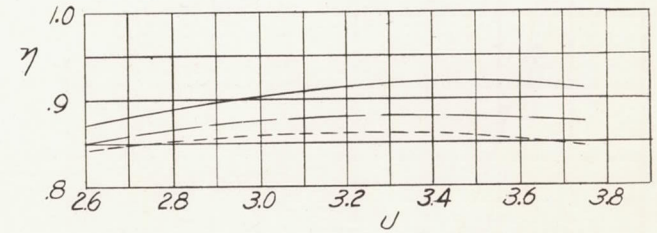




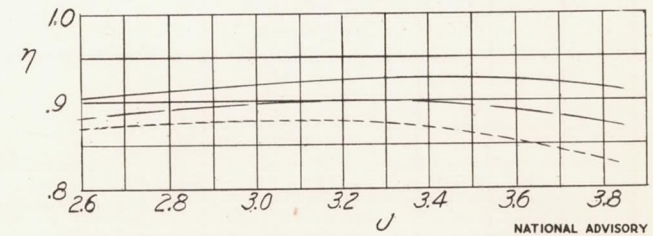
(b) Climb. $C_p = 0.246$.



(c) High speed. $C_p = 0.246$.



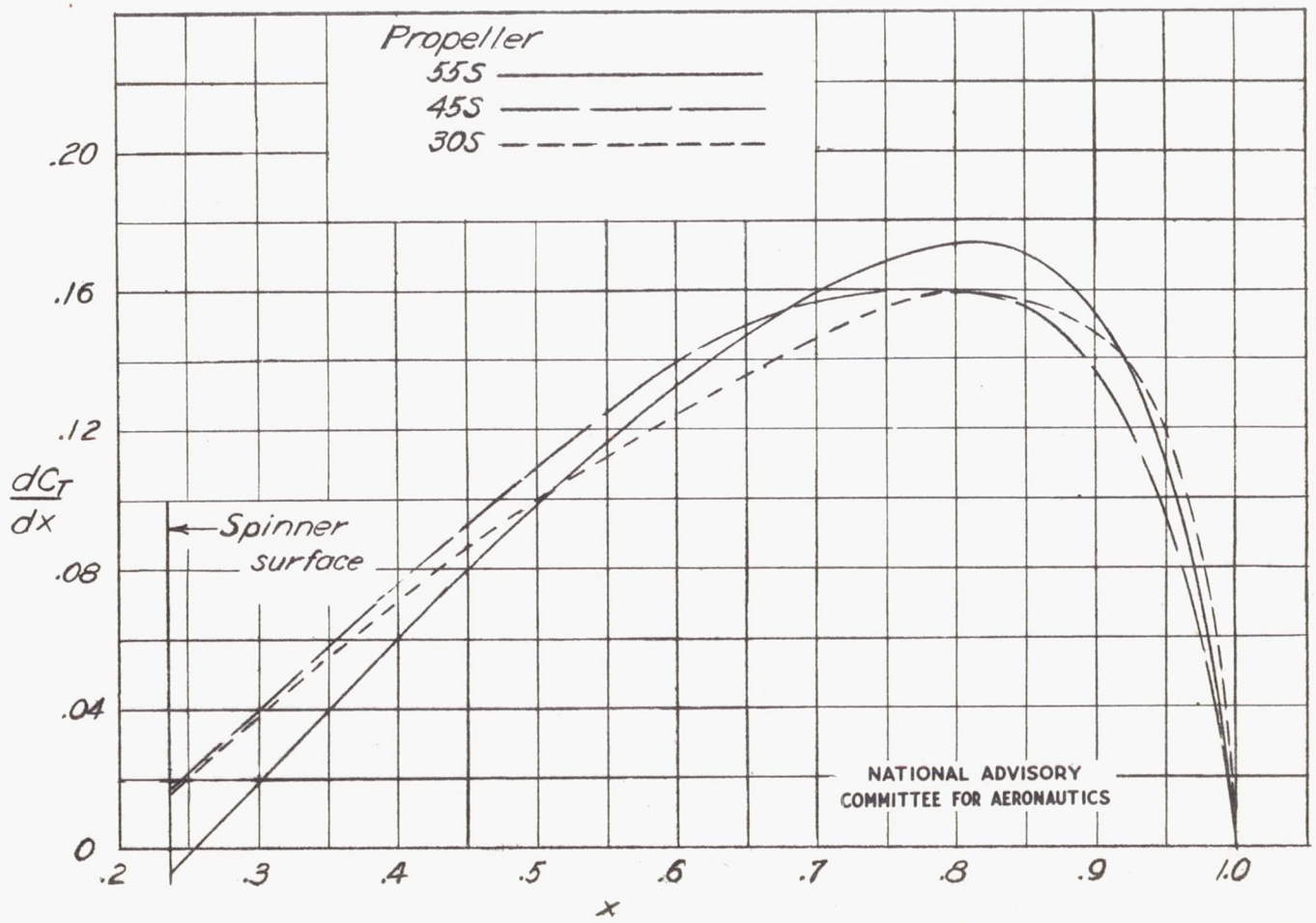
(d) High speed. $C_p = 0.400$.



(e) High speed. $C_p = 0.320$.

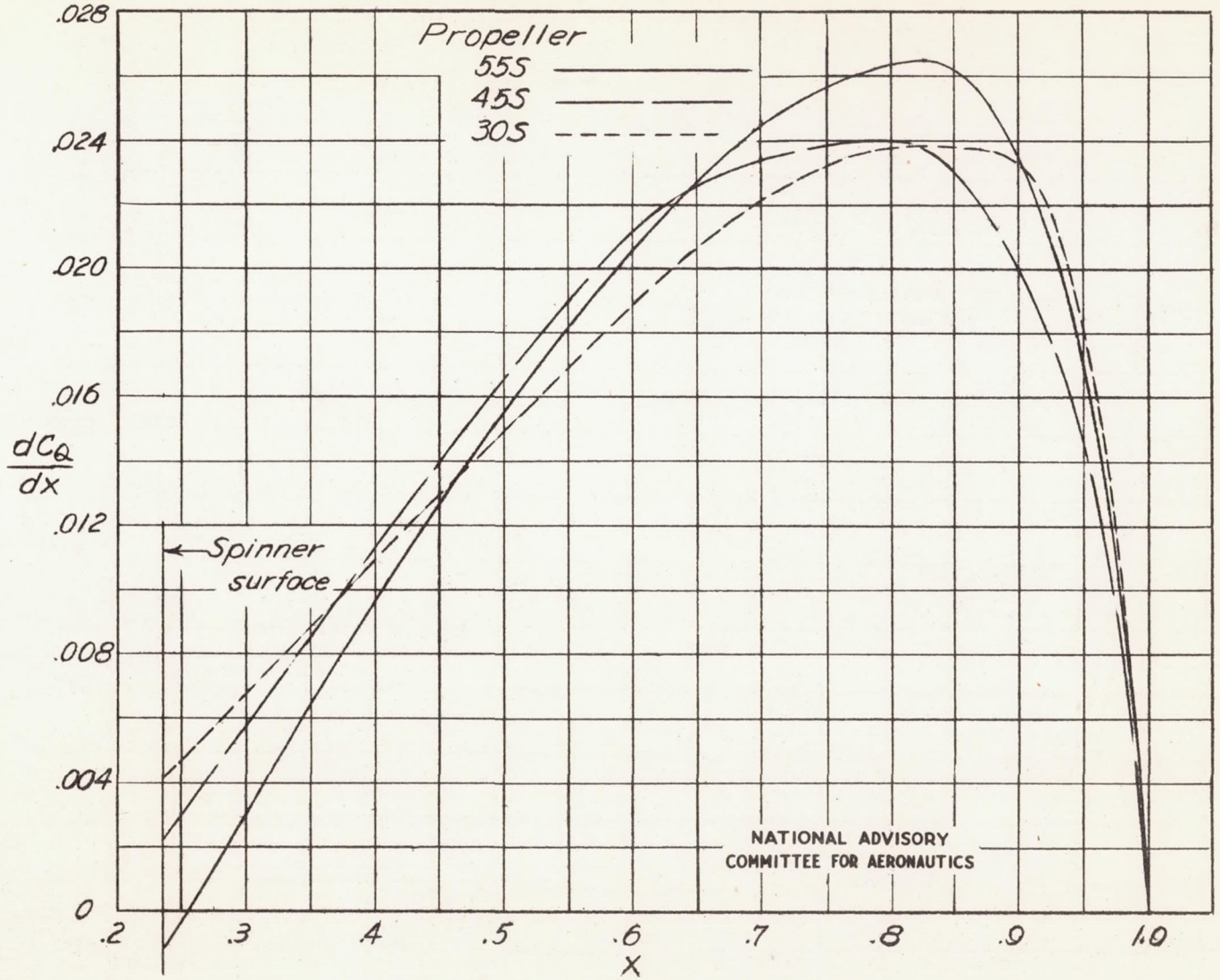
NATIONAL ADVISORY
COMMITTEE FOR AERONAUTICS

Figure 23.- Variation of η with J at several constant values of C_p.



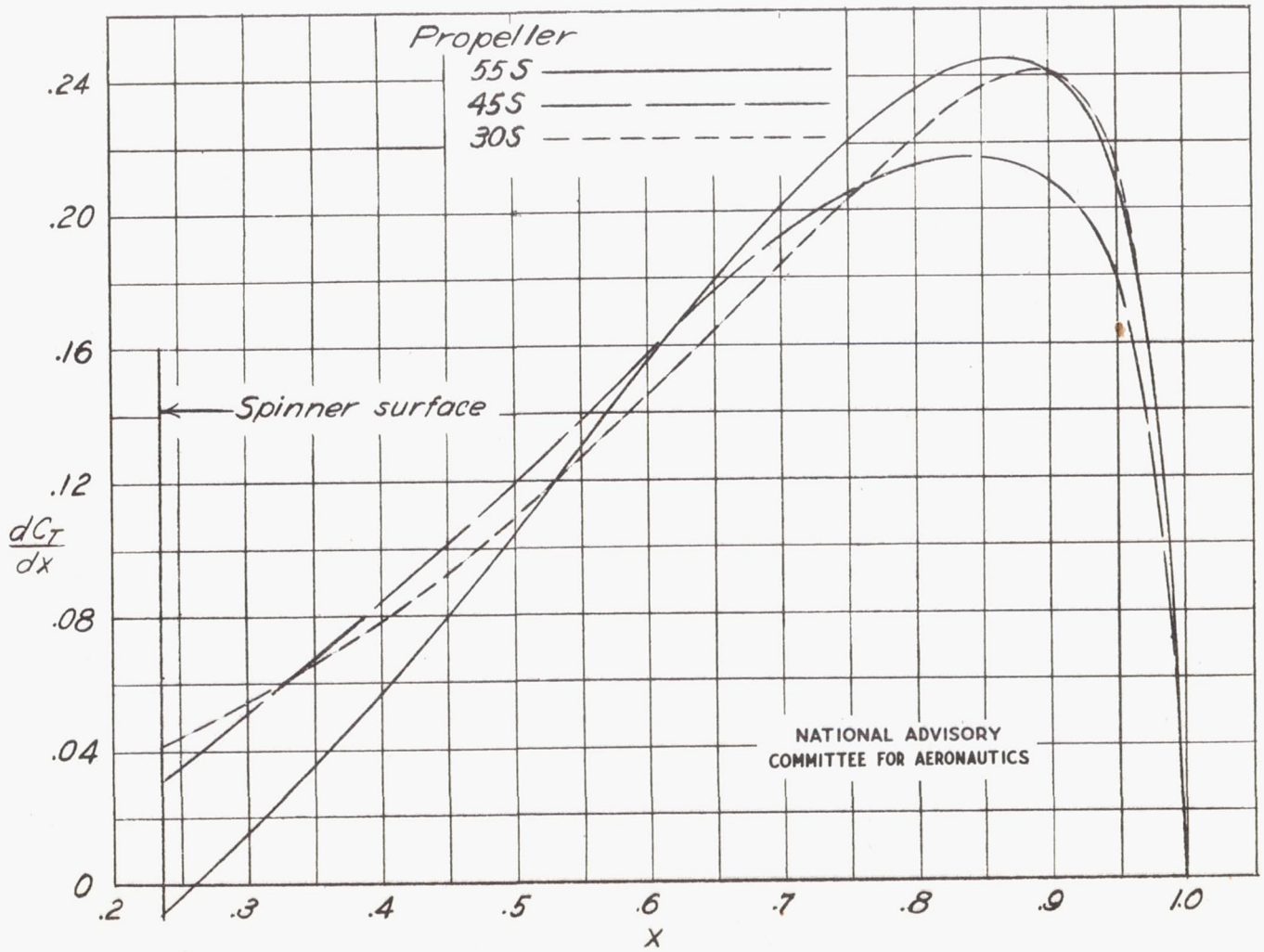
(a) Thrust.

Figure 24.- Grading curves at take-off. C_p = 0.080; J = 0.80.



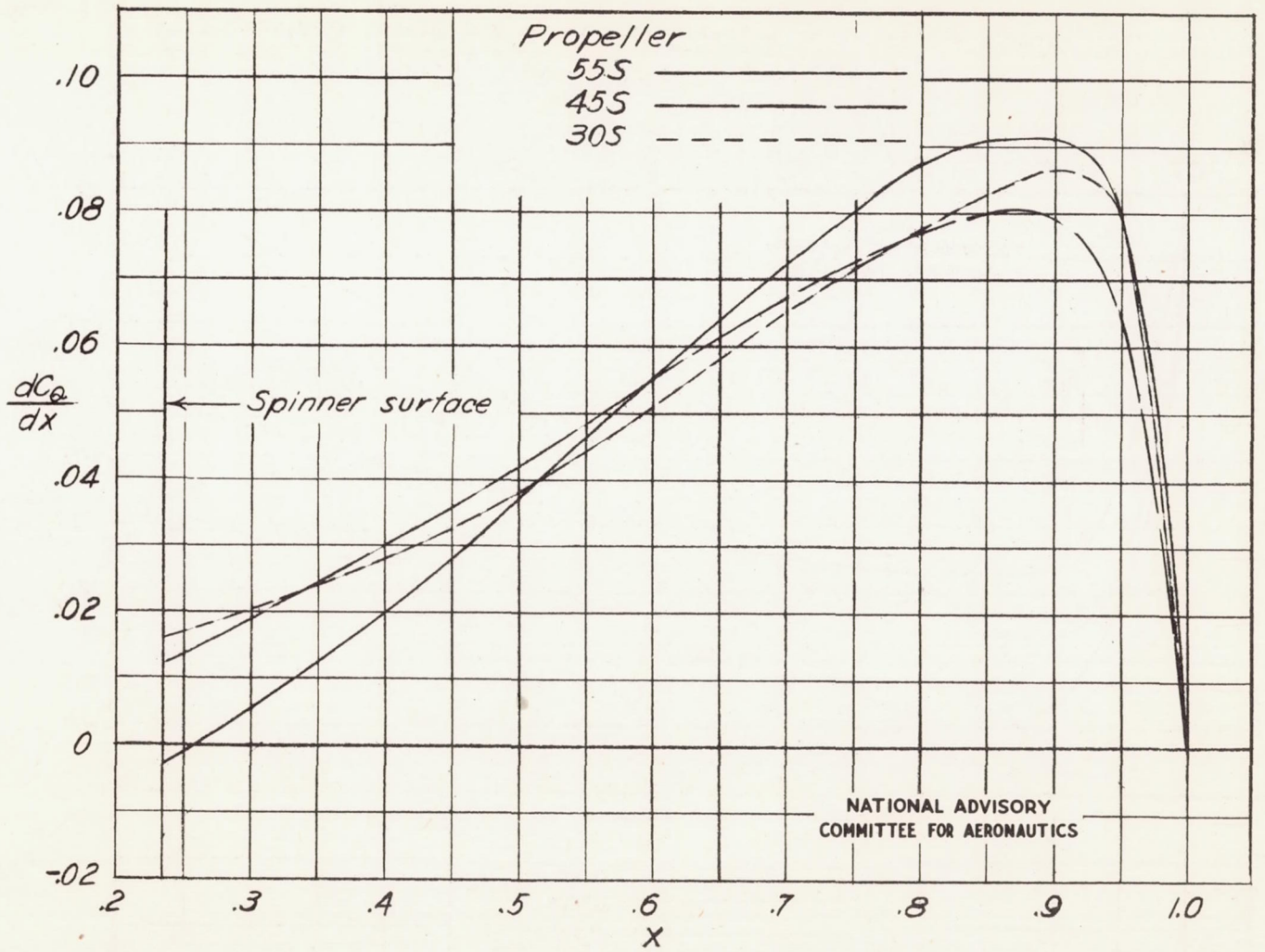
(b) Torque.

Figure 24.- Concluded.



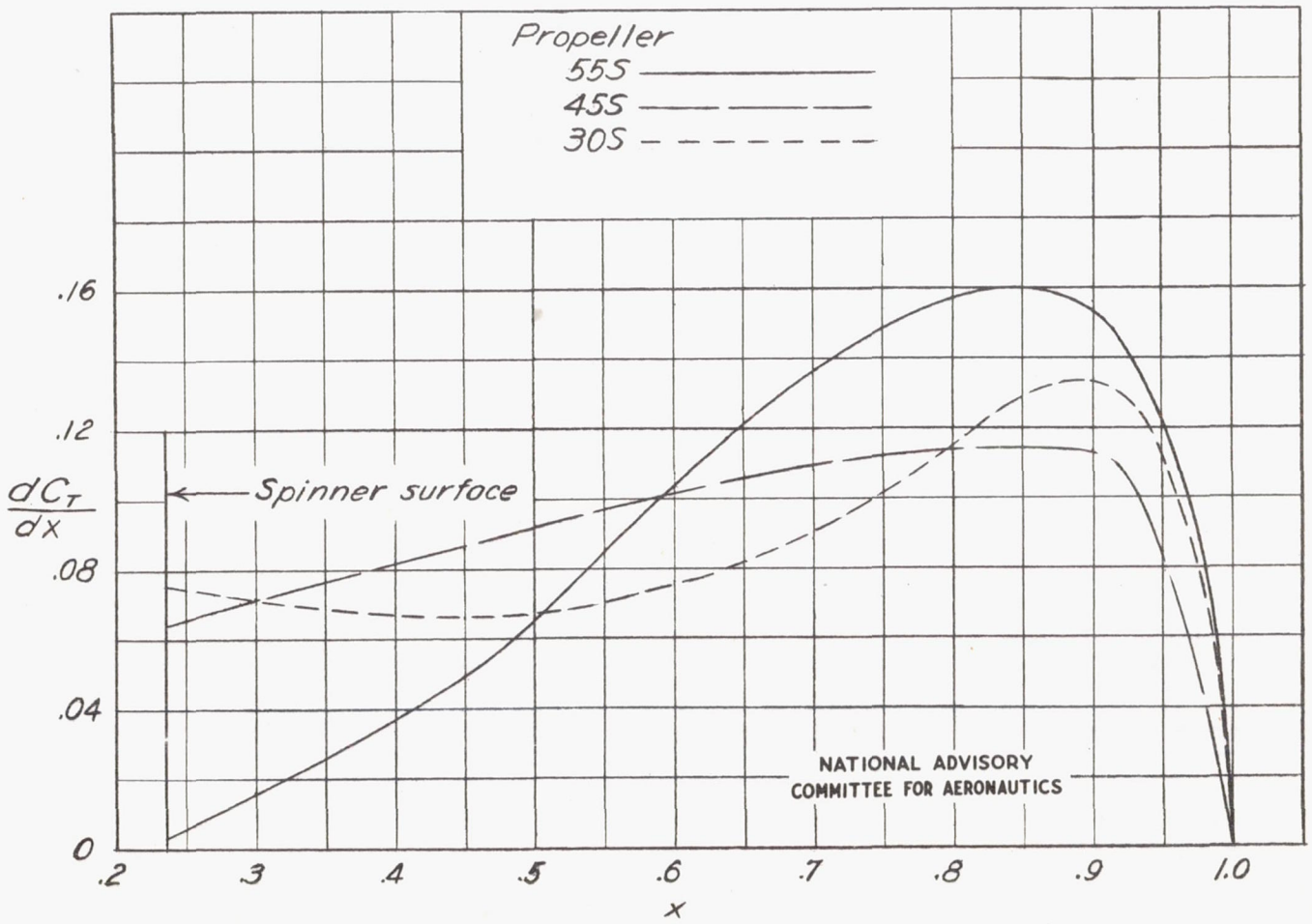
(a) Thrust.

Figure 25.- Grading curves at climb. C_p = 0.246; J = 2.00.



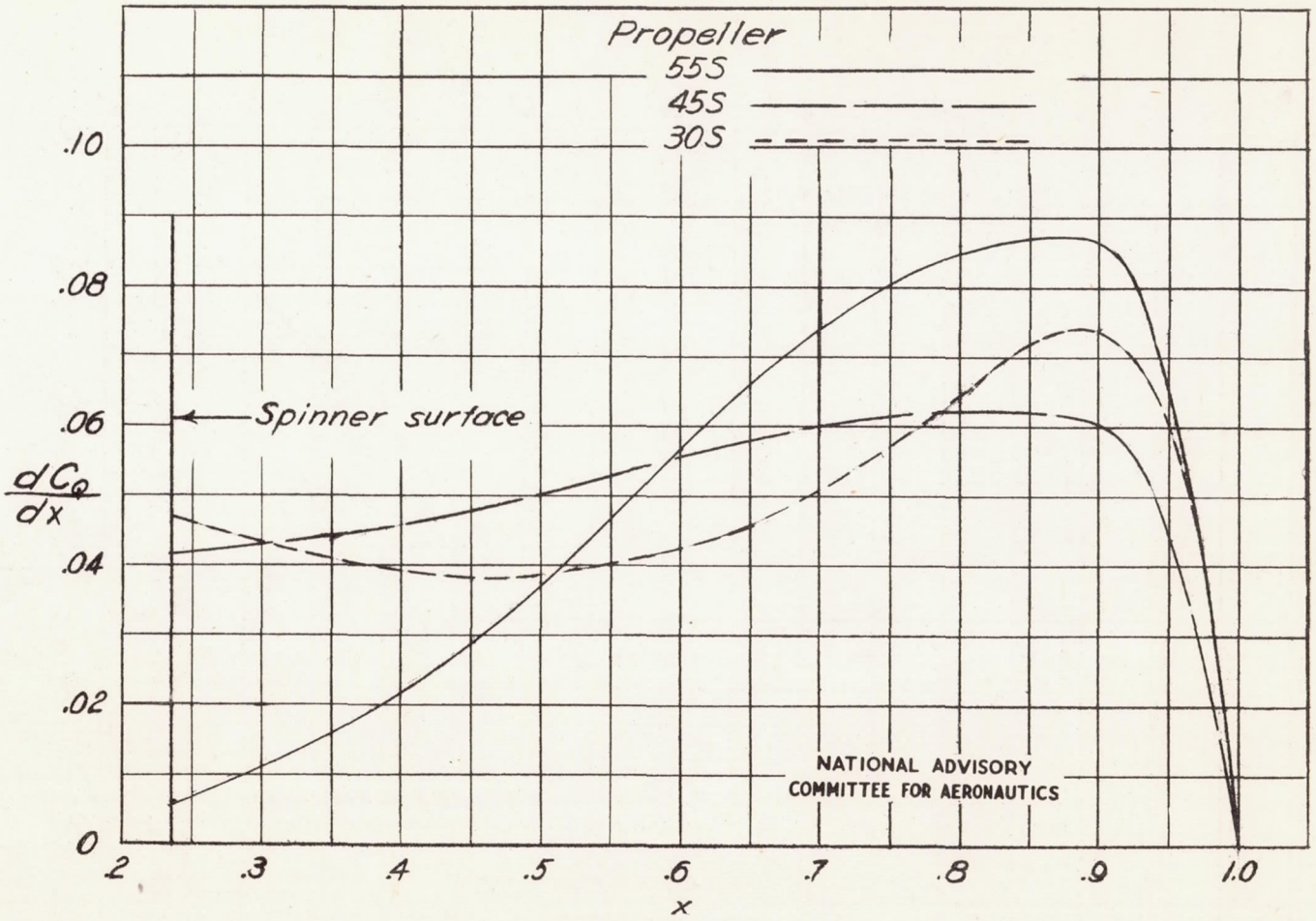
(b) Torque.

Figure 25.- Concluded.



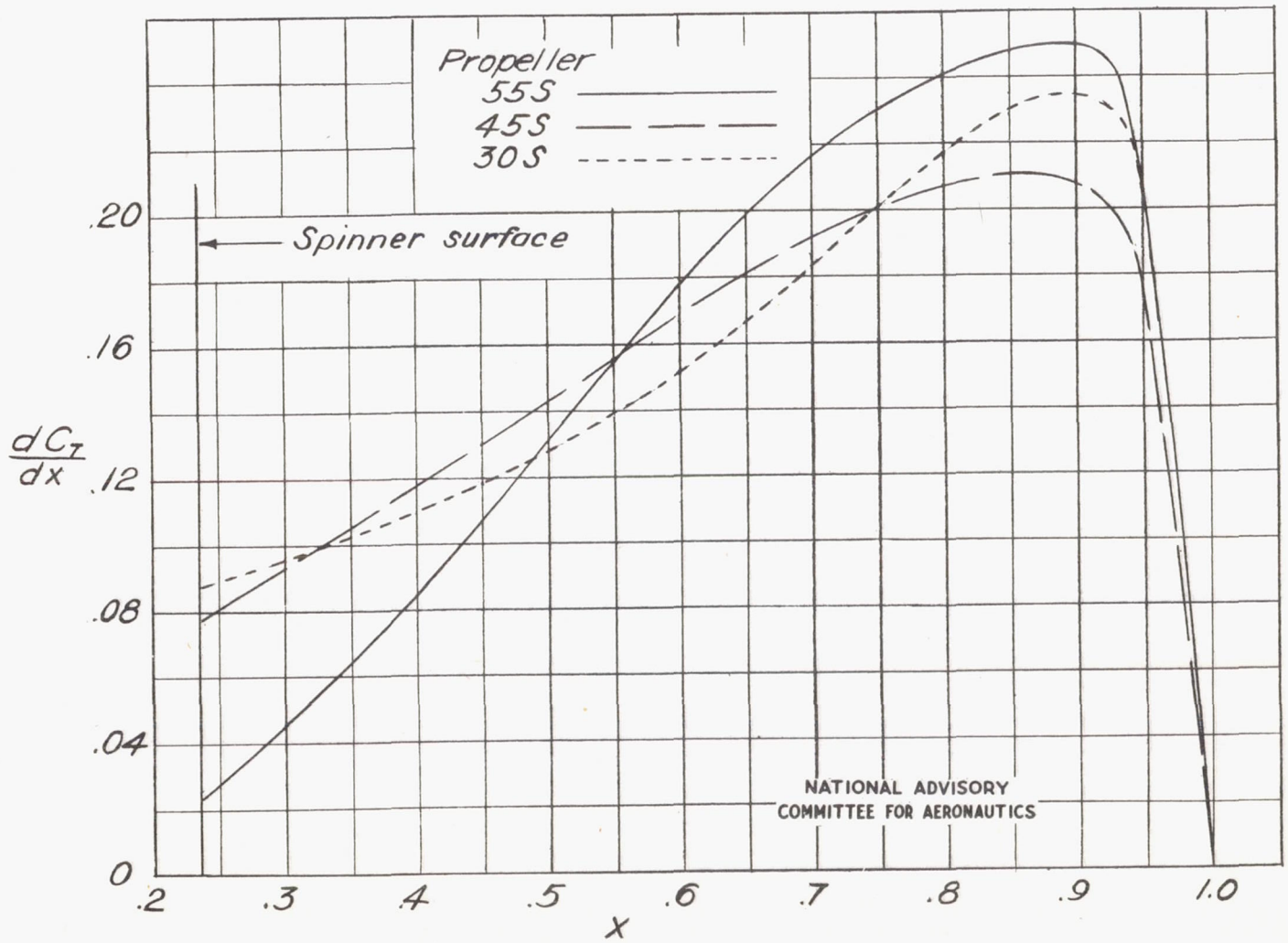
(a) Thrust.

Figure 26.- Grading curves at high speed. C_P = 0.246; J = 3.15.



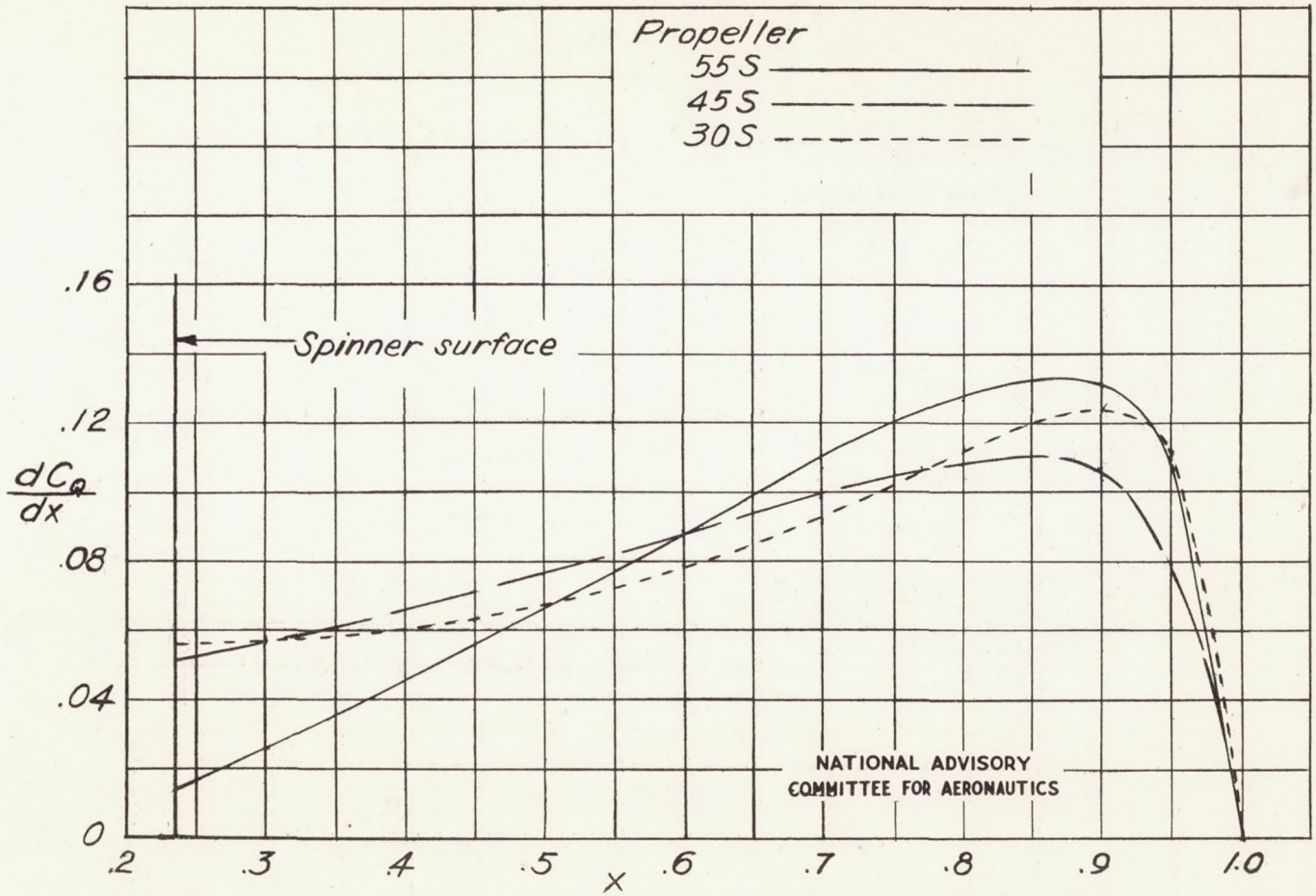
(b) Torque.

Figure 26.- Concluded.



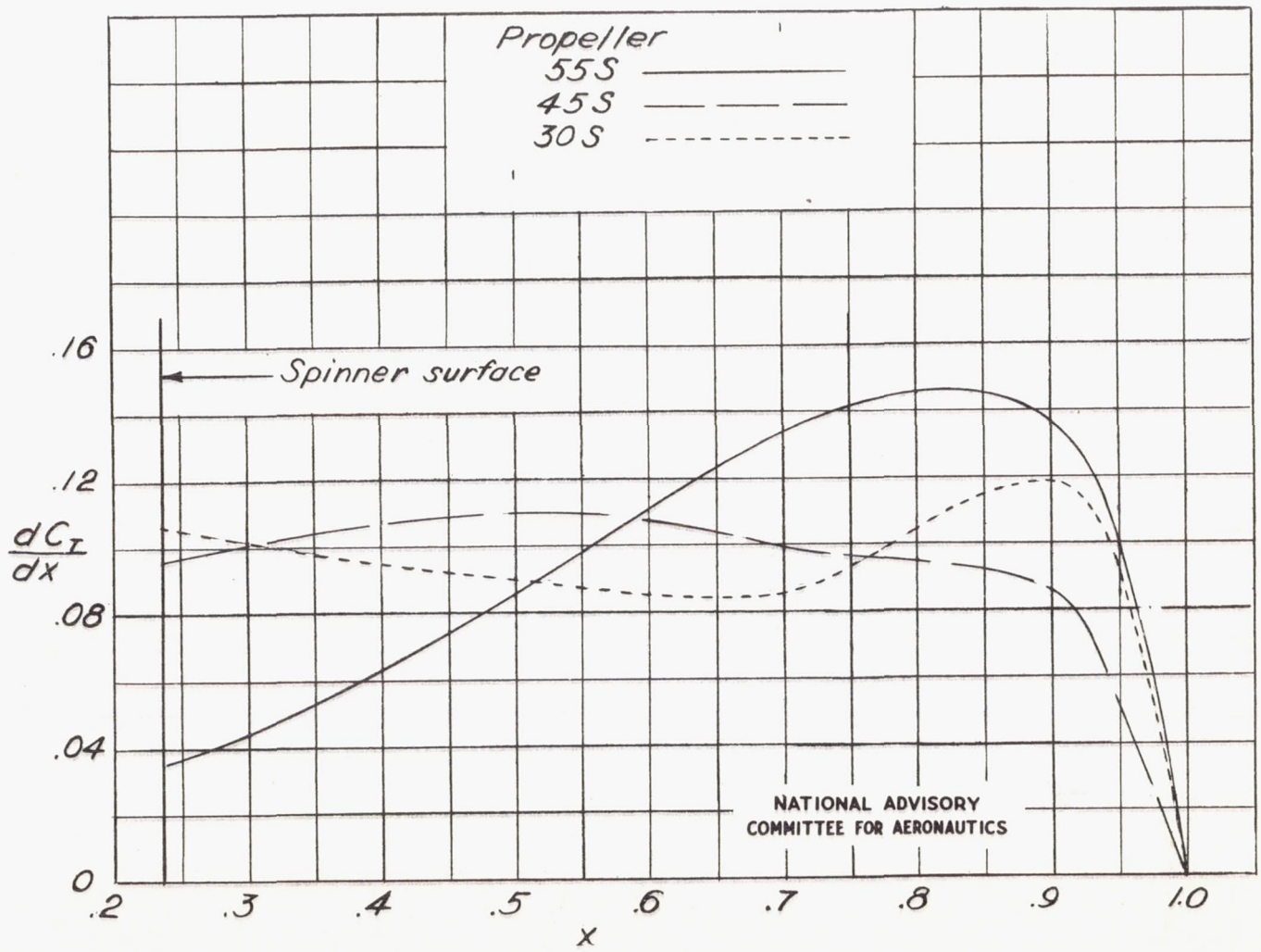
(a) Thrust.

Figure 27.- Grading curves at high speed. C_p = 0.400; J = 3.00.



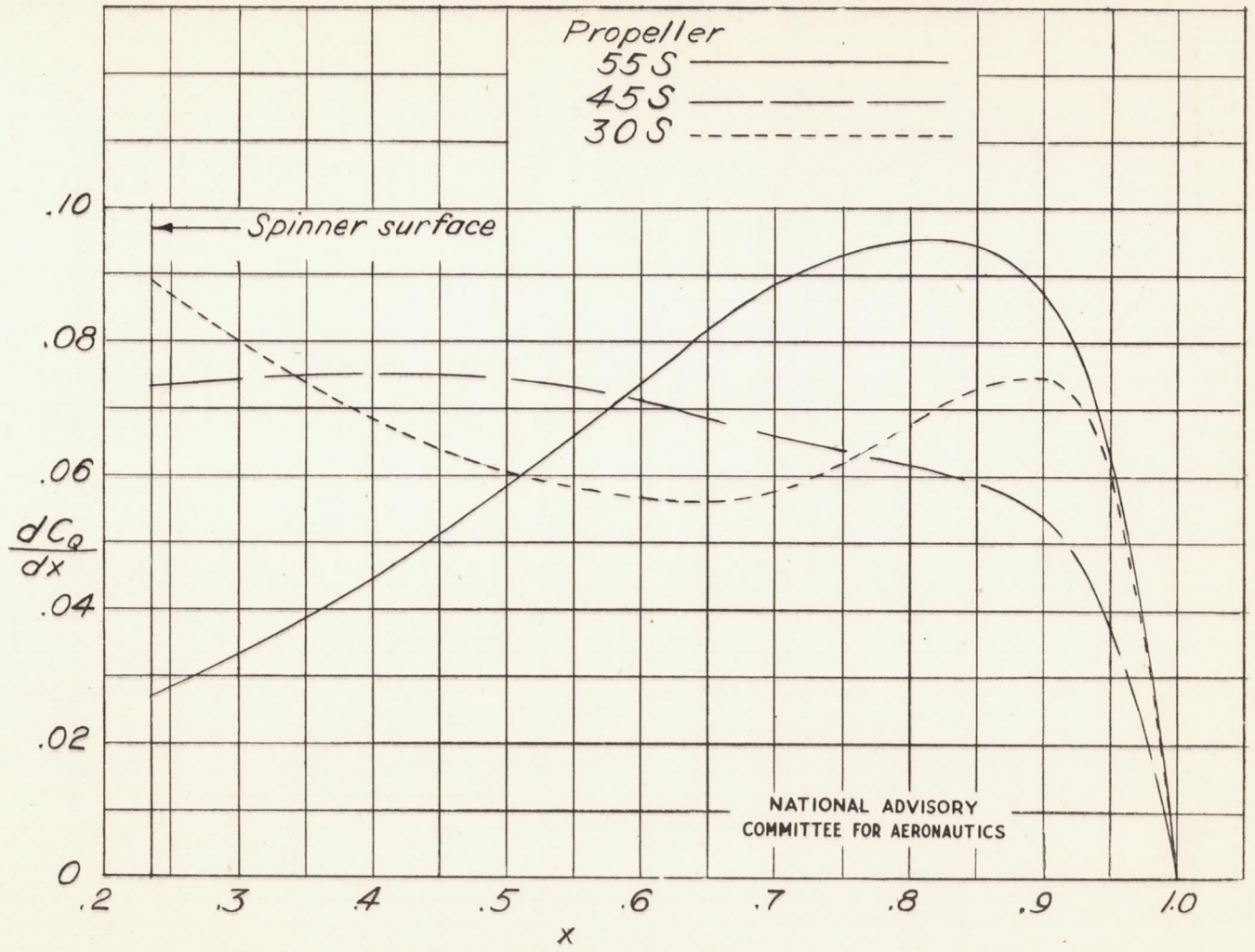
(b) Torque.

Figure 27.- Concluded.



(a) Thrust.

Figure 28.- Grading curves at high speed. C_p = 0.320; J = 3.80.



(b) Torque.

Figure 28.- Concluded.

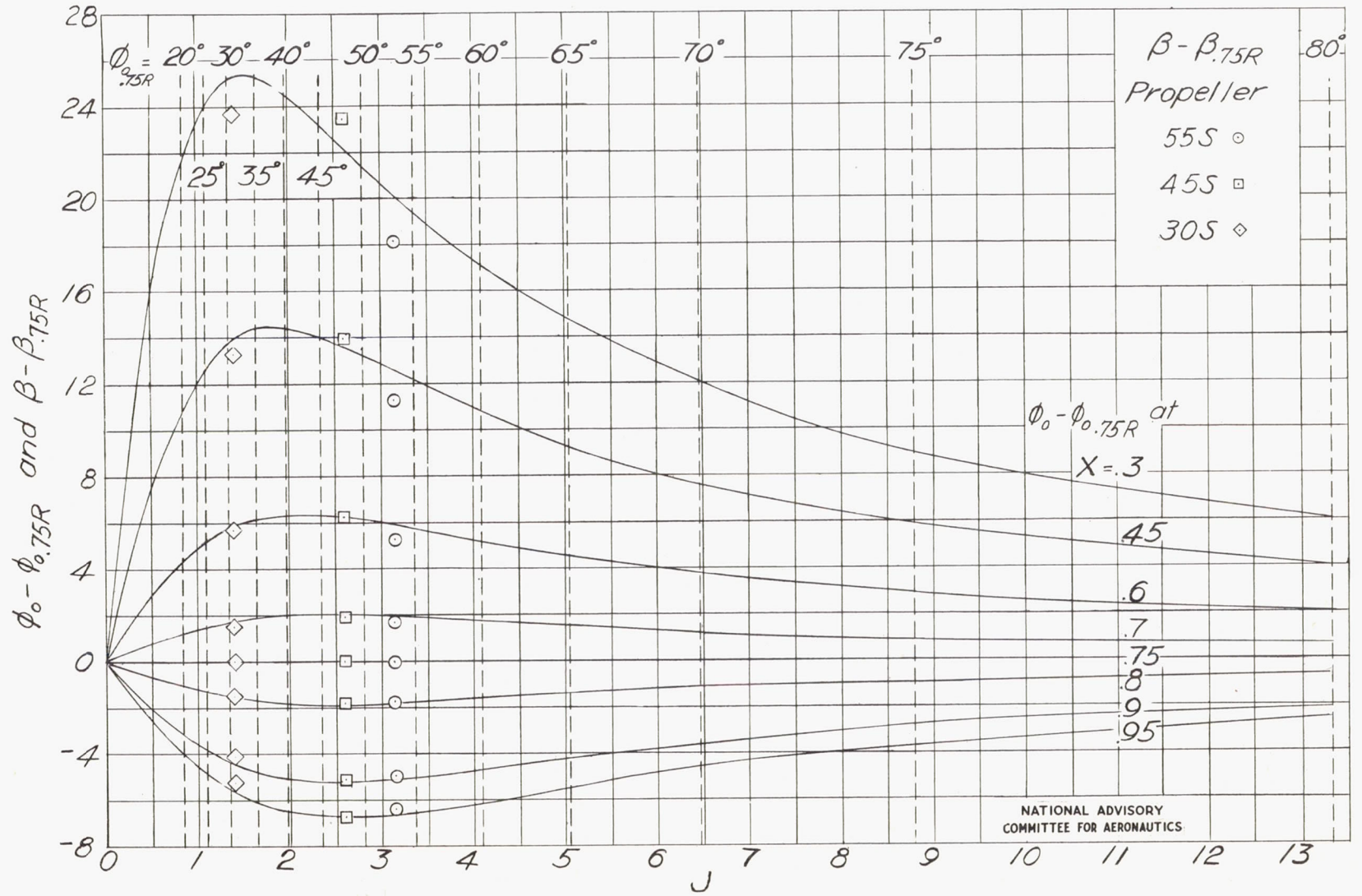
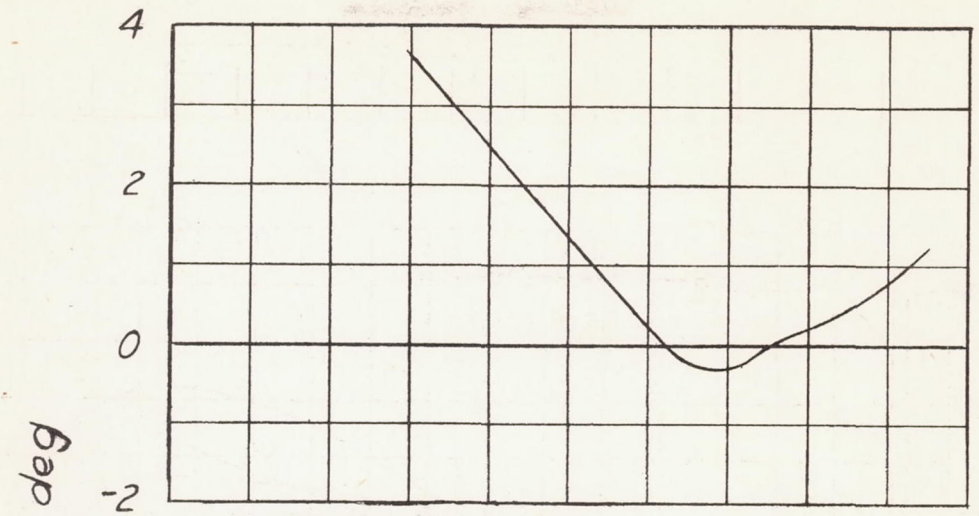
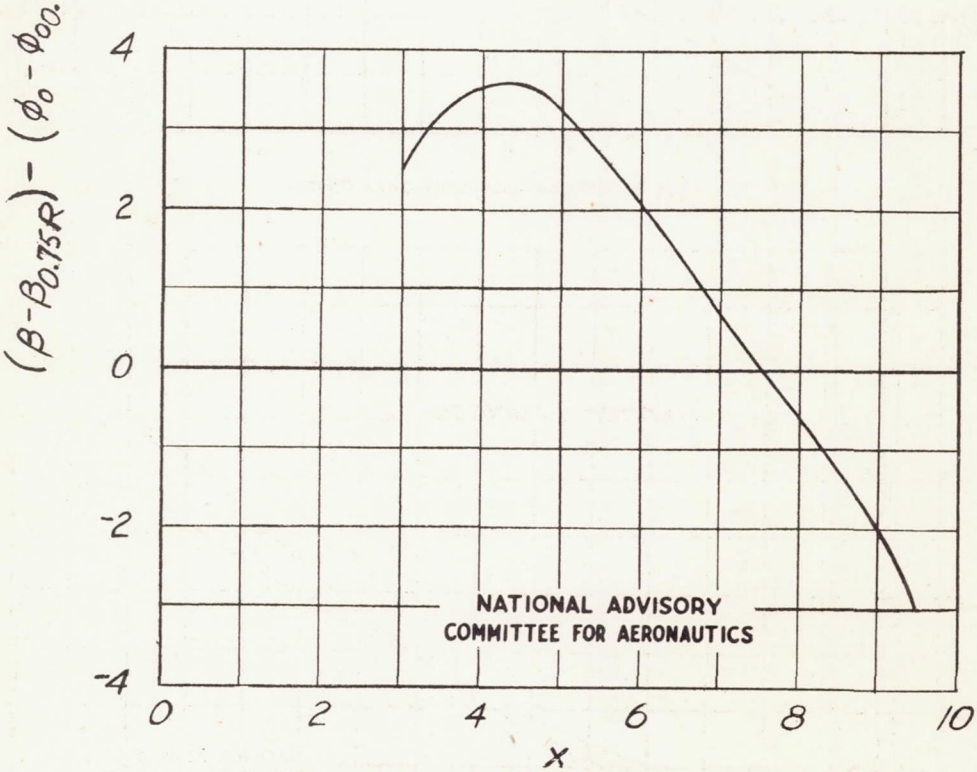


Figure 29.- Variation of resultant air-stream twist with advance-diameter ratio. (Air-stream twist based on geometric helix angle with assumption of no body interference.)



(a) Propeller 30S; J = 3.8.



(b) Propeller 45S; J =0.8.

Figure 30.- Variation of geometric angle of attack, based on chord line.

$\beta_{0.75R} - \phi_{o0.75R} = 0°$.

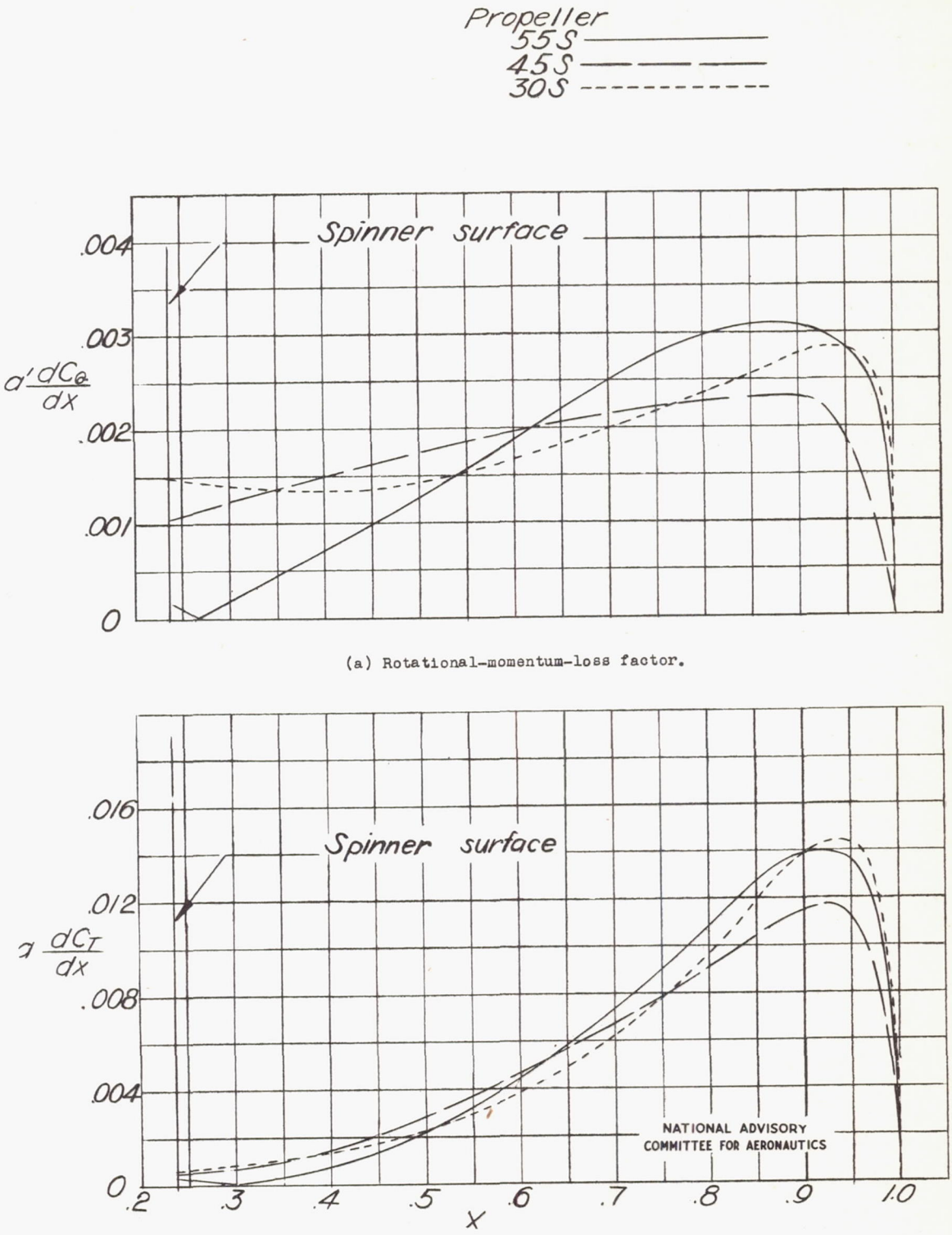
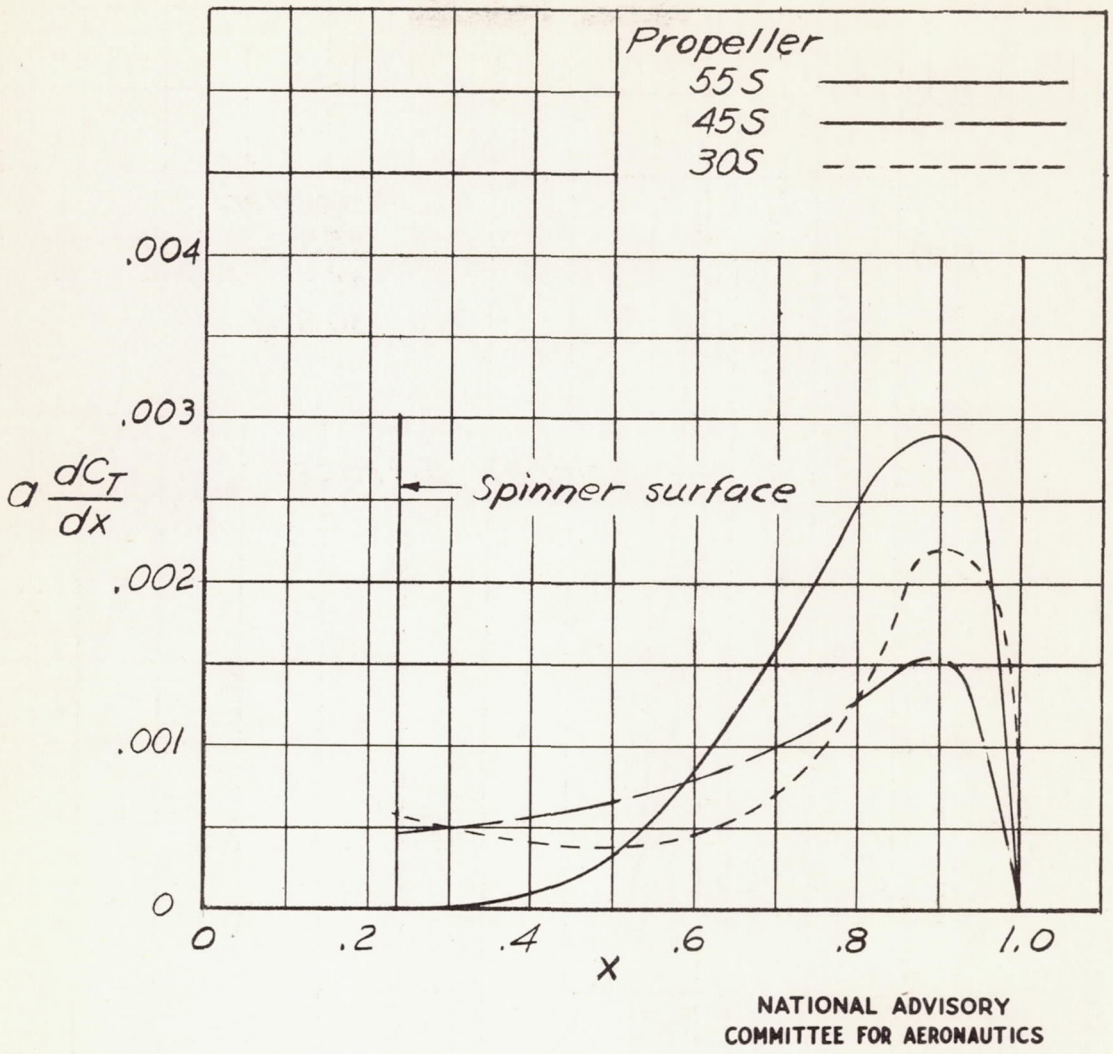
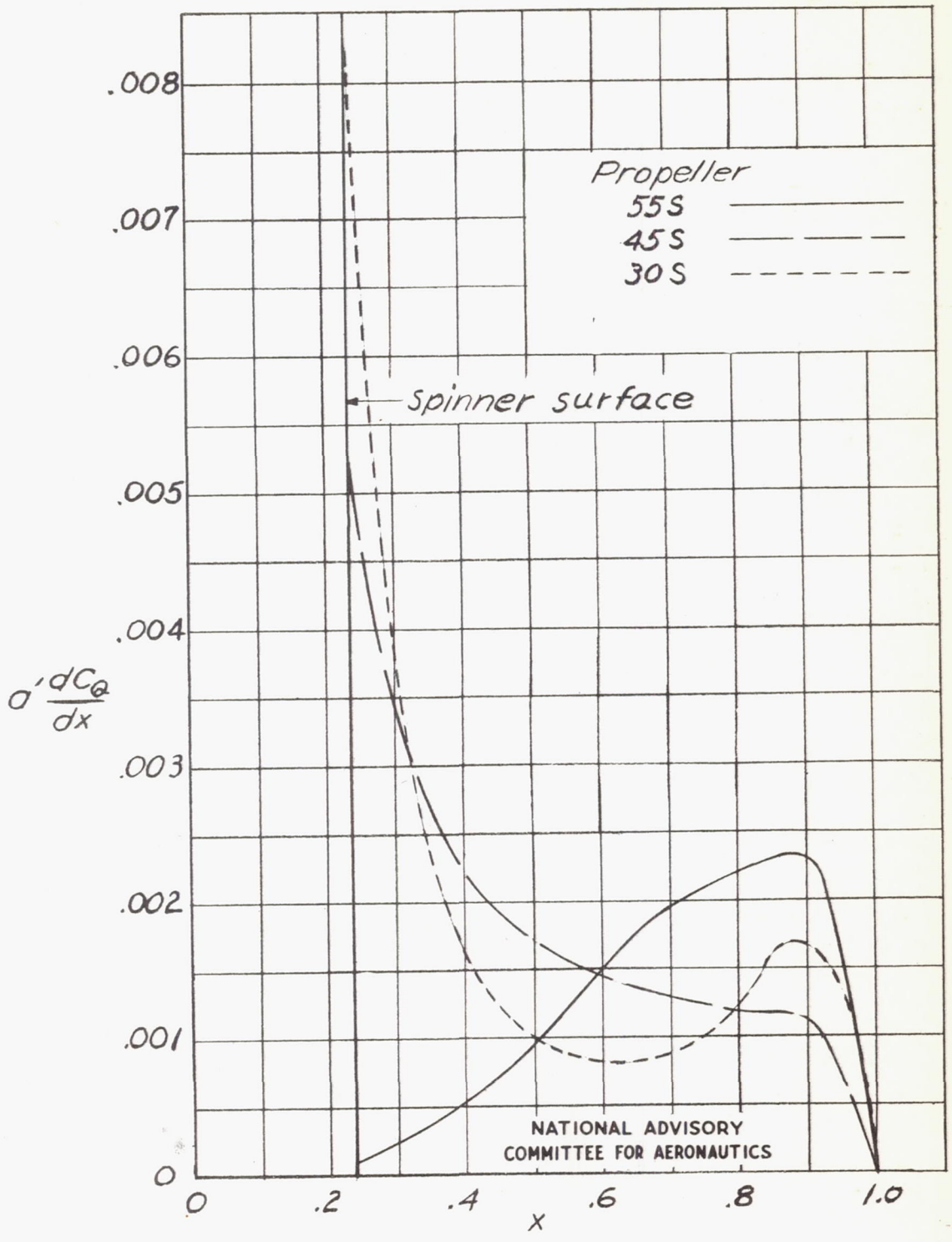


Figure 31.- Distribution of induced energy losses in climb. C_p = 0.246; J = 2.00.



(a) Axial-momentum-loss factor.

Figure 32.- Distribution of induced energy losses at high speed. $C_p = 0.246$; $J = 3.15$.



(b) Rotational-momentum-loss factor.

Figure 32.- Concluded.

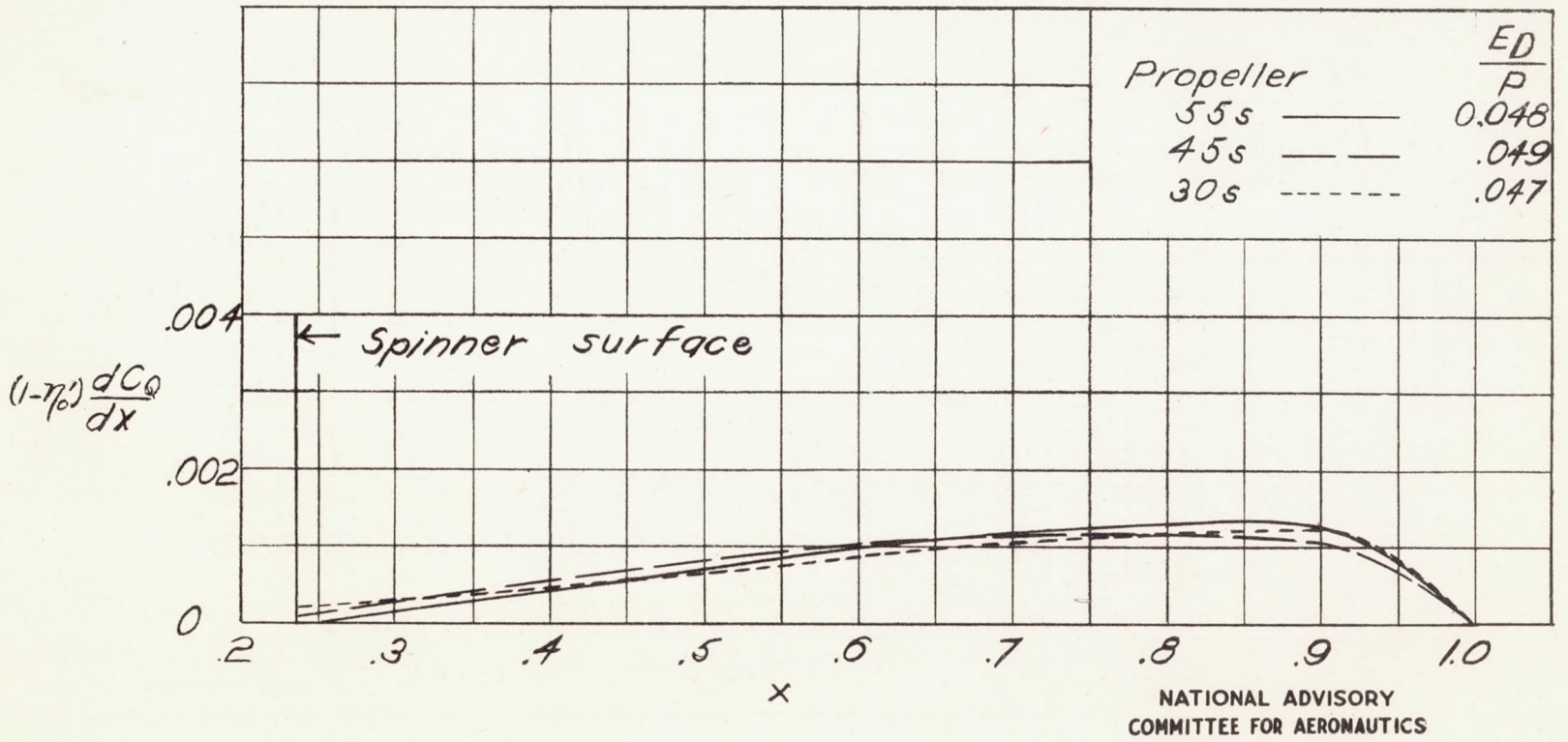


Figure 33.- Distribution of fractional energy loss due to profile drag. Take off. Cp = 0.080; J = 0.80.

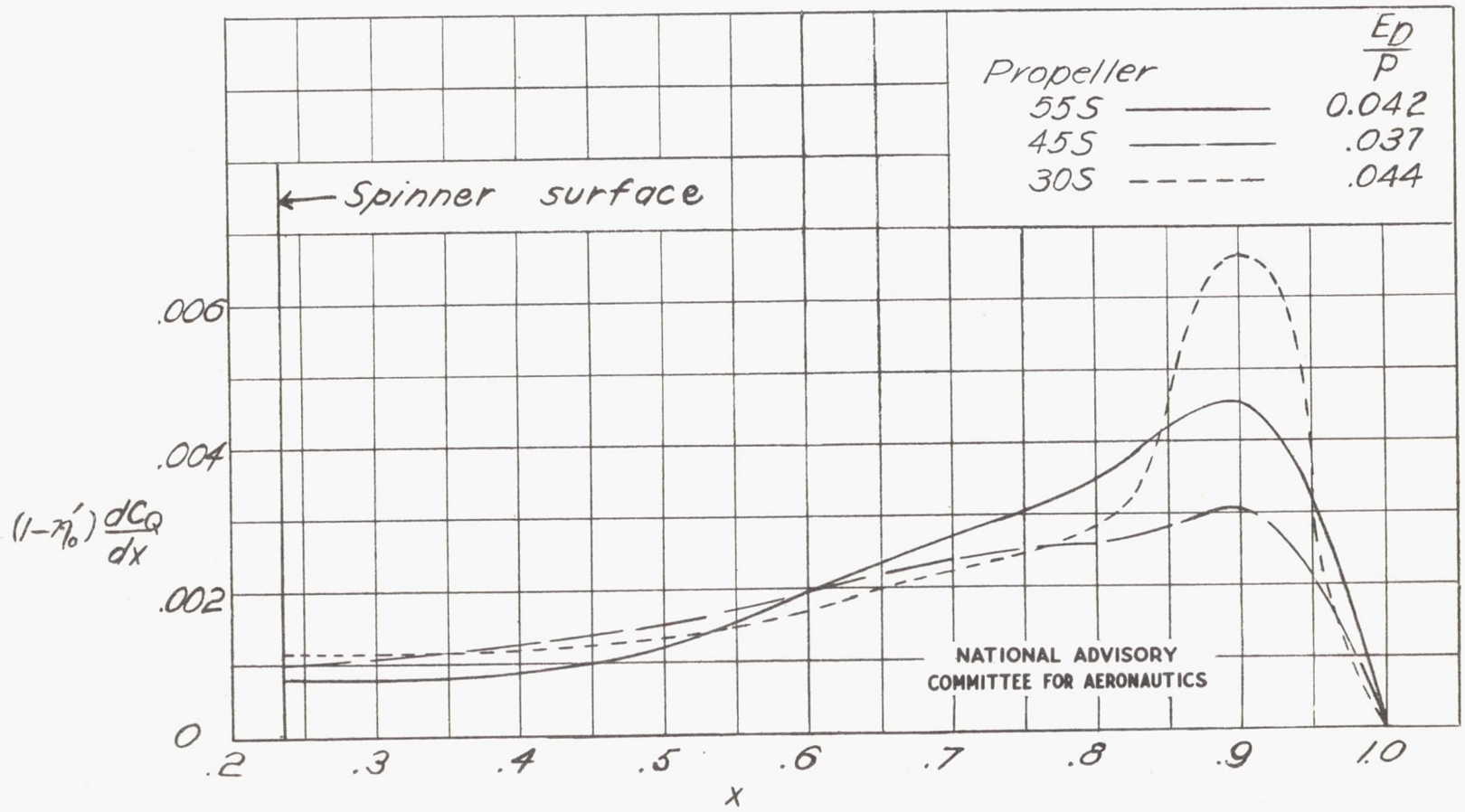


Figure 34.- Distribution of fractional energy loss due to profile drag. Climb. C_p = 0.246; J = 2.00.

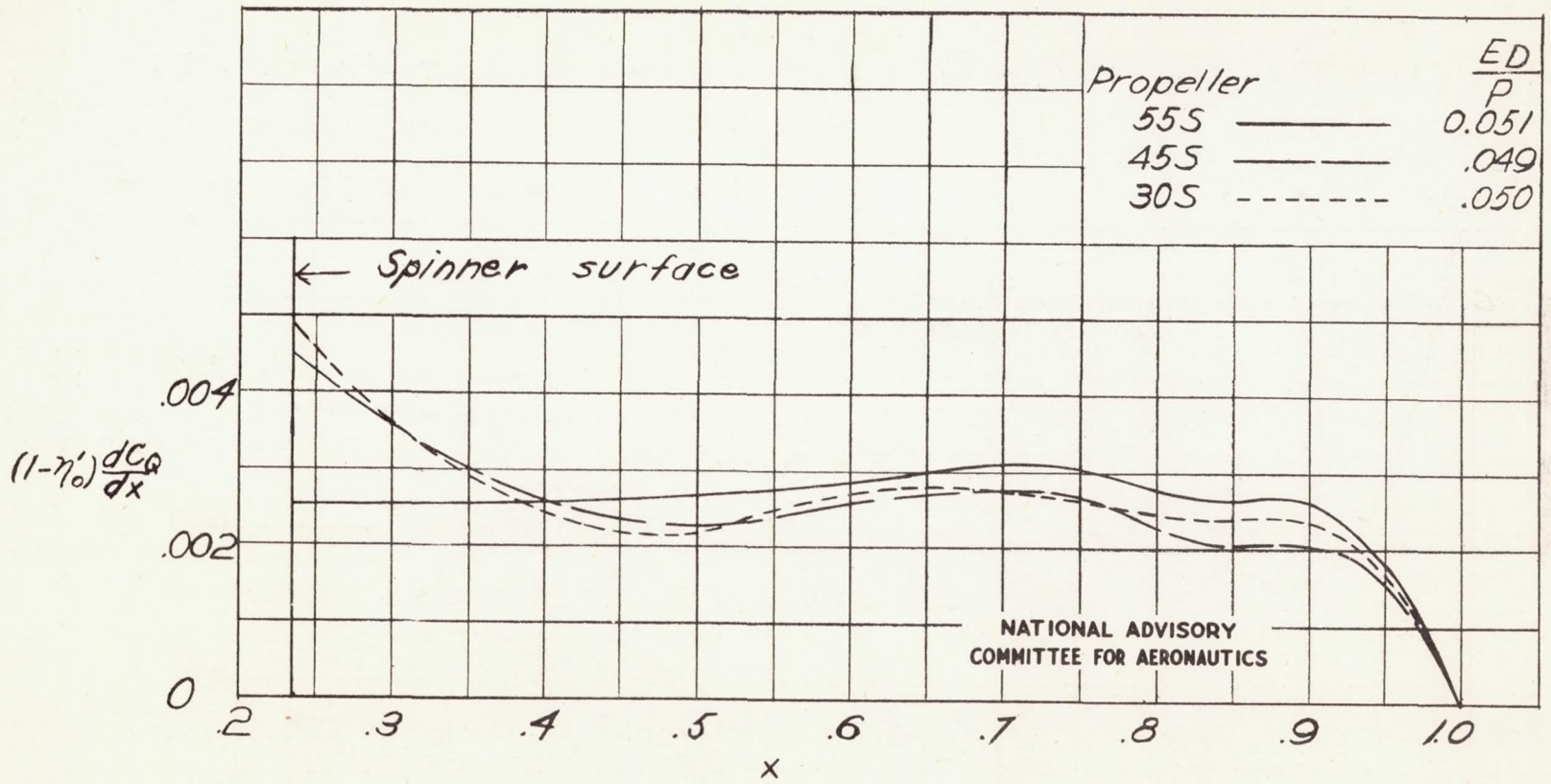


Figure 35.- Distribution of fractional energy loss due to profile drag. High speed. $C_p = 0.246$; $J = 3.15$.

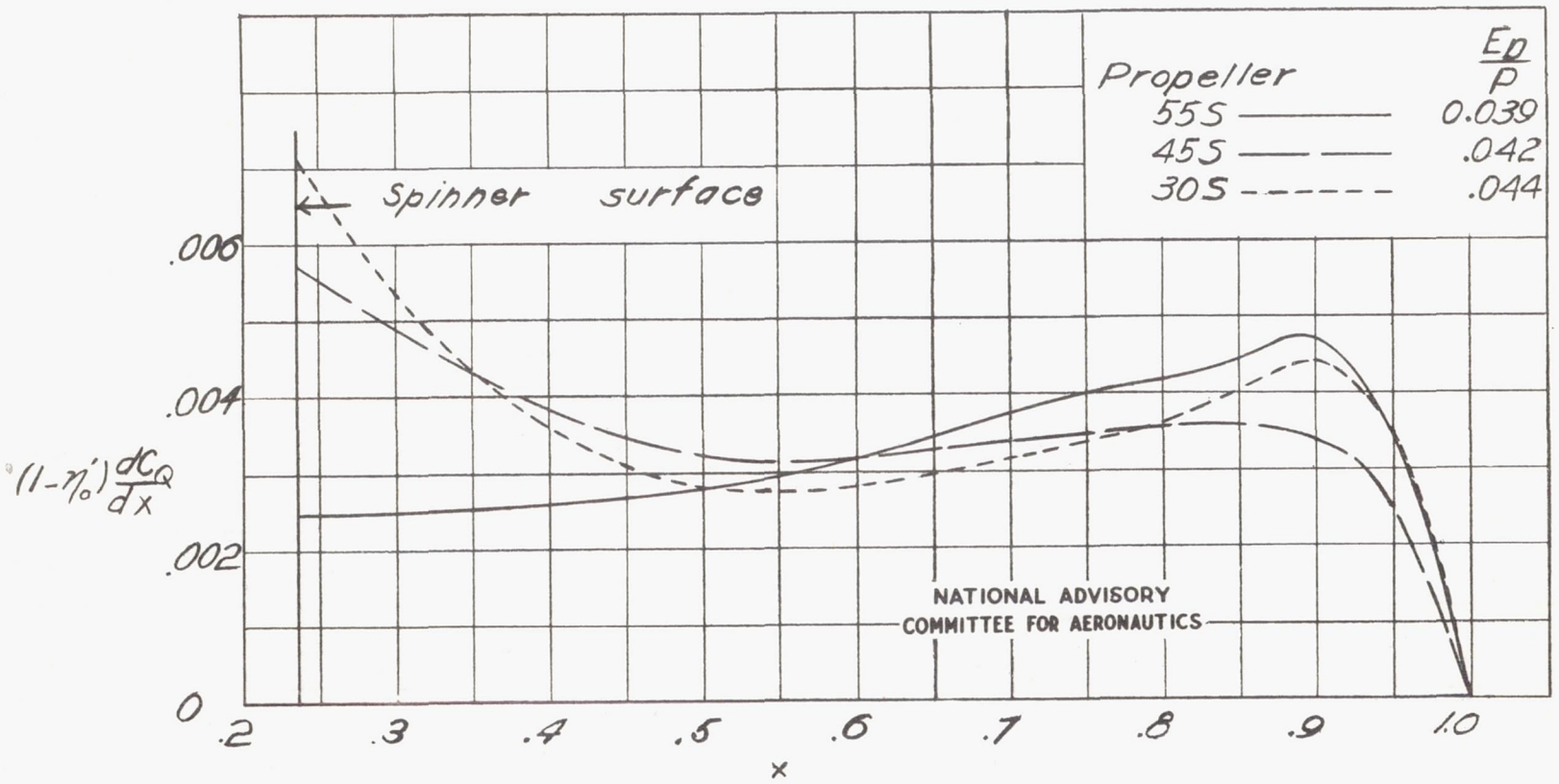


Figure 36.- Distribution of fractional energy loss due to profile drag. High speed. $C_p = 0.400$; $J = 3.00$.

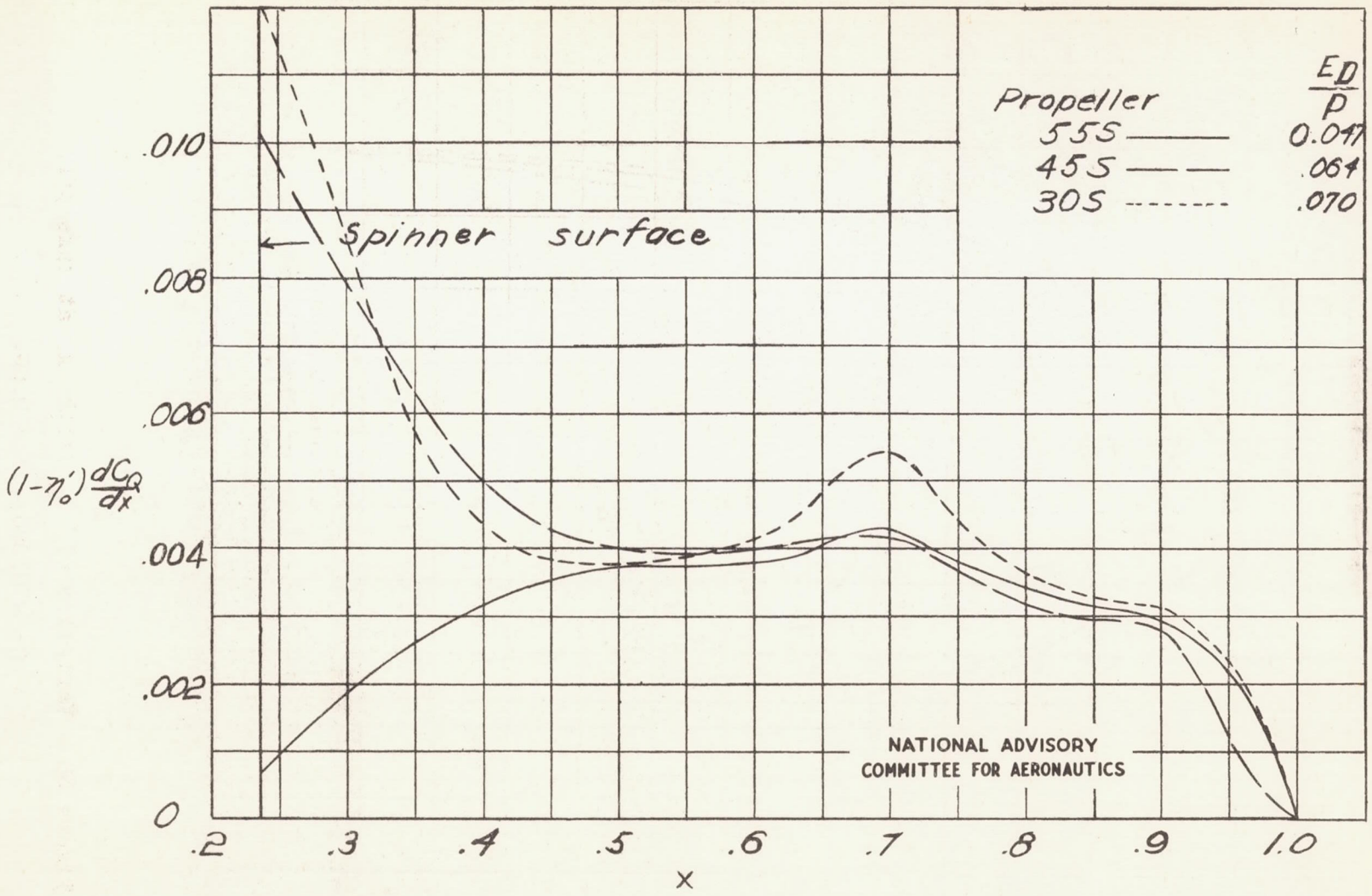


Figure 37.- Distribution of fractional energy loss due to profile drag. High speed.
Cp = 0.320; J = 3.80.

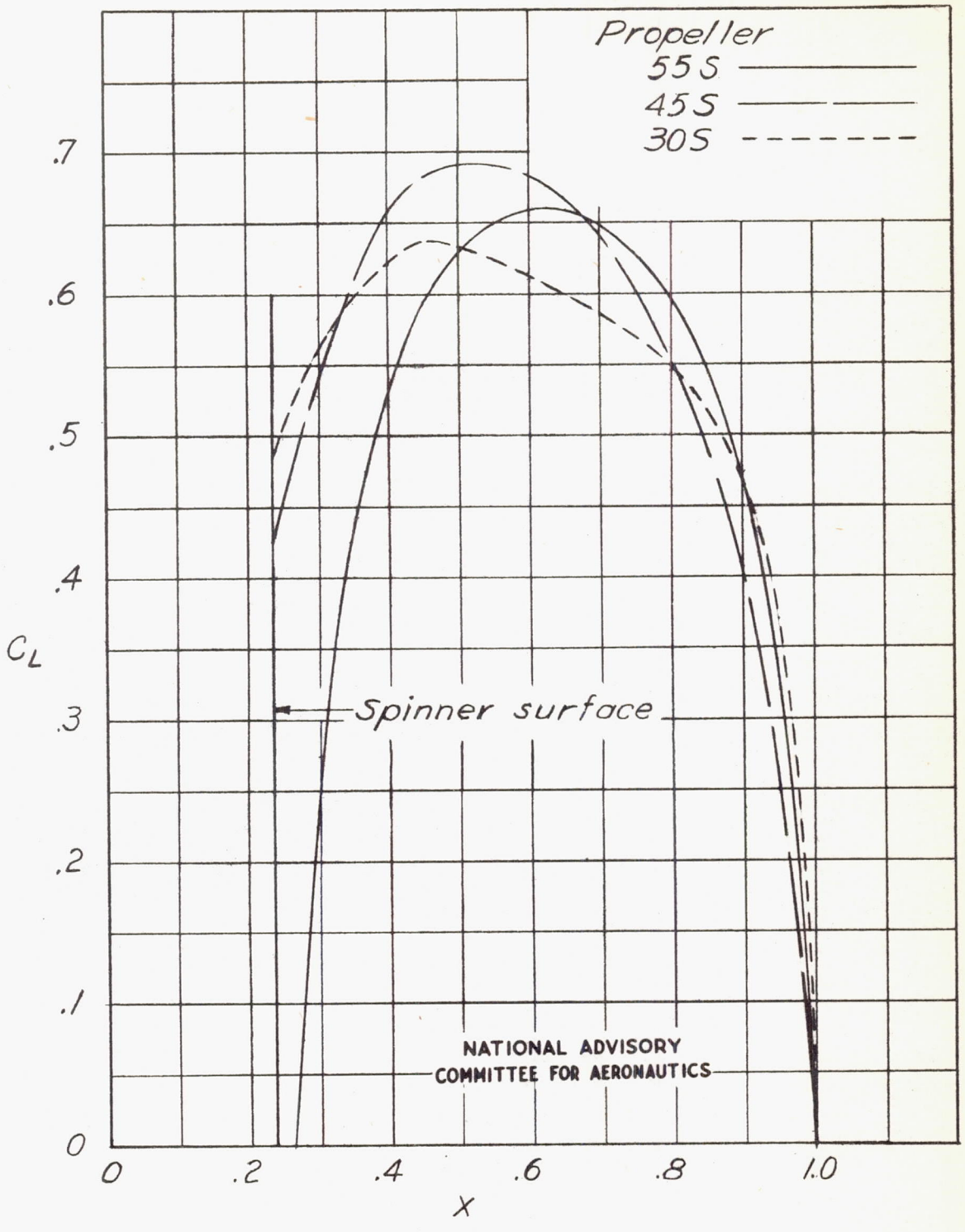


Figure 38.- Variation of C_L with x at take-off.

C_P = 0.080; J = 0.80.

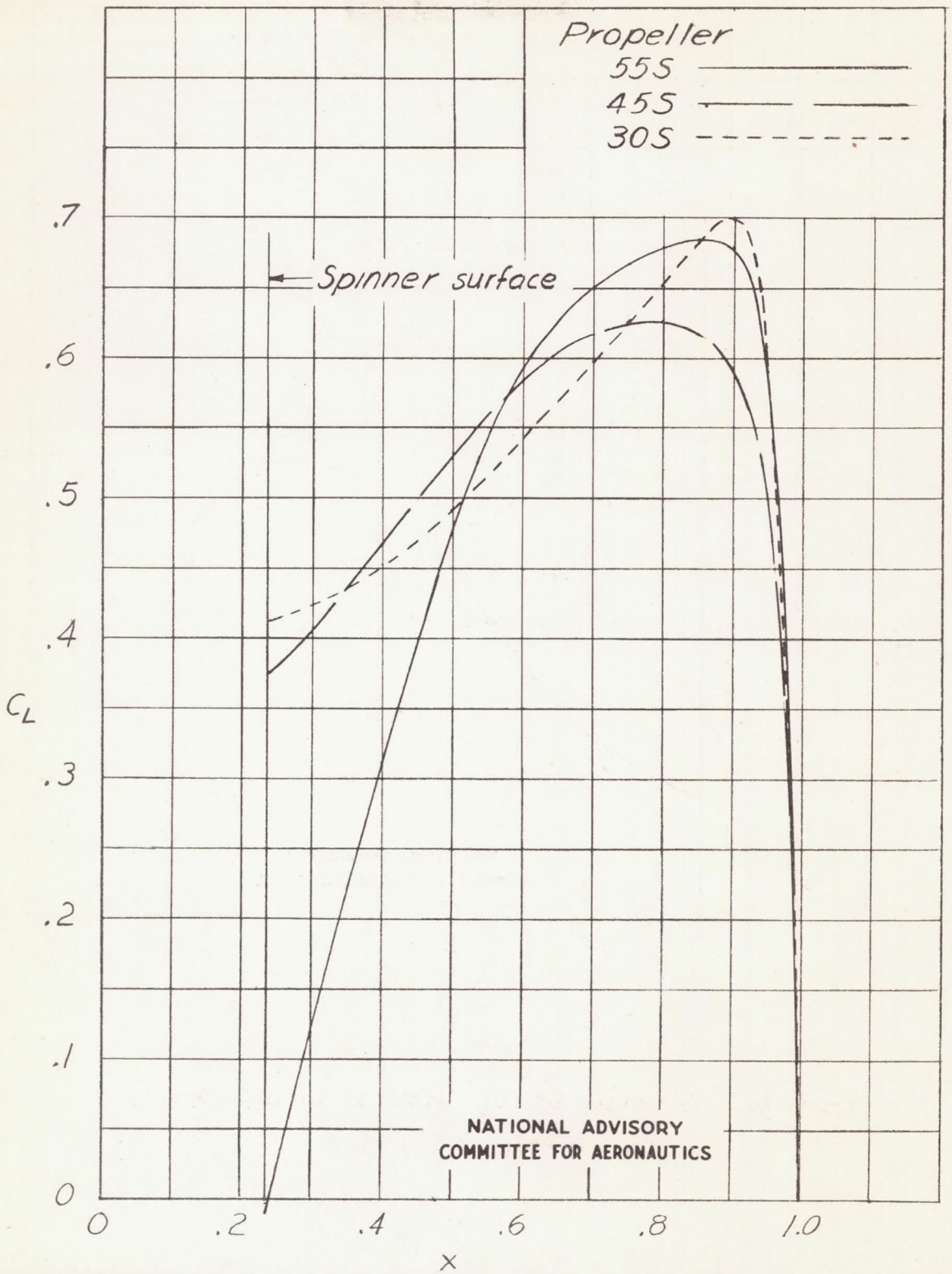


Figure 39.- Variation of C_L with x at climb.
$C_p = 0.246$; $J = 2.00$.

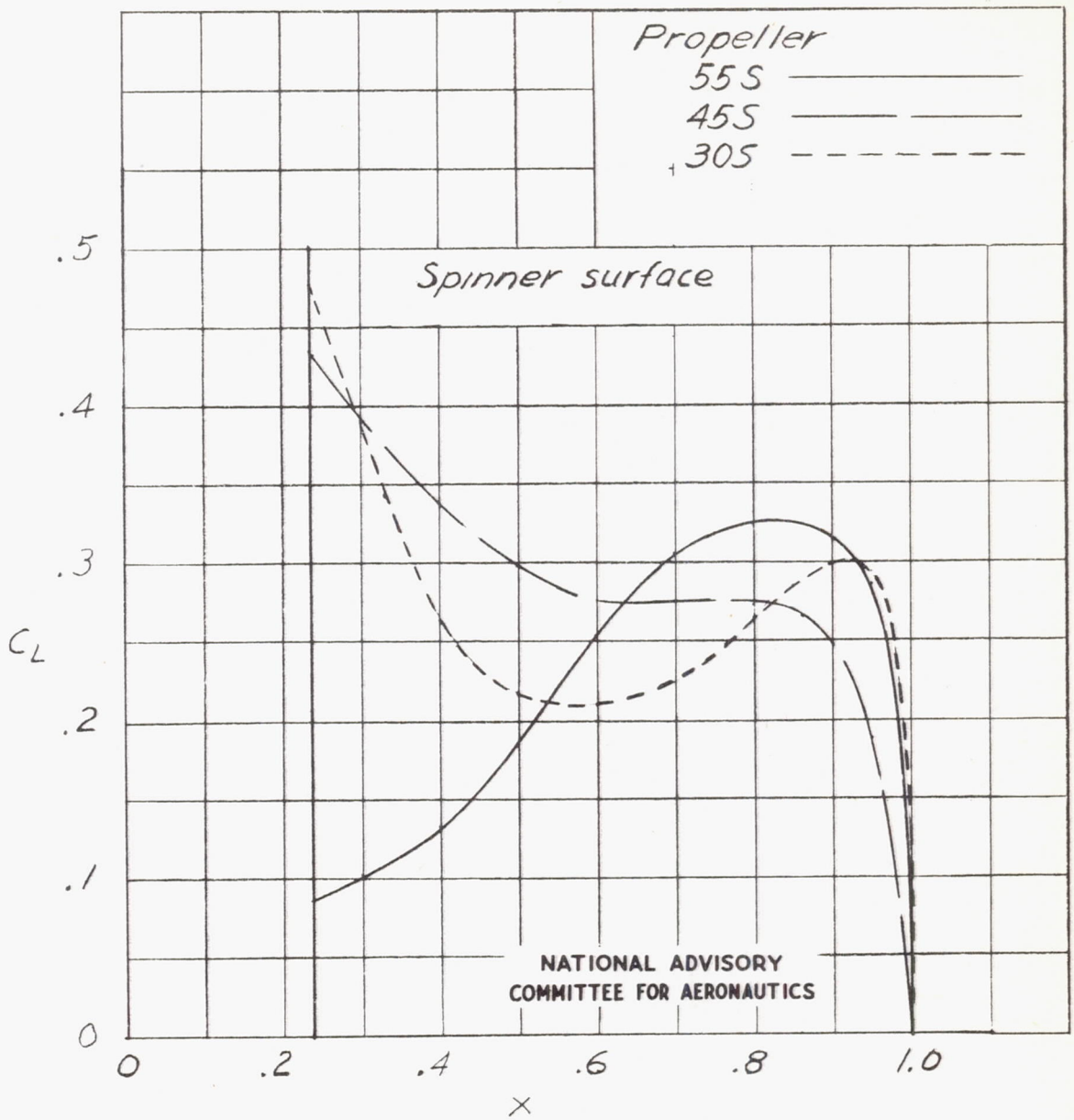


Figure 40.- Variation of C_L with x at high speed.

C_p = 0.246; J = 3.15.

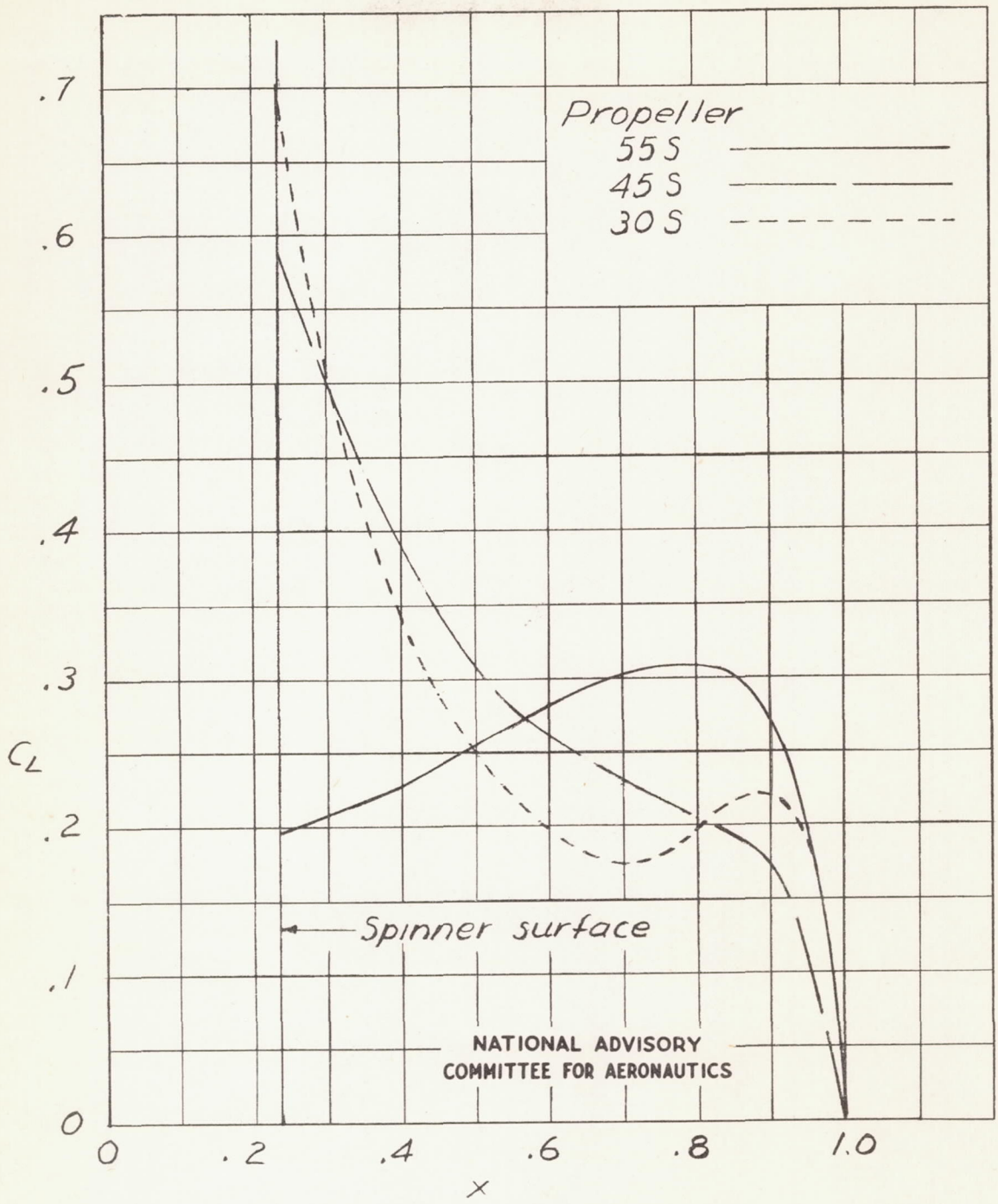


Figure 41.- Variation of C_L with x at high speed. C_p = 0.320; J = 3.80.